

SOME ASPECTS OF GAMMA-RAY ASTRONOMY

By

LAB SAHA

Enrolment No : PHYS05200704012

Saha Institute of Nuclear Physics, Kolkata

A thesis submitted to the

Board of Studies in Physical Sciences

In partial fulfilment of requirements

for the Degree of

DOCTOR OF PHILOSOPHY

of

HOMI BHABHA NATIONAL INSTITUTE



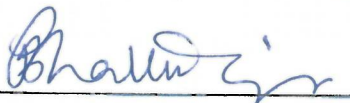
May, 2014


Homi Bhabha National Institute

Recommendations of the Viva Voce Board

As members of the Viva Voce Board, we certify that we have read the dissertation prepared by Lab Saha entitled "Some aspects of gamma-ray astronomy" and recommend that it may be accepted as fulfilling the dissertation requirement for the Degree of Doctor of Philosophy.



Chair - Prof. Pijushpani Bhattacharjee Date: 07/08/2014


Guide/Convener - Prof. Pijushpani Bhattacharjee Date: 07/08/2014


Member 1 - Prof. Debades Bandyopadhyay Date: 7.8.2014


Member 2 - Prof. Satyajit Saha Date: 7.8.2014


Member 3 - Prof. Pratik Majumdar Date: 7.8.2014

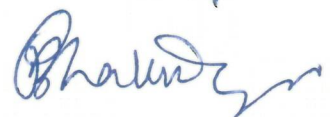

External Examiner - Prof. Prasad Subramanian Date: 7/8/2014

Final approval and acceptance of this dissertation is contingent upon the candidate's submission of the final copies of the dissertation to HBNI.

I hereby certify that I have read this dissertation prepared under my direction and recommend that it may be accepted as fulfilling the dissertation requirement.

Date: 07/08/2014

Place: KOLKATA



Guide

STATEMENT BY AUTHOR

This dissertation has been submitted in partial fulfilment of requirements for an advanced degree at Homi Bhabha National Institute (HBNI) and is deposited in the Library to be made available to borrowers under rules of the HBNI.

Brief quotations from this dissertation are allowable without special permission, provided that accurate acknowledgement of source is made. Requests for permission for extended quotation from or reproduction of this manuscript in whole or in part may be granted by the Competent Authority of HBNI when in his or her judgement the proposed use of the material is in the interests of scholarship. In all other instances, however, permission must be obtained from the author.

Lab Saha

Lab Saha

DECLARATION

I hereby declare that the investigation presented in the thesis has been carried out by me.
The work is original and has not been submitted earlier as a whole or in part for a degree
/ diploma at this or any other Institution / University.

Lab Saha
Lab Saha

List of publications arising from the thesis

Journals

1. **A study of the performance parameters of the High Altitude Gamma Ray (HA-GAR) Telescope System at Ladakh in India**

Saha, L., Chitnis, V. R., Vishwanath, P. R., Kale, S., Shukla, A., Acharya, B. S., Anupama, G. C., Bhattacharjee, P., Britto, R. J., Prabhu, T. P., Singh, B. B.

Astroparticle Physics, Volume 42, February 2013, Pages 33-40

2. **Origin of gamma rays in the shell of Cassiopeia A**

Saha, L., Ergin, T., Majumdar, P., Bozkurt, M. & Ercan, N.

Astronomy & Astrophysics, Volume 563, March 2014, A88

Conferences

1. **TeV γ -ray source MGRO J2019+37 : PWN or SNR?**

Saha, L. & Bhattacharjee, P.

In the proceedings of the International Astronomical Union, January 2013, Volume 9, 300-304, doi:10.1017/S1743921313009629

2. **Locating the TeV γ -rays from the shell regions of Cassiopeia A**

Saha, L., Ergin, T., Majumdar, P., Bozkurt, M.

In the proceedings of the International Astronomical Union, January 2013, Volume 9, 380-381, doi:10.1017/S1743921313009927

3. **Monte Carlo simulation for High Altitude Gamma Ray Telescope System at Ladakh in India**

Saha, L., Acharya, B. S., Anupama, G. C., Britto, R. J., Bhattacharjee, P., Chitnis, V. R., Kale, S., Prabhu, T. P., Shukla, A., Singh, B. B., Vishwanath, P. R.

*In the proceedings of 32nd International Cosmic Ray Conference at Beijing, China,
August 2011, Volume 9, 198-201*

Others

1. **Constraint on the pulsar wind nebula scenario of origin of the TeV gamma ray emission from MGRO J2019+37 in the Cygnus region**

Saha, L. & Bhattacharjee, P.

Submitted to an International Journal.

Lab Saha

Lab Saha

to my parents....

ACKNOWLEDGEMENTS

First of all, I thank my advisor Prof. Pijushpani Bhattacharjee for his constant help and support in developing and completing my thesis. I have learned a lot from him during the very fruitful discussions that we had over the years. He gave me a lot of independence to pursue my theoretical ideas. His objective criticism at various stages of this work was immensely helpful for which I am grateful to him. I have been fortunate to work with him.

I am also thankful to my collaborators Prof. B.S. Acharya, Prof. Palahalli Vishwanath for their contributions to the experimental work presented in this thesis. I enjoyed a lot of stimulating discussions with them and learned a lot from them.

My thanks are due to Dr. V. R. Chitnis, for her valuable guidance throughout my PhD tenure. I learnt a lot about different aspects of gamma-ray astronomy, particularly Monte Carlo simulations which is an integral part of my thesis. I have also learnt X-ray astronomy from her. I am grateful to her for her constant support and encouragement.

I thank Prof. Pratik Majumdar and Dr. Tulun Ergin for their contributions in a project which is presented in my thesis. I have benefited a lot from discussions with Prof. Pratik Majumdar, particularly about imaging Cherenkov technique.

My sincere thanks also to Prof. Parthasarathi Majumdar from whom I learned a lot on many different areas in Physics.

Thanks also to Ayan da, Sayan da, Nilanjan da, Sovan da, Rana da, Srijit da, Pritibhajan da, Soumini di, Raktim, Arindam, Somdeb, Najmul, Pratyay, Parijat, Avirup, Swapan, Tapan, Atanu, Santanu, Susmita, Susnata, Satyajit, Anirban, Mainak, Debabrata, Abhishek, Amit, Anshu, Abhishek, Chandrachur, Kamakshya, Prasanta, Apurba, Naosad, Dipankar, Aminul, Goutam, Baishali, Aritra for many fruitful conversations on several topics in Physics.

I acknowledge the non-academic staff of the Theory Division and Astroparticle Physics and Cosmology Division of SINP for helping me on several administrative work.

Finally, I am deeply grateful to my parents, elder brothers, elder sister and sister-in-law for their constant support in my life. I specially thank my brother-cum-best friend Kush for being so supportive all the time. I am indebted to my wife Amrita for her love, encouragement and moral support over the last two years. I also thank my friends Tanushree and Ayon for their support over these years.

Synopsis

Gamma-ray astronomy has already entered into a new era with the discovery of more than thousands galactic and extragalactic gamma-ray sources. Gamma rays from astrophysical objects provide one of the best windows for exploration of phenomena in the non-thermal universe. High energy astrophysical processes are known to produce relativistic particles as well as associated gamma rays over an enormous range of energies. The gamma-ray radiation is considered to span over energies from 10^6 eV to $\geq 10^{20}$ eV. They are secondary products of cosmic accelerators. Cosmic rays being charged get deflected by the interstellar magnetic fields and they lose their directional information and cannot be used to pinpoint their sources, except perhaps for cosmic rays of extreme energy $> 10^{18}$ eV. Gamma rays, on the other hand, being neutral in nature come in straight lines from the cosmic accelerators. Hence they are naturally considered the most important messenger for cosmic ray accelerators. Therefore, cosmic ray accelerators can be directly probed by gamma rays on Earth. Depending on the energies of gamma rays different detection techniques have been adopted. Gamma rays in the energy range of MeV to GeV are observed through direct detection, whereas indirect detection is used for the gamma rays with energy in the range of GeV to TeV energies, the so-called very high energy (VHE) regime. For direct detection, gamma-ray detectors are put on space-based satellites or on balloons. The high energy end of this type of detectors are limited by the collection area as well as the steeply falling spectrum of cosmic rays. Currently, the best space based gamma-ray detector, namely the Large Area Telescope on board the Fermi satellite (Fermi-LAT) is able to detect gamma rays from about 20 MeV to 300 GeV. In case of indirect detection of VHE gamma rays, ground based gamma-ray telescopes with much greater collection area than that of space based detectors are used. In this case, atmosphere plays a crucial role. When a VHE gamma-ray enters into the Earth's atmosphere, it interacts with atmospheric nuclei and produces a electron-positron pair, which in turn dissipate their energy through producing secondary gamma rays through bremsstrahlung processes. The secondary gamma rays further produces electron-positron pairs. This process of pair production and bremsstrahlung continues, resulting in a shower of electrons, positrons and

secondary gamma rays, which is called Extensive Air Shower (EAS). When the charged particles move down in the atmosphere with velocities greater than the velocity of the light in that medium, they cause the atmosphere to produce Cherenkov light, which falls in the Ultra Violet and blue (UV-blue) region of the electromagnetic spectrum. The Cherenkov light illuminates a large circular area with a diameter in the range of 200 m – 250 m on the ground for vertically incident shower. This light can be captured with optical elements, and reconstructing the shower axis in space and tracing it back onto the sky, celestial origin of the gamma rays can be determined. In addition, the energy of the gamma-ray can be estimated since the amount of Cherenkov light relates to the energy of the gamma-ray.

This thesis is broadly divided into two parts: (a) Monte Carlo simulations, observations and analyses of data for High Altitude GAMMA Ray (HAGAR) telescope system, and (b) the multi-wavelength modelling of two Galactic TeV gamma-ray sources.

Part 1:

MC simulation, observation and data analysis studies for HAGAR system

Like the ground based gamma-ray detectors such as H.E.S.S., MAGIC and VERITAS, HAGAR telescope system is designed to detect very high-energy gamma rays from celestial sources through the atmospheric Cherenkov technique. This technique of recording atmospheric Cherenkov photons was pioneered by Galbraith and Jelly in 1953 [1], using a single PMT and mirror. Unlike those existing ground-based instruments (H.E.S.S., MAGIC and VERITAS), HAGAR is based on the non-imaging atmospheric Cherenkov technique which measures arrival time of the Cherenkov shower front at various locations in the Cherenkov light pool using an array of telescopes. From the arrival time information, the direction of shower axis is estimated to enable rejection of off-axis cosmic ray showers. The HAGAR telescope system consists of an array of seven telescopes located at Hanle ($32^{\circ}46'46''$ N, $78^{\circ}58'35''$ E, 4270 m above msl), Ladakh, in the Himalayas. Each telescope consists of seven front-coated parabolic mirrors each of diameter 0.9 m. A photomultiplier tube (PMT) is kept at the focal point of each of the mirrors. The pulses from seven PMTs of a telescope are added to obtain what is called the “royal sum” pulse. The event trigger is formed if there is a coincidence of four royal sum pulses out of seven telescopes with amplitude above a predefined threshold and within a time window of 150 ns to 300 ns. HAGAR is the highest altitude atmospheric Cherenkov telescope in the world. Taking advantage of the high altitude, this experiment achieves a comparatively low energy threshold of 208 GeV with a modest mirror area of 31 m². Another setup similar to HAGAR but at lower altitudes is PACT(Pachmarhi Array of Cherenkov Telescopes) [2, 3, 4] in INDIA. It is installed at Pachmarhi, on the hills of the Satpura mountain range,

in the state of Madhya Pradesh (Central India). The altitude of PACT is 1075 m amsl. The energy threshold for this PACT array was estimated to be 700–800 GeV, about a factor of 4 higher than that achieved by HAGAR.

Since, it is not possible to produce VHE photons in the laboratory, direct calibration of the telescope system is not possible. In this situation, the performance of the system has to be understood through Monte Carlo (MC) simulations. This is a standard procedure in high energy physics, where direct calibration of the system is not possible. The simulations for HAGAR are done in two steps. In the first step of the simulation procedure, the production of EAS in the atmosphere initiated by the interaction of cosmic charged particles or gamma rays at the top of the atmosphere and the production and propagation of the Cherenkov photons produced by the charged particles in the EAS are simulated. This step is usually called “shower simulation”. Then in the second step, the “detector simulation”, the response of the detector (the telescope system with its associated electronics) is simulated. For air shower simulations, we have used the freely available software package CORSIKA [5, 6]. On the other hand, for detector simulations, the simulation software specific to the HAGAR system has been developed in house. CORSIKA is a MC program for simulating EAS in the atmosphere initiated by cosmic gamma rays and charged particles. Information about Cherenkov photons, produced by charged particles, with wavelength in the range of 200–650 nm is stored. The CORSIKA simulation provides information about the arrival times and direction of Cherenkov photons at detector plane. This information is then passed through the detector simulation program, and corresponding detector responses are studied. The output obtained from the detector simulation is analysed to estimate the performance parameters of the detector. In addition, simulation results are compared with the observed results. From our MC Simulations, we have established that the HAGAR system is able to observe Crab Nebula in 17 hours with a statistical significance of 5σ at an energy threshold of about 210 GeV [7]. The estimated trigger rate agrees well with the observed trigger rate of 13Hz. It has also been found that the simulated trigger rates at various zenith angles are consistent with the corresponding observed trigger rates.

Regular source observations have been continuing with the complete setup of 7 telescopes of the HAGAR array since September 2008. Several sources including both the galactic and extragalactic sources have been observed with HAGAR. The time of arrival of each shower front is recorded using Time to Digital Converter (TDC) in each telescope. Relative timing differences in the arrival of the Cherenkov wavefront at the telescopes are fitted using a plane front approximation to estimate the space angle (i.e. angle between the direction of incidence of a shower and the pointing direction of the telescope) for each

shower. Gamma-ray events are expected to arrive close to the telescope axis direction for point source observation whereas cosmic ray background events arrive isotropically. Data are taken pointing all the 7 telescopes towards the source direction (On-source run). This is followed (or preceded) by a background run (Off-source run) covering the same zenith range but without a gamma-ray source. By comparing the space angle distribution for On-source and Off-source observations the excess of gamma-ray events is estimated. The analysis of 14.3 hours (after data quality selection) of the Crab nebula data from the period 2010–2011 gives 5.63 ± 0.63 γ -rays/min with 8σ significance when more than or equal to 5 telescopes are participating in the trigger formation. In addition to that, a high mass X-ray binary source LSI 61+303 was observed during the period of 2010 and 2012. The result of the analysis of about 22 hours' data gives an estimate of 3.8 ± 0.5 γ -rays/min with 6σ significance when more than or equal to 5 telescopes are participating in the trigger formation. Furthermore, another galactic object MGRO J2019+37, which is supposed to be a Pulsar Wind Nebula (PWN), has been observed with HAGAR. The analysis of about 5.2 hours (after data quality selection) of the MGRO J2019+37 data taken during 2010 gives 3.67 ± 1.16 γ -rays/min with 3σ significance when more than or equal to 5 telescopes are participating in the trigger formation.

Part 2:

Multi-wavelength modelling of TeV gamma-ray sources

We have performed multi-waveband modelling of two galactic sources to understand the gamma-ray emission mechanism as well as to understand the nature of the sources. The Milagro collaboration has recently reported an extended TeV gamma-ray source MGRO J2019+37 in the Cygnus region [8, 9, 10]. No confirmed counterparts of this source are known although possible associations with several known sources have been suggested. We study the spectral energy distribution (SED) of the source using a leptonic model for the TeV emission within the context of a Pulsar Wind Nebula (PWN), using constraints from multi-wavelength data from observations made on sources around MGRO J2019+37. These include a radio upper limit given by the Giant Meter wave Radio Telescope (GMRT) [11], GeV observations by Fermi-LAT [12], EGRET [13, 14] and AGILE [15] and VHE data taken from Milagro [10]. We find that, within the PWN scenario, while leptonic model can explain the TeV flux from this source, the upper limit from the radio observation using GMRT imposes a stringent constraint on the size of the emission region.

Additionally, multi-wavelength modelling was done for another galactic source Cassiopeia A (Cas A). It is a historically well-known shell type supernova remnant (SNR) observed

in almost all wavebands, e.g. radio [16], optical [17], IR [18], and X-rays [19, 20] and TeV gamma rays [21, 22]. Upper limits on the GeV gamma-ray emission from this source were first reported by EGRET. However, the first detection at GeV energies was reported by the Fermi-LAT in 2010 [23]. The brightness of this source in all wavelengths makes it a unique galactic astrophysical source for studying the origin of galactic cosmic rays as well as high-energy phenomena in extreme conditions. Non-thermal X-ray emission from the shell of Cas A has been an interesting subject of study, as it provides information about relativistic electrons and their acceleration mechanisms in the shocks. The *Chandra* X-ray observatory revealed the detailed spectral and spatial structure of this SNR in X-rays. The spectral analysis of *Chandra* X-ray data of Cas A shows unequal flux levels for different regions of the shell, which can be attributed to different magnetic fields in those regions. We have explained the GeV–TeV gamma-ray data in the context of both leptonic and hadronic scenario [24, 25]. We use the synchrotron emission process to explain the observed non-thermal X-ray fluxes from different regions of the shell. These result in estimation of the model parameters, which are then used to explain the TeV spectrum. We also use a hadronic scenario to explain both GeV and TeV fluxes simultaneously. We show that leptonic model alone cannot explain the GeV–TeV data. Therefore, we need to invoke a hadronic model to explain the observed GeV–TeV fluxes. We found that although a pure hadronic model is able to explain the GeV–TeV data, a mixed lepto-hadronic model provides the best fit to the data.

This thesis will focus on some aspects of gamma-ray astronomy. The integral part of this thesis deals with the experimental project on gamma-ray astronomy using the High Altitude GAMMA Ray (HAGAR) telescope system which is located at an altitude of 4270 m in the Ladakh region of the Himalayas in India. Detailed Monte Carlo simulations pertaining to HAGAR system are studied to determine the performance parameters of the system. In addition, several Galactic sources are studied through analysis of data taken with the HAGAR system. The remaining part of this thesis is on phenomenological aspects of gamma-ray astronomy. In this context, two Galactic sources are studied through multi-wavelength modelling.

The thesis will be organised as follows. First chapter will give a brief introduction to gamma-ray astronomy and review of various models proposed for the mechanism of non-thermal radiation. The atmospheric Cherenkov technique along with details of HAGAR array will be described in Chapter 2. Chapter 3 deals with Monte Carlo simulations of the HAGAR system and comparison with the observed data. The observations and data analysis results of some galactic sources will be described in Chapter 4. Multi-wavelength modelling of two astrophysical sources and summary are discussed in Chapter

5 and Chapter 6, respectively.

List of Figures

1.1	Observed cosmic ray spectrum.	4
1.2	Fermi-LAT gamma-ray sky map above 1 GeV based on five years data . .	9
1.3	Characteristic spectrum of synchrotron radiation process	18
1.4	Characteristic spectra of both inverse Compton and bremsstrahlung radiation processes	19
1.5	Characteristic spectrum of π^0 -decay process	20
1.6	Multi-wavelength spectrum of the Crab nebula.	22
2.1	Polarization state of a medium when a charge particle moves through it. .	25
2.2	Illustration of the coherent nature of Cherenkov radiation.	26
2.3	Simplified schematic of extensive air shower initiated by a cosmic gamma-ray.	30
2.4	Air showers initiated by a cosmic ray proton.	32
2.5	Simulated EAS for a gamma-ray with energy 100 GeV	33
2.6	Simulated EAS for a proton with energy 100 GeV	36
2.7	Position of Cherenkov photons on the ground.	37
2.8	Lateral distribution of Cherenkov photons on the ground for both gamma- and cosmic ray showers.	37
2.9	Lateral distribution of Cherenkov timing profile	38
2.10	Snapshot of a typical image of a shower	41
2.11	Response of an array of four detectors to air shower	42
2.12	Hillas parameters to describe a shower image.	42
2.13	Distribution of Hillas parameters for gamma-ray and cosmic ray initiated showers.	43
2.14	A schematic diagram of HAGAR telescope array setup.	44
2.15	One of the telescopes of the HAGAR array.	45
2.16	A schematic diagram of the HAGAR telescope control.	46
2.17	Flowchart of telescope electronics in the HAGAR DAQ.	48
2.18	Flowchart of trigger setup and its distribution in the DAQ.	49
2.19	Shower front arriving at two telescopes	53
2.20	Space angle distribution of a typical ON-source run	54

2.21	Space angle distribution of an ON-OFF pair and excess in signal	56
3.1	Normalized NSB flux distribution in the wavelength range of 3000 Å to 6000 Å	64
3.2	Quantum efficiency plot for PMT (XP2268B).	65
3.3	Differential rate plots for different trigger conditions for simulated gamma-ray showers.	69
3.4	Differential rate plots for different zenith angles for the ≥ 4 trigger condition.	70
3.5	Energy threshold vs trigger rate from simulations.	71
3.6	Effective collection area vs energy of primary from simulations for vertical incidence for ≥ 4 trigger condition.	72
3.7	Detection efficiency vs energy for γ -rays from simulations for the ≥ 4 fold trigger condition.	73
3.8	Detection efficiency vs impact parameter for γ -rays from simulations for the ≥ 4 fold trigger condition.	74
3.9	Detection efficiency vs viewcone for proton showers from simulations for the ≥ 4 fold trigger condition.	75
3.10	Observation duration vs source flux for detection of a source at 5σ significance level with HAGAR.	75
3.11	Comparison of the data with simulations for trigger rates at different elevation angles.	76
3.12	Comparison of space angle distributions from simulations with observed data, both for vertical directions.	78
3.13	Comparison of space angle distributions from simulated cosmic ray (proton and helium) and γ -ray showers, both for vertical directions.	79
4.1	Observation period during October 2012 to September 2013.	82
4.2	<i>Left:</i> event rates of a good quality run. <i>Right:</i> event rates of a bad quality run	85
4.3	Distribution of R_{stab} of 50 runs with a vertical line which separates good and bad quality runs.	86
4.4	Location of the Crab nebula (red circle with radius 3 degrees; ON-source region) in the sky along with the two background regions (green circles with radius 3 degrees; OFF-source regions).	87
4.5	<i>Upper:</i> Distribution of gamma-ray rates for 23 pairs of the Crab nebula data for $NTT \geq 4$. <i>Lower:</i> Gamma-ray light curve of the Crab nebula for all 23 pairs for different telescope triggering conditions.	92
4.6	The integral flux of the Crab nebula.	93

4.7	Orbital geometry of LSI 61+303.	96
4.8	Location of LSI 61+303 (red circle with radius 3 degrees; ON-source region) in the sky along with the two background regions (green circles with radius 3 degrees; OFF-source regions).	97
4.9	Distribution of orbital phase vs exposure time for the observation of LSI 61+303.	101
4.10	<i>Upper:</i> Distribution of gamma-ray rates for 34 pairs of LSI 61+303 for $NTT \geq 4$. <i>Lower:</i> Light curve of LSI 61+303 for different trigger conditions.	102
4.11	Gamma ray rates of LSI +61 303 as a function of orbital phase for different telescope trigger conditions.	104
4.12	Location of the MGRO J2019+37 (3 degree radius red circle; ON-source region) in the sky along with the two background regions (green circles with radius 3 degree; OFF-source regions).	106
4.13	<i>Upper:</i> Distribution of gamma-ray rates for all 9 pairs for $NTT \geq 4$. <i>Lower:</i> Light curve for MGRO J2019+37 for all 9 pairs for different telescope triggering conditions.	108
5.1	Multi-colour image of Cas A based on Chandra observation	113
5.2	X-ray spectra for five different regions of Cas A	114
5.3	Synchrotron spectra with the observed best-fit X-ray data for different regions of the shell	116
5.4	IC spectra of the whole remnant, based on parameters related to different regions of the shell	118
5.5	Gamma-ray spectra of Cas A for different leptonic emission processes. . .	119
5.6	Gamma-ray spectra of Cas A for both leptonic and hadronic emission processes	120
5.7	Gamma-ray spectrum for lepto-hadronic model	121
5.8	Spectral energy distribution of MGRO J2019+37	135
5.9	Variation of $r_{em,max}$ with magnetic field and various electron parameters . .	141
5.10	Variation of $r_{em,max}$ and the corresponding total energy in electrons	142
6.1	An artist's impression of CTA array	147

List of Tables

3.1	Samples generated for vertical showers.	62
3.2	The NSB fluxes at different sites of gamma-ray telescopes.	63
3.3	Performance parameter for HAGAR telescope array for vertical shower. .	66
3.4	Performance parameters for various zenith angles for the ≥ 4 trigger condition.	66
3.5	Variation of trigger rate and energy threshold with discriminator bias. . . .	68
3.6	Variation of trigger rate and energy threshold with NSB flux level.	69
3.7	Dependence of the energy threshold and effective collection area on the spectral shapes of the γ -ray energy spectrum.	71
3.8	Telescope Trigger Ratio, R_N , for simulated data, $R_{N,s}$, and for observed data, $R_{N,o}$ with N, the number of telescopes.	77
4.1	Observation log from September, 2008 to September, 2013 (Run number 1 to 3690)	83
4.2	Selected pairs for the Crab nebula analysis.	89
4.3	Results of the Crab nebula for NTT equal to 4-fold, 5-fold, 6-fold and 7-fold.	91
4.4	Results of the Crab nebula for NTT \geq 4-fold, 5-fold, 6-fold and 7-fold . .	91
4.5	Selected pairs for the LSI 61+303 analysis.	99
4.6	Observation time, orbital phase, and duration for all ON-source runs for the observations of LSI 61 +303.	100
4.7	Orbital phase and corresponding exposure time for all the pairs for LSI 61+303.	101
4.8	Results of LSI + 61 303 for NTT equal to 4-fold, 5-fold, 6-fold and 7-fold.	103
4.9	Results of LSI + 61 303 for NTT \geq 4-fold, 5-fold, 6-fold and 7-fold . . .	103
4.10	Selected pairs for the MGRO J2019+37 analysis.	107
4.11	Results of MGRO J2019+37 for NTT equal to 4-fold, 5-fold, 6-fold and 7-fold.	107
4.12	Results of MGRO J2019+37 for NTT \geq 4-fold, 5-fold, 6-fold and 7-fold. .	107

5.1	The magnetic field parameters for the synchrotron spectra for all selected regions.	115
5.2	Parameters used for calculating the bremsstrahlung spectrum contributing to the emission from the S-region of the SNR.	117
5.3	Parameters for gamma-ray production through decay of neutral pions. . .	121
5.4	Parameters of the model for MGRO J2019+37	134

Contents

Synopsis	i
List of Figures	vii
List of Tables	xi
1 Gamma-Ray Astronomy	1
1.1 Introduction	1
1.2 Motivation	2
1.3 History and development of VHE gamma-ray astronomy	6
1.4 Sources of gamma rays	8
1.4.1 Galactic sources	8
1.4.2 Extragalactic sources	11
1.5 Radiation processes	12
1.5.1 Photons produced by high energy electrons	12
1.5.2 Photons produced by high energy protons	16
1.6 Multi-wavelength modelling of gamma-ray sources	21
2 Atmospheric Cherenkov Technique	23
2.1 Cherenkov radiation	24
2.2 Extensive air shower (EAS)	29
2.2.1 Gamma-ray initiated air shower	29
2.2.2 Cosmic ray initiated air shower	31
2.2.3 Differences between gamma-ray and hadron induced showers . . .	33
2.3 Detection Technique	39
2.3.1 Wavefront Sampling Technique	39
2.3.2 Imaging Technique	40
2.4 HAGAR Array	44
2.4.1 Telescope Control System	44
2.4.2 Data acquisition system (DAQ)	45
2.5 Observations	49

2.5.1	Fixed-angle run	49
2.5.2	ON-source run	50
2.5.3	OFF-source run	50
2.6	Data Analysis	50
2.6.1	TZERO (t0) estimation	51
2.6.2	Space Angle estimation	52
2.6.3	Signal extraction	54
2.7	Summary	58
3	Monte Carlo Simulations for HAGAR	59
3.1	Atmospheric air shower simulations	59
3.1.1	CORSIKA output	62
3.2	Detector simulation	62
3.3	Performance parameters	65
3.3.1	Trigger rate	65
3.3.2	Energy threshold	67
3.3.3	Effective area	70
3.3.4	Detection efficiency	71
3.3.5	Sensitivity	73
3.4	Comparison of observational data with Monte Carlo simulations	76
3.5	Summary	80
4	TeV Gamma-ray sources	81
4.1	Data selection	84
4.2	Crab Nebula	86
4.2.1	Analysis and results	88
4.3	LSI 61+303	94
4.3.1	Analysis and results	95
4.4	MGRO J2019+37	105
4.4.1	Analysis and results	105
4.5	Summary	109
5	Multi-wavelength modelling of TeV gamma-ray sources	111
5.1	Modelling of Cassiopeia A	111
5.1.1	Modelling the spectrum	113
5.1.2	Discussion	121
5.1.3	Summary & conclusion	124
5.2	Modelling of MGRO J2019+37	125

5.2.1	Injection spectra of electrons	128
5.2.2	Multiwavelength photon spectra and constraints	129
5.2.3	Summary and conclusions	139
6	Summary and future prospects	143
6.1	Summary	143
6.2	Future directions	146
	Bibliography	149

Chapter 1

Gamma-Ray Astronomy

1.1 Introduction

Very high energy (VHE) gamma-ray astronomy is a rapidly growing field of science, and our understanding of the non-thermal universe is developing through detection of several galactic and extragalactic gamma-ray sources. Depending on the energies of gamma rays different detection techniques have been adopted. Gamma rays in the energy range of about 30 MeV to 300 GeV are observed through direct detection, whereas indirect detection is used for the gamma rays with energy in the range of above 30 GeV to few tens of TeV energies, the so-called very high energy (VHE) regime. For direct detection, gamma-ray detectors are put on space based satellites or on balloons. The capabilities of space based detectors at very high energies are limited by the collection area as well as the steeply falling spectrum of gamma rays with energy. Currently, the best space based gamma-ray detector, namely the Large Area Telescope on board the Fermi satellite (Fermi-LAT) is able to detect gamma rays from about 20 MeV to more than 300 GeV. On the other hand, ground based gamma-ray telescopes have much greater collection area than that of space based detectors. In the case of detection of gamma rays at the ground level, atmosphere plays a crucial role. When a VHE gamma-ray enters into

the Earth's atmosphere, it interacts with atmospheric nuclei and produces an electron–positron pair, which in turn dissipate their energy by producing secondary gamma rays through bremsstrahlung processes. The secondary gamma rays further produce electron–positron pairs. This process of pair production and bremsstrahlung continues, resulting in a shower of electrons, positrons and secondary gamma rays, which is called Extensive Air Shower (EAS). When the charged particles move down in the atmosphere with velocities greater than the velocity of the light in that medium, they cause the atmosphere to produce Cherenkov light, which falls in the Ultra Violet and blue (UV-blue) region of the electromagnetic spectrum. The Cherenkov light illuminates a large circular area with a diameter in the range of 200 m – 250 m on the ground for vertically incident shower. This light can be captured with optical elements, and the celestial origin of the gamma rays can be determined by reconstructing the shower axis in space and tracing it back onto the sky. Moreover, energies of the gamma rays can be measured. Detection of gamma rays by space bound and earth based detectors together provide significant understanding of our non-thermal universe in the energy range of MeV to TeV.

This Chapter is organized as follows: motivations for studying very high-energy galactic and extragalactic astrophysical sources of gamma rays are explained in section 1.2. An overview of the early history and development of VHE gamma-ray astronomy is given in section 1.3. Section 1.4 provides a short description of the galactic and extragalactic gamma-ray sources. Production mechanisms of gamma rays and modelling of their sources are discussed in section 1.5 and section 1.6, respectively.

1.2 Motivation

- One of the major motivations for studying gamma-ray astronomy is to understand the origin of cosmic rays (CRs). The CRs span a large range of energies, from 10^6 eV to more than 10^{20} eV. Cosmic rays arriving at Earth consist of protons, electrons

and other nuclei. The observed CR spectrum can be described by a pure power law (spectral index ~ -2.6) spectrum up to an energy of about 10^{15} eV, where the spectrum slightly steepens (spectral index ~ -3.0). The feature is called the “knee” as shown in Figure 1.1. The second feature in the spectrum is at about 10^{18} eV where a flattening of the spectrum back to spectral index ~ -2.6 is observed, and this is called the “ankle” of the cosmic ray spectrum. Despite extensive efforts on both theoretical and experimental aspects of cosmic ray physics for about hundred years, a coherent theory for origin and different features of CRs is still lacking. Although it is believed that cosmic particles below energy 10^{15} eV are of galactic origin, it is not clear whether galactic CRs extend up to 10^{18} eV. Moreover, there is a great deal of speculation about whether the observed CR spectrum is due to sources distributed over the entire Galaxy or it has a local origin.

CRs being charged particles, information about the source direction is lost due to their deflection in the galactic magnetic fields. Therefore, it is important to search for neutral radiation from astrophysical sources which could be the possible sites of acceleration of CRs. Hence, gamma-ray astronomy can provide detailed understanding of cosmic ray origin, their acceleration, and propagation.

Supernova remnants (SNRs) are believed to be one of the main sources of galactic cosmic rays. Evidence for acceleration of electrons at energies well above 10^{12} eV in SNRs comes from X-ray observations of several supernovae remnants [26, 27]. On the other hand, the signature of acceleration of cosmic protons in SNRs can be established from the study of the gamma-ray spectra resulting from decay of neutral pions (π^0 s) which are secondary products of interactions of cosmic ray protons with the gas or molecular clouds in the surrounding region. Although cosmic ray electrons can contribute to gamma rays through inverse Compton and bremsstrahlung processes, the shape of the gamma-ray spectra from protons is different from that from electrons. Therefore, the observation of the gamma-ray spectrum from a source can provide important information about the population of high energy par-

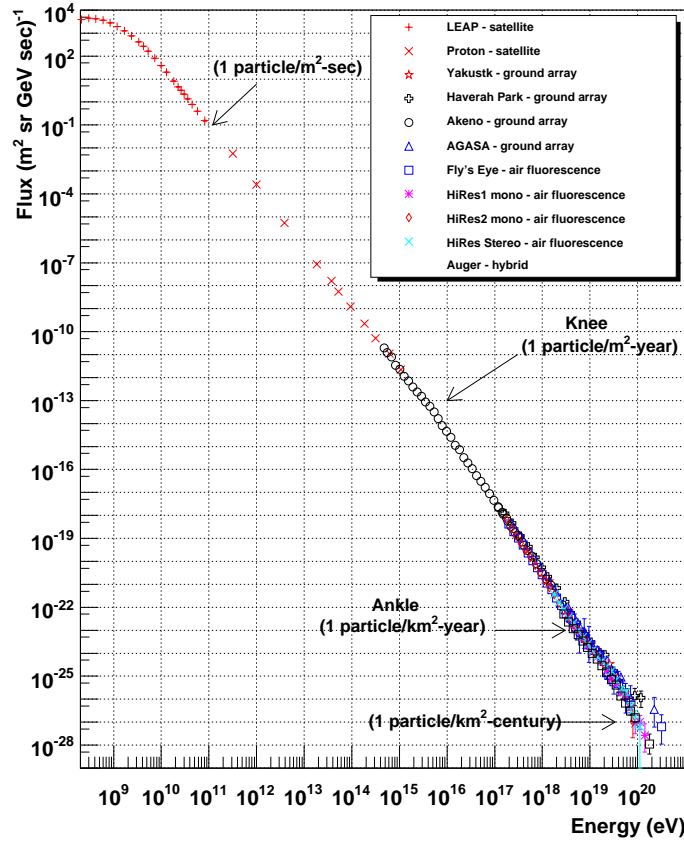


Figure 1.1: Observed cosmic ray spectrum.

ticles inside the source. Recently, direct spectral signatures of gamma-ray emission from decay of π^0 have been found in two middle-aged SNRs interacting with molecular clouds: W44 and IC 443 [28].

- Another motivation for the study of gamma-ray astronomy is to understand the intergalactic radiation field. This radiation field provides a measure of the radiative energy released in the process of star formation that has occurred since the decoupling of matter and radiation following the Big Bang. Very high energy gamma rays from extragalactic objects may interact with cosmic microwave background radiation (CMBR) and/or infrared (IR) photons on their way to earth and produce electron-positron ($\gamma\gamma \rightarrow e^+e^-$) pair. Therefore, the observed spectrum of gamma rays from a distant object would be different from the emission spectrum at the

source. Gamma rays at TeV energies are attenuated depending on the gamma-ray energy, the distance to the source, and the density of intergalactic background photons. If the intrinsic source spectra can be inferred from observations of several similar sources, the background radiation density can be estimated from spectral measurements made on sources at different redshifts [29, 30, 31].

- Gamma-ray bursts (GRBs) are the most luminous explosions in the Universe emitting as much as $10^{52} - 10^{54}$ ergs of energy during a brief period of 0.01–1000 s. They are considered to be potential candidates for the sources of ultra-high-energy cosmic rays (UHECRs) with energies up to 10^{20} eV. They occur at cosmological distances and show rapid and irregular variability on timescales down to sub-millisecond levels. The UHECRs in GRBs may also induce observable fluxes of high-energy neutrinos [32, 33]. Measurements of gamma rays from GRBs will provide crucial diagnostic tools of ultra-high-energy cosmic ray and neutrino production in GRBs, advance observational cosmology by probing the high-redshift extragalactic background light and intergalactic magnetic fields, and contribute to fundamental physics by testing Lorentz invariance violation with high precision or to probe the structure of space-time [34, 35].
- Another motivation for gamma-ray astronomy is to look for signatures of Dark Matter. Weakly Interacting Massive Particles (WIMPs) with masses in the energy range of few GeV to few TeV are considered as natural candidates for the dark matter in the Universe. Annihilation of WIMPs in high density regions such as the Galactic Centre can produce high-energy gamma rays with energies extending up to the mass of the WIMP. Therefore, a signature of dark matter can be obtained by detection of gamma rays resulting from WIMP annihilation.

1.3 History and development of VHE gamma-ray astronomy

In 1948, P .M. S. Blackett had noticed the presence of a small fraction of Cherenkov photons in the night sky background light [36]. He proposed that the Cherenkov photons were originating from primary cosmic rays and their secondaries in the atmosphere. Following this, Bill Galbraith and John Jelley [1] took initiative to detect short pulses of Cherenkov radiation. The experimental set up used by Jelly and Galbraith consists of a parabolic mirror of 25cm diameter, a photomultiplier tube (PMT), and a cylindrical can along with some simple electronic components [1]. They found about one event in every two minutes whose pulse height was exceeding the level of the noise in the night-sky background. The detection of atmospheric Cherenkov photons from air shower initiated by cosmic rays in the 1953s opened the way for gamma rays studies from astrophysical sources by ground-based telescopes.

It can be said that the subject of gamma-ray astronomy started with the publication of a historic paper by Phillip Morrison [37] in 1957. He suggested the Crab nebula as a possible source of cosmic rays. Soon after, in 1959, Cocconi proposed Crab nebula as a possible source of TeV gamma rays [38], which motivated Chudakov and others at the Lebedev Research Institute, Russia, to build a Cherenkov telescope for detecting gamma-ray sources [39]. The telescope built by Lebedev group consisted of 12 mirrors of aperture 1.5 m, and it was operational from 1960 to 1963. But, no significant detection could be made of gamma rays from any of the sources including the Crab nebula, Cygnus A, and Cassiopeia A.

In the 1970s, the space based gamma-ray detectors, COS-B and SAS-2, gave an enormous boost to the field with the first direct detection of gamma rays from outer space. These experiments, operating at energies between 35 MeV and 5 GeV, detected a diffuse gamma-ray flux concentrated in the Galactic plane. In addition, an isotropic extra-galactic

gamma-ray background was also found by them [40]. The first significant detection from the Crab nebula was reported in 1989 by the 10 m Whipple telescope which started operating in 1968 at Mount Hopkins, in south Arizona, USA. They reported a detection with 9.0σ significance above 0.7 TeV [41], based on the data taken during 1986–1988. They also observed additional twenty-six possible gamma-ray sources in the energy range of 10^{11} eV to 10^{12} eV, without any significant detection.

NASA's space based Compton Gamma Ray Observatory (CGRO), which was launched on 5th April, 1991, added another dimension to this field by detecting more than 250 sources in the energy range from about 30 MeV to over 20 GeV [42]. In the late 90s, with the knowledge gained with Whipple telescope, several new ground-based telescope systems were proposed to be built. Among those telescopes MAGIC, HESS and VERITAS telescopes are currently in operation and providing exciting results in this field. A brief introduction of all these telescopes can be found, for example, in Ref. [43].

Further development in this field at MeV to GeV energies was made by the The Fermi Gamma Ray Space Telescope spacecraft which was launched into a near-earth orbit in 2008. The on-board Large Area Telescope (LAT) is an imaging high-energy gamma-ray telescope covering the energy range from about 20 MeV to more than 300 GeV. The LAT's field of view covers about 20% of the sky at any time, and it scans the sky continuously, covering the whole sky every three hours. It has detected about 1500 gamma-ray sources from the whole sky so far.

Indian contribution in the field of VHE gamma-ray astronomy came through the observations of few gamma-ray sources in 1969 in Nilgiri Hills in South India [44]. This was then followed by the operations of an array of Cherenkov telescope near Ooty in southern India, PACT (Pachmarhi Array of Cherenkov Telescopes), TACTIC (TeV Atmospheric Cherenkov Telescope with Imaging Camera) and HAGAR (High Altitude GAMMA Ray) telescope systems. Details about the PACT and TACTIC experiments can be found from Refs. [45, 2, 46]. I shall describe the HAGAR telescope system in more details later in

this thesis.

1.4 Sources of gamma rays

1.4.1 Galactic sources

There are many gamma-ray sources observed within the MilkyWay. The gamma-ray sky map is shown in Figure 1.2. The central bright region consists of several Galactic gamma-ray sources including a diffuse gamma-ray background. The most prominent Galactic gamma-ray sources are supernova remnants (SNRs). In addition, pulsar wind nebulae (PWNe) and high-mass X-ray binaries are two different class of galactic objects which could emit gamma rays. Moreover, the diffuse high-energy gamma-ray emission above about 30 MeV is dominantly seen along the Galactic plane. A brief introduction to these sources are given below.

Supernova remnants

Supernova remnants are considered to be most probable sources of galactic cosmic rays and are known to radiate in radio, X-rays, GeV and sometimes TeV gamma rays. The diffuse shock acceleration mechanism of acceleration of charged particles in supernova shocks offers a plausible explanation for the origin of cosmic rays up to energies of $\sim 10^{14}$ eV [47, 48]. A supernova explosion typically releases $\sim 10^{51}$ ergs of kinetic energy, and it can power the cosmic rays if $\sim 10\%$ of the kinetic energy released during the explosion goes into acceleration of protons and nuclei. The strong shock front produced by the material ejected at supersonic speeds from the explosion can accelerate the charged particles from the surrounding medium. Charged particles diffuse back and forth across the shock front by scattering on the irregularities in the magnetic field, and this leads to a net gain of energy after passage through the shock front after many such scatterings. The

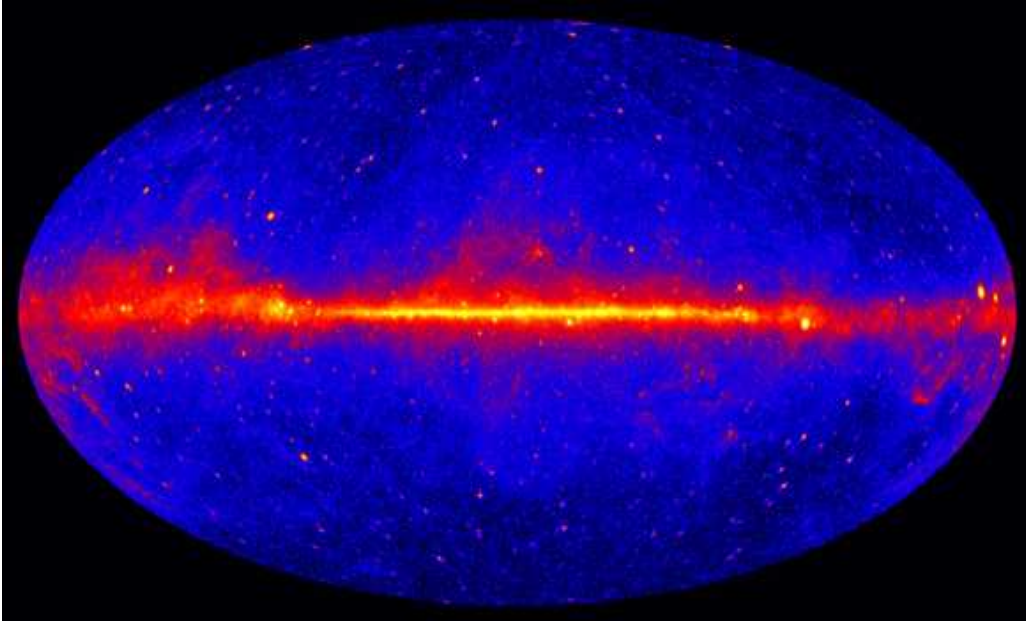


Figure 1.2: The gamma-ray map of the entire sky at energies greater than 1 GeV based on five years of data from the LAT instrument on NASA's Fermi Gamma-ray Space Telescope. Brighter colors indicate brighter gamma-ray sources <http://fermi.gsfc.nasa.gov/>.

acceleration process was first proposed by Fermi [49] and this has been extensively reviewed by many others [50, 51, 52]. The acceleration at the shocks produces a spectrum of cosmic rays close to the observed spectrum. For young shell-type supernovae remnants where the remnant material exists in the form of several shells, the outer shells are the most plausible acceleration sites of high-energy electrons with the diffusive shock acceleration mechanism [53]. Although acceleration of electrons to TeV energies is established through detection of X-rays from some shell-type supernova remnants [26, 27], more direct proof of acceleration of protons is still lacking. Nonthermal X-rays and gamma rays can be produced in shell-type supernova remnants by extremely energetic electrons via electron synchrotron, bremsstrahlung, or inverse-Compton process. Evidence of acceleration of protons can be obtained by unambiguous detection of gamma rays resulting from decay of neutral pions produced by interaction of protons with the interstellar medium.

Pulsar wind nebulae

Pulsars are rapidly rotating astrophysical objects. Gamma rays have been detected from many pulsar wind nebulae (PWNe). In a PWN, a pulsar is surrounded by a supernova remnant and the nebula is powered by the pulsar. Pulsars lose their rotational energy through streaming winds of electrons, positrons and ions. The stopping of the winds from the pulsar by the nebular material gives rise to a so-called "collisionless shock" or wind shock front where no collisional energy loss occurs when particles interact with the shock front. The position of the shock front is determined by the balance between the wind pressure and the total pressure in the nebula caused by accumulation of the energy injected in the nebula over the time of the pulsar age [54]. Crab nebula is powered by the pulsar sitting at the center of the nebula, and it is considered as the best example of a PWN. Reviews of the various theories of PWN including latest observation results can be found, for example, in Ref. [55, 56, 57]. According to typical PWN models, electrons and positrons in the winds from the pulsar get accelerated to energies with Lorentz factor of $\sim 10^4$ through magnetohydrodynamics processes before they are stopped by the wind shock. Then those particles get randomized in the downstream region of the shock, and they are then further accelerated to even higher energies through Fermi shock acceleration mechanism [49] and streamed into the surrounding nebula. In the nebula they interact with magnetic fields and photon fields and ambient matter to produce photons through synchrotron, inverse Compton and bremsstrahlung processes.

High-mass X-ray binaries

High mass X-ray binaries, another distinct class of Galactic objects, are established as potential gamma-ray emitters. There are two types of these binaries: binary pulsars and microquasars. Binary pulsars are thought to be a system consisting of a compact object orbiting around a B0 main-sequence star with a circumstellar disc (i.e., a Be star). In this system, high energy emission results from the interactions of the pulsar wind with the

dense circumstellar disc of the Be star. On the other hand, microquasars are binary systems consisting of a compact object of a few solar masses (a neutron star or a black hole) and a companion star that loses mass into an accretion disk around the central compact object giving rise to well collimated relativistic jet-outflows of matter from regions close to the central accreting black hole or neutron star. TeV emission from a microquasar is possibly generated by the up-scattering of stellar UV photons by high energy electrons that are present in the jet. Microquasars could provide a measurable contribution to the cosmic ray (CR) spectrum [58]. One of the Galactic binary systems is LSI+61 303 which not only emits gamma rays but also shows variability in its emission. The variability is attributed to orbital modulation of the emission or absorption processes [59].

1.4.2 Extragalactic sources

Active galactic nuclei

Active Galactic Nuclei (AGNs) are the most prominent extragalactic sources of TeV gamma rays. AGNs are characterised by extremely luminous electromagnetic radiation produced in very compact volumes. Active galaxies are thought to host supermassive black holes at their centres, which accrete material from the surroundings, thereby releasing large amount of gravitational energy. This energy eventually comes out through thermal emission from the accretion disk, as well as through non-thermal processes in the form of jets of relativistic particles that emanate perpendicular to the plane of the accretion disc. Particle acceleration takes place throughout the entire jet extending to distances well beyond the host galaxy. These particles interact with the ambient photon and magnetic fields, thereby giving rise to non-thermal (synchrotron and inverse Compton) emission. The spectra of AGN extend over a broad range of wavelengths from radio to gamma-rays. The energy emitted by the AGN exceeds the total emission from the population of stars in the host galaxy. Although there are several classes of galaxies with

substantially different characteristics, the current classification schemes are dominated by random pointing directions rather than by intrinsic physical properties of the AGNs [60]. A particularly interesting class of AGNs are the so-called blazars which are characterised by their relativistic jets pointing towards the Earth, thereby appearing as very efficient TeV gamma-ray emitters.

1.5 Radiation processes

High-energy leptons (e^+ and e^-) can produce very high-energy (\sim GeV and above) gamma rays by inverse Compton and bremsstrahlung processes, whereas hadrons produce gamma rays through decay of pions produced in interaction of the hadron with ambient matter. The photons produced in the range of radio to X-ray wavelengths by synchrotron process play important role for inverse Compton process. A brief summary of all these radiation processes is given below for the purpose of their use in the discussions in the later Chapters of this thesis.

1.5.1 Photons produced by high energy electrons

Synchrotron radiation process

The energy spectrum of synchrotron photons produced by an electron of energy $\gamma m_e c^2$ with a pitch angle θ in a magnetic field B can be written as [61]

$$\mathcal{L}_\nu^{\text{Sy}} \equiv \left(\frac{d\mathcal{E}}{d\nu dt} \right)_{\text{Sy}} = \frac{\sqrt{3}e^3 B \sin \theta}{m_e c^2} \frac{\nu}{\nu_c} \int_{\nu/\nu_c}^{\infty} K_{5/3}(x) dx, \quad (1.1)$$

where e is the electron charge,

$$\nu_c = \frac{3e\gamma^2}{4\pi m_e c} B \sin \theta, \quad (1.2)$$

is the characteristic frequency of the emitted synchrotron radiation, and $K_{5/3}(x)$ is the modified Bessel function of fractional order 5/3. Averaging over the electron pitch angle, a value of $\langle \sin \theta \rangle = \sqrt{2/3}$ is adopted.

Thus, the energy spectrum of radiation produced by electrons with an energy spectrum $\frac{dN_e}{d\gamma}$, due to synchrotron process is given by

$$(\mathcal{L}_\nu)_{Sy}^{total} = \int_1^\infty d\gamma \frac{dN_e}{d\gamma_e} \mathcal{L}_\nu^{Sy}. \quad (1.3)$$

The characteristic spectra of synchrotron radiation are shown in Figure 1.3 for power-law ($dN_e/d\gamma \propto \gamma^{-2.1}$; for $1 \leq \gamma \leq \gamma_{max}$) distributed electrons for three different values of magnetic field and maximum energy of the electrons ($\gamma_{max} m_e c^2$).

Inverse Compton process

High-energy electrons scattering off a background of low-energy photons transfer their energy to the low energy photons thereby producing high energy photons. The energy spectrum of photons produced by this Inverse Compton (IC) scattering of an electron of energy $\gamma m_e c^2$ off a background of soft photons is given by [61]

$$\mathcal{L}_\nu^{IC} \equiv \left(\frac{d\mathcal{E}}{d\nu dt} \right)_{IC} = \frac{3}{4} \frac{\sigma_T c}{\gamma^2} h^2 \nu \int_{h\nu/(4\gamma^2)}^{h\nu} d\epsilon \frac{n_b(\epsilon)}{\epsilon} f_{IC}(\epsilon, \nu, \gamma), \quad (1.4)$$

where σ_T is the Thomson scattering cross section, $h\nu$ is photon energy after scattering, $d\epsilon n_b(\epsilon)$ is the number density of the background soft photons between energy ϵ and $\epsilon + d\epsilon$, and

$$f_{IC}(\epsilon, \nu, \gamma) = 2q \ln q + (1 + 2q)(1 - q) + \frac{1}{2} \frac{[4\epsilon\gamma q / (m_e c^2)]^2}{1 + 4\epsilon\gamma q / (m_e c^2)} (1 - q),$$

with

$$q = \frac{h\nu}{4\epsilon\gamma^2 [1 - h\nu/(\gamma m_e c^2)]}.$$

The energy spectrum of inverse Compton radiation produced by electrons with an energy spectrum $\frac{dN_e}{d\gamma}$ is given by

$$(\mathcal{L}_\nu)_{IC}^{total} = \int_1^\infty d\gamma \frac{dN_e}{d\gamma_e} \mathcal{L}_\nu^{IC}. \quad (1.5)$$

The background low energy photons can be a sum of contributions from several different components, e.g., synchrotron radiation from the same population of electrons responsible for the IC emission, emission from thermal dust, the cosmic microwave background radiation (CMB), and so forth. Although the photon density of the CMB is constant throughout the emission volume in the source, the other components may vary within the source and they are, in fact, different in different sources.

The IC interactions of the high energy electrons on the synchrotron radiation from the same population of the electrons – the so-called synchrotron self Compton (SSC) mechanism – plays an important role in gamma-ray emission from a wide variety of sources.

For the same population of electrons as considered for synchrotron radiation process, the IC spectra for different values of γ_{max} are estimated (but with the same total energy of electrons) and are shown in the upper panel of Figure 1.4.

Bremsstrahlung process

The bremsstrahlung process can be considered as Compton scattering of incoming electrons with the virtual photons of the Coulomb field of a scattering centre. When an electron passes through a plasma of various species (atoms, ions, and electrons) with corresponding number densities n_s , the bremsstrahlung spectrum per electron can be written as

[61]

$$\frac{dN_\gamma}{dt dk} = c \sum_s n_s \frac{d\sigma}{dk}, \quad (1.6)$$

where dN_γ is the number of photons with momentum within dk emitted by an electron in time dt . The differential bremsstrahlung scattering cross section for an electron from an unshielded charge Ze is given by

$$d\sigma = 4Z^2 \alpha r_0^2 (dk/k) (E_i^2)^{-1} \left[(E_i^2 + E_f^2) - \frac{2}{3} E_i E_f \right] \left[\ln(2E_i E_f / k) - \frac{1}{2} \right]; \quad (1.7)$$

where E_i and E_f are the initial and final energies of the electrons, respectively, k ($= E_i - E_f$) is the energy of the radiated photon, α is the fine structure constant, and r_0 is the classical radius of the electron.

Therefore, the total spectrum of bremsstrahlung radiation resulting from a distribution of high energy electrons, (dN_e/dE) , can be written as

$$\frac{dN_{\gamma, total}}{dt dk} = \int dE \frac{dN_e}{dE} \frac{dN_\gamma}{dt dk}. \quad (1.8)$$

Since the relativistic electrons follow power-law distribution, the resulting bremsstrahlung spectrum is non-thermal in nature as opposed to the thermal bremsstrahlung where electrons follow Maxwell-Boltzmann distribution at thermal equilibrium and which mostly produces photons at X-ray energies. The characteristic spectra of bremsstrahlung process for three different values of γ_{max} are shown in the lower panel of Figure 1.4.

1.5.2 Photons produced by high energy protons

π^0 -decay process

Inelastic p - p interactions of high energy protons and other nuclei with the ambient matter produce π^0 and η mesons whose subsequent decay gives rise to high energy gamma rays. This process has been studied by a large number of authors; see, e.g., [62] for discussions and references. Here we shall follow the treatment of Ref. [63] which gives a convenient parametrized form of the resulting γ -ray spectrum based on the results of Monte Carlo simulations of the secondary particle production in inelastic $p - p$ interactions. For a spectrum of protons, $\frac{dN_p}{dE_p}$, the spectrum of γ rays produced per unit time, $\frac{dN_\gamma}{dE_\gamma dt}$, can be written as [63]

$$\frac{dN_\gamma}{dE_\gamma dt} = cn_H \int_{E_\gamma}^{\infty} \sigma_{\text{inel}}(E_p) \frac{dN_p}{dE_p} F_\gamma \left(\frac{E_\gamma}{E_p}, E_p \right) \frac{dE_p}{E_p}, \quad (1.9)$$

where c is the speed of light, n_H is the number density of ambient matter (assumed mostly hydrogen), $\sigma_{\text{inel}}(E_p)$ is the inelastic p - p cross section, and the function $F_\gamma(x, E_p)$ (with $x = \frac{E_\gamma}{E_p}$) represents the number of photons produced per unit interval of x per interaction of a proton of energy E_p with the ambient protons. For γ -ray energies $E_\gamma \gtrsim 1$ GeV, the parametrized form of $F_\gamma(x, E_p)$ given by Eqs. (58) through (61) of Ref. [63] with the form of $\sigma_{\text{inel}}(E_p)$ given by their equation (73) can be used. For lower energies, “ δ -function approximation” for the pion production spectrum in $p - p$ collisions described in [63] with the appropriate form of $\sigma_{\text{inel}}(E_p)$ given by equation (79) of Ref. [63] can be considered.

The gamma-ray spectra resulting from the decay of π^0 s are shown in Figure 1.5, which are estimated considering power-law ($\frac{dN_p}{dE_p} \propto E_p^{-2.1}$; for $E_p \leq E_{\text{max}}$) distributed protons for three different values of maximum energies of high energy protons $E_{\text{max}} = 10, 100, 1000$ TeV, respectively, but with the same total energy of protons.

Proton synchrotron

High energy gamma rays can also be produced by synchrotron radiation of a relativistic proton. The synchrotron radiation of relativistic electrons as mentioned briefly in section 1.5.1 can be readily applied to the proton-synchrotron radiation. The characteristic frequency of the emitted synchrotron radiation by a proton of energy $\gamma m_p c^2$ in a magnetic field B is

$$\nu_c = \frac{3e\gamma^2}{4\pi m_p c} B \sin \theta, \quad (1.10)$$

where m_p is the mass of the proton and θ is the pitch angle. This frequency is $(m_p/m_e)^3 \simeq 6 \times 10^9$ times smaller than the characteristic frequency of synchrotron photons emitted by an electron of the same energy.

The spectrum of synchrotron photons produced by a proton can be obtained by replacing m_e by m_p in equation 1.1.

In some astrophysical scenarios such as in the case of blazars, TeV gamma rays from these sources could be explained by synchrotron radiation of extremely high energy protons [64].

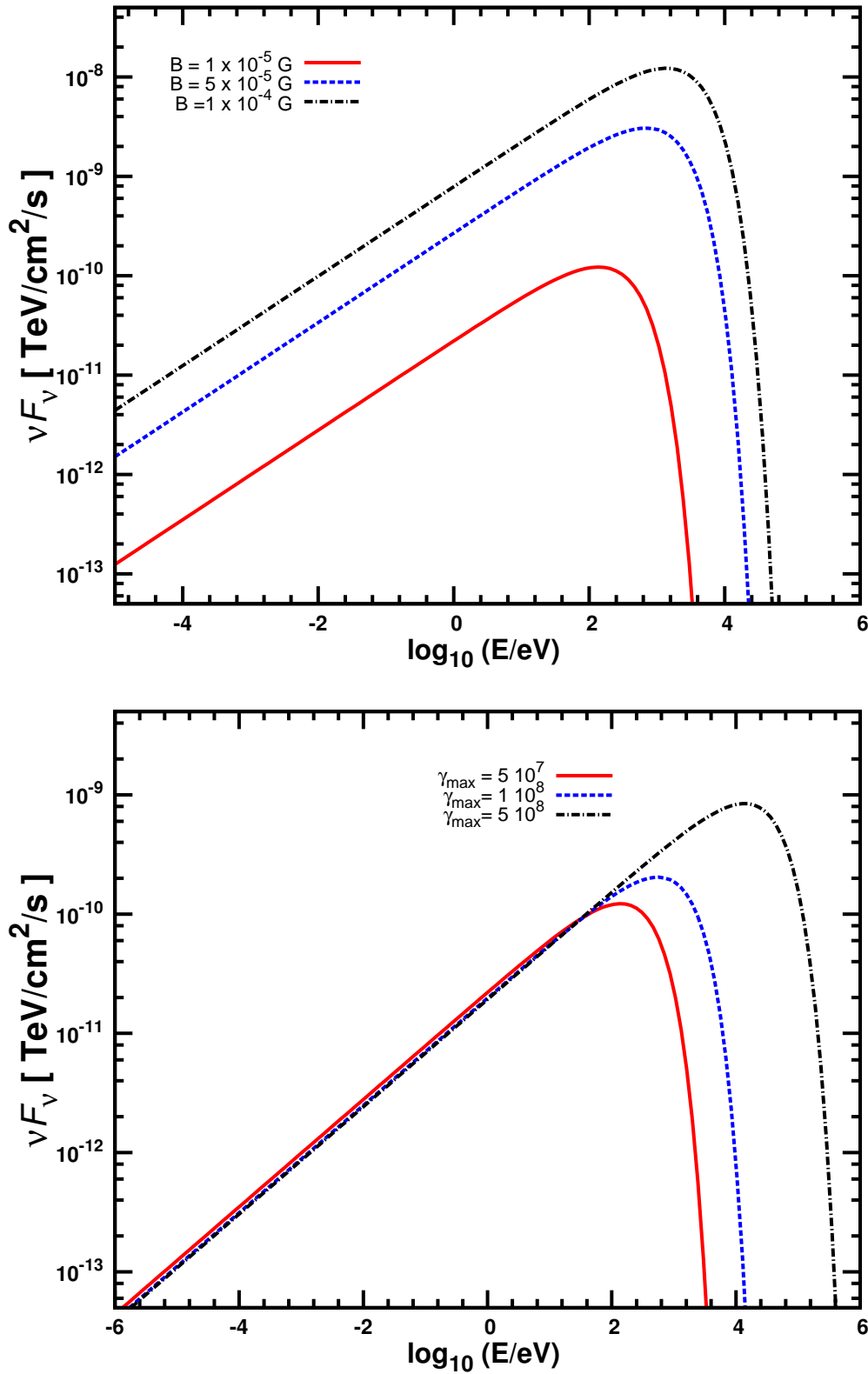


Figure 1.3: Upper panel: The synchrotron spectra from power-law distributed electrons for three different magnetic fields. Lower panel: The synchrotron spectra from the same power-law distributed electrons, but the maximum energies of electrons are different.

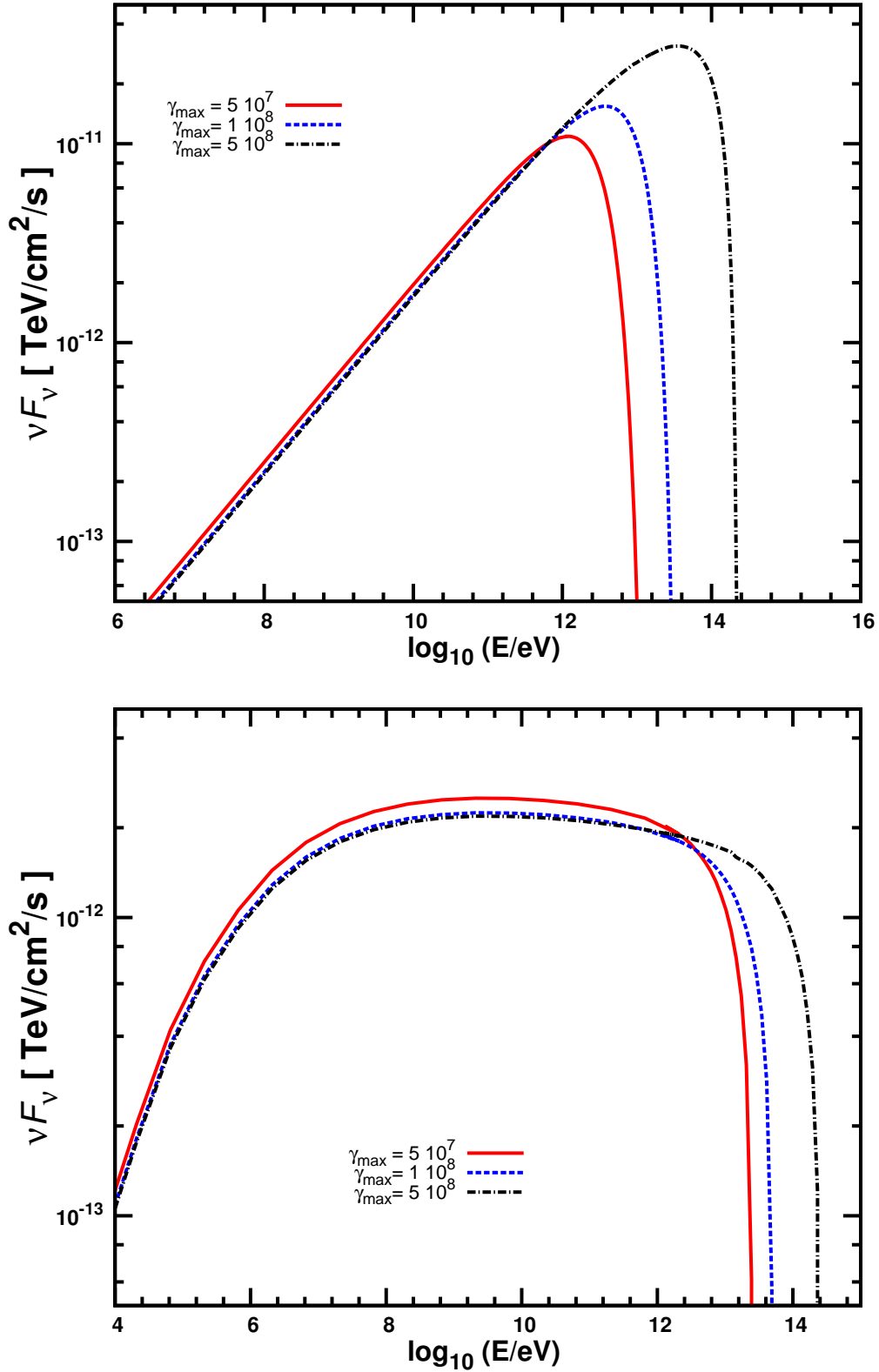


Figure 1.4: Upper panel: The IC spectra from power-law distributed electrons ($\gamma^{-2.1}$) for three values of maximum energies of the electrons. Lower panel: The bremsstrahlung spectra from the same power-law distributed electrons and three different values of maximum energies of the electrons.

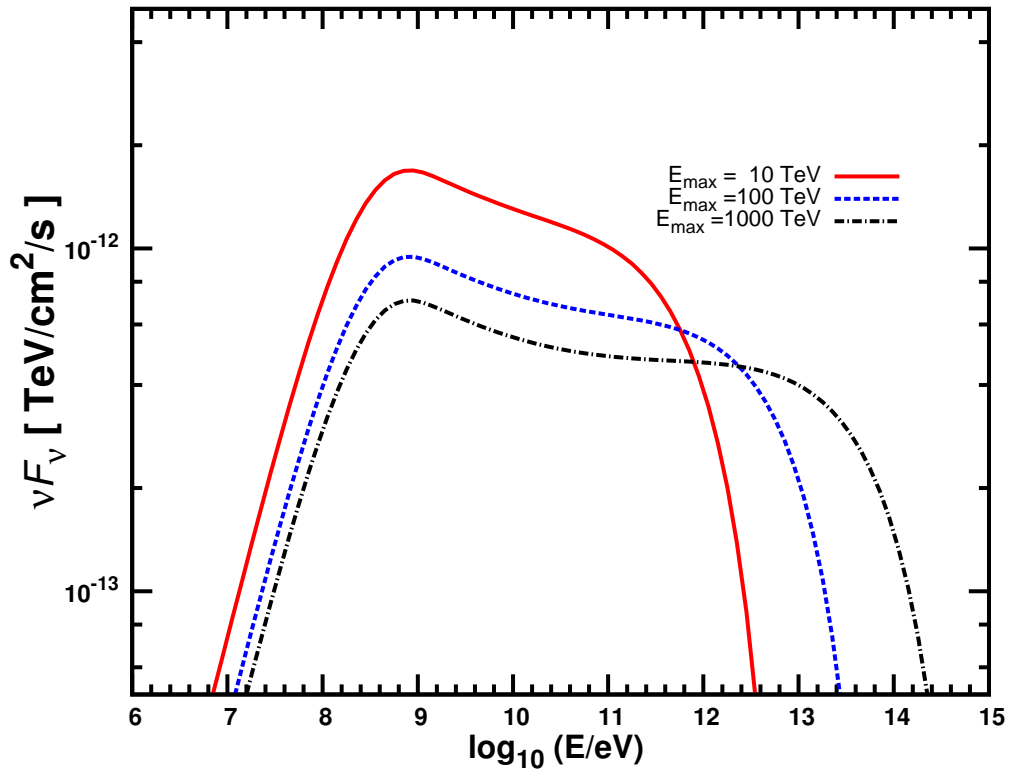


Figure 1.5: The high energy gamma-ray spectrum resulting from the decay of neutral pions produced in the interactions of high energy protons (power-law distributed) with ambient matter. The solid (red), dashed (blue) and dot-dashed (black) lines correspond to three different spectra when the maximum energies for the protons are fixed to 10, 100 and 1000 TeV, respectively and total energy of the protons are kept same for all the cases.

1.6 Multi-wavelength modelling of gamma-ray sources

Multi-waveband modelling of the gamma-ray sources is an important tool for understanding the gamma-ray emission mechanisms as well as the nature of the source. For Galactic SNRs, PWNe this approach is widely used. The observed spectra from radio to X-ray wavelengths are usually attributed to the synchrotron emission of relativistic electrons. The peak position of the x-ray spectrum provides information about the maximum energy of the electrons in the source. On the other hand, the observed spectrum from GeV to TeV energies are usually described by inverse Compton or bremsstrahlung or π^0 -decay processes. From the correlation study between X-ray and GeV–TeV spectra, it can be understood if the same population of electrons are responsible for observed spectrum at two different energy bands. Moreover, the density of the ambient medium and dominant contribution of the target photon fields for the IC process can be found out. In addition, under certain circumstances the observed spectrum can also be explained by invoking the hadronic spectrum (π^0 decay process) which may provide information about the presence of relativistic protons in the source. Also the total energy supplied to relativistic electrons and protons can be estimated. In short, the origin of galactic cosmic rays and morphology of different potential gamma-ray sources can be established through such multi-waveband studies.

One of the Galactic sources which has been studied extensively in multiple wave bands is the Crab nebula. Multi-wavelength modelling of this source has provided a lot of information about this source such as the magnetic field, presence of different populations of electrons, dominant radiation processes, etc. The details on this can be found, e.g., in Ref. [55]. The complete multi-wavelength spectrum of the Crab nebula is shown in Figure 1.6 for later reference.

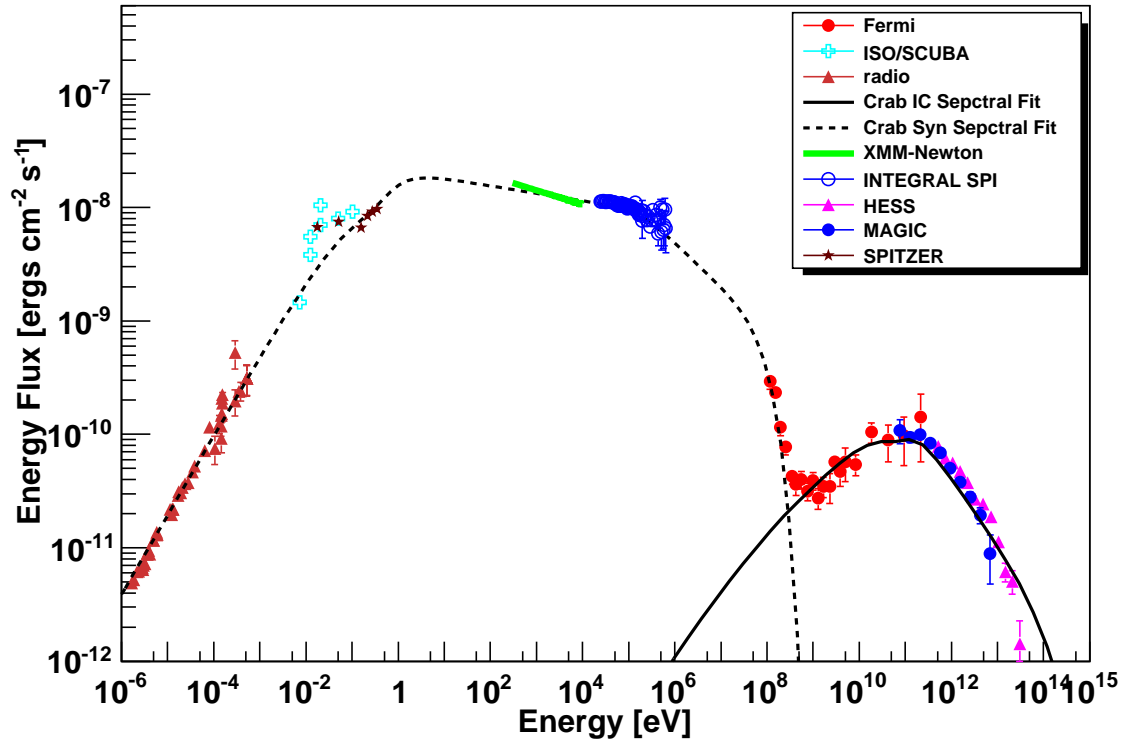


Figure 1.6: Multi-wavelength spectrum of the Crab nebula. Radio [65], SCUBA/ISO [66], SPITZER [67], XMM-Newton [68], INTEGRAL SPI [69] provide observations in radio, submillimeter, far infrared, X-ray and gamma-ray wavelengths, respectively and Fermi-LAT [70] and MAGIC [71], HESS [72] provide observations of very high energy gamma rays in the energy ranges of 50 MeV – 300 GeV and 30 GeV – few tens of TeV, respectively. The spectral fit to the data is done following the electron distribution provided in Ref. [55].

Chapter 2

Atmospheric Cherenkov Technique

When a very high energy (VHE) gamma-ray enters into the Earth's atmosphere, it interacts with atmospheric nuclei and initiates the so-called extensive air shower (EAS) consisting primarily of electrons, positrons and secondary gamma rays, which are produced through many generations of interactions. As the charged particles in the shower move down in the atmosphere with velocities greater than the phase velocity of the light, they cause the atmosphere to produce Cherenkov light. The Cherenkov light of many shower particles illuminates a large circular area with a diameter in the range of 200 m – 250 m on the ground for vertically incident showers. By detecting the Cherenkov light at different locations in the light pool by focusing mirrors with a photomultiplier tube (PMT) at the focal point of each mirror or by big reflectors with a collection of PMTs at focal point of each reflector, directionality and energy of the incident gamma rays are estimated. This technique is known as Atmospheric Cherenkov Technique (ACT) [1]. There are a number of experiments (VERITAS, HESS, MAGIC, etc.) based on this technique, and they are currently operational. One of the experiments, which uses this technique, is the High Altitude GAMMA Ray (HAGAR) telescope system located at Hanle, Ladakh, in the Himalayas. In this Chapter, we shall describe details about the HAGAR system in the context of ACT. This Chapter is organised as follows: details of the ACT are described

in section 2.1, 2.2 and 2.3. Details of HAGAR system are described in section 2.4. Observations and data analysis techniques specific to this system are described in section 2.5 and section 2.6, respectively.

2.1 Cherenkov radiation

When a charged particle passes through a medium with a velocity greater than the phase velocity of light in that medium, then Cherenkov radiation is produced by that medium. Cherenkov radiation was first observed by Marie Curie in the year 1910 as a bluish glow from bottles containing radioactive radium salts dissolved in liquids. However, she assumed this as some kind of luminescence. A series of experiments was carried out by Cherenkov and Vavilov between the years 1934 to 1937 to understand the nature of the radiation. P. A. Cherenkov first showed the anisotropic character of the emission through his experimental work. He also showed that the light was emitted only within a certain angular range in the forward direction [73]. The correct theoretical interpretation of this phenomenon was given by I. E. Tamm and I. M. Frank in 1937 [74]. Cherenkov radiation can be explained with a charged particle moving in a dielectric medium [75]. In the vicinity of its track (see Figure 2.1), at a particular instant in time, for instance, at a point **P**, the electric field of the particle distorts the atoms resulting in induced dipole moments of the atoms. The medium thus becomes polarized about the point **P**. When the charged particle moves on to another point, say **Q**, the elongated atoms around **P** return to their normal shape. This is accompanied by emission of an electromagnetic pulse. For slow moving particles ($v < c_m$, where c_m is the velocity of light in the medium), the polarization is more or less symmetrical w.r.t particle position, as shown in panel (a) of Figure 2.1, resulting in no net electric field at long distances due to destructive interference (and thus no radiation). When the particle is moving with a velocity greater than the velocity of light in the medium ($v > c_m$), polarization is no longer symmetrical. The state is still symmetric about the current position of the particle in the azimuthal plane

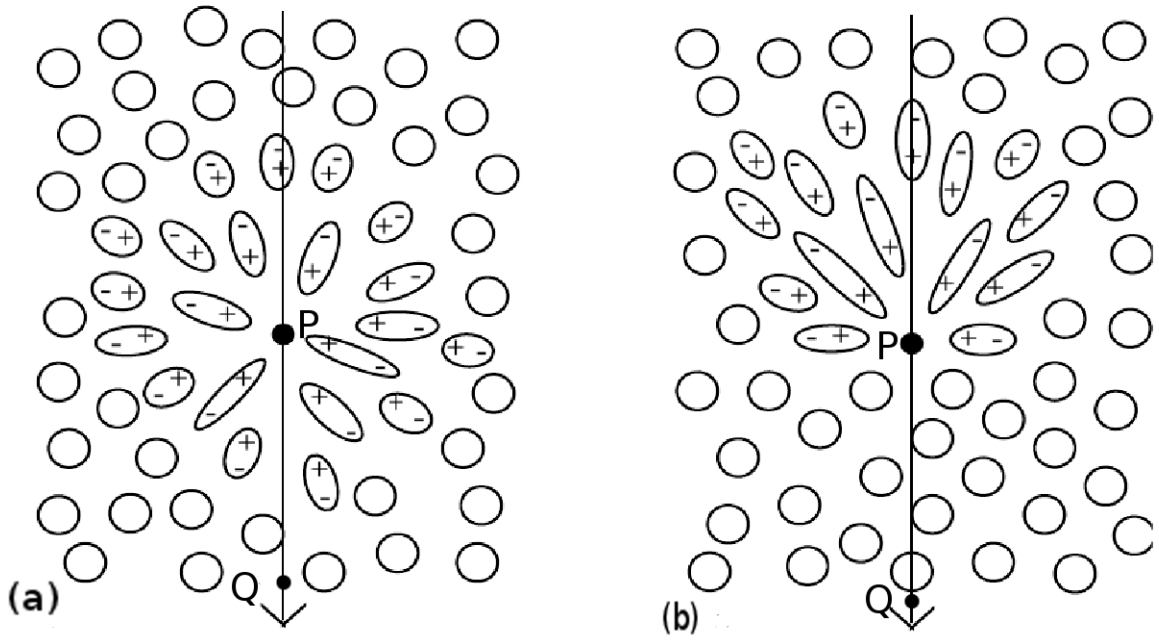


Figure 2.1: Polarization state of the medium when the velocity of the charged particle is (a) less than the phase velocity of light in that medium ($v < c_m$) and (b) greater than the phase velocity of light in that medium ($v > c_m$).

which is plane perpendicular to the trajectory of the particle, but no longer symmetrical in the plane of the trajectory of the particle (see panel (b) of Figure 2.1). Hence, a cone of dipoles develops behind the charged particle. There would now be a distinct dipole field established in the dielectric. When this state collapses, it results in wavelets emanating from all portions of the track, which are in phase, and interfere constructively to produce Cherenkov radiation. Radiation would be emitted perpendicular to the surface of this cone. The Cherenkov radiation is emitted at an angle that depends on the refractive index of the medium and is beamed in the forward direction.

Figure 2.2 shows that this radiation can only be observed at a particular angle θ called Cherenkov angle, with respect to the track of the particle. The Cherenkov angle can be estimated in the following way: consider that a charged particle travels from point A to B (see Figure 2.2) in time δt with a velocity βc , where c is the velocity of light in vacuum. In that time interval, light travels from A to C. The arbitrary points P1, P2 and P3 over the track AB are sources of spherical wavefronts, which are coherent in nature, and they

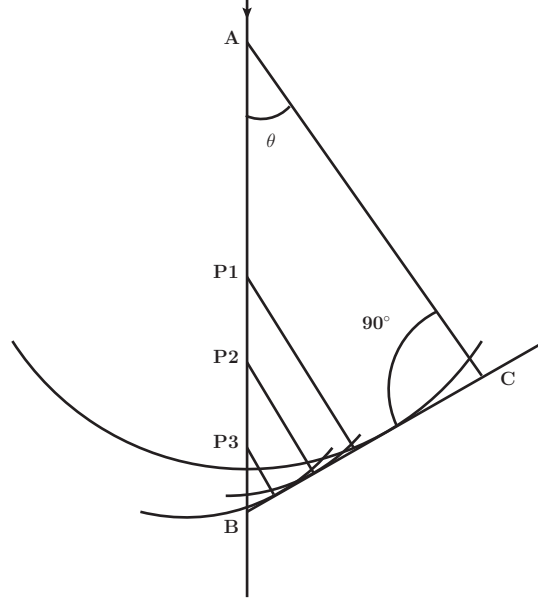


Figure 2.2: Illustration of the coherent nature of Cherenkov radiation.

combine to form a conical wavefront which can be approximated as the plane wavefront BC. The direction of the particle is along AB, and the plane wavefront BC determining the direction of the radiation is perpendicular to AC. The particle traverses a distance of $\beta c \delta t$ in time δt whereas the light travels a distance $c \delta t / n$ (where n is average refractive index of the medium) in the same time interval δt . Therefore, we can write

$$\begin{aligned} \cos \theta &= \frac{AC}{AB} = \frac{\delta t \frac{c}{n}}{\delta t \beta c} \\ &= \frac{1}{\beta n}. \end{aligned} \quad (2.1)$$

Equation (2.1) implies two limiting cases. Firstly, for a given medium of refractive index n there exists a threshold velocity of particles such that, $\beta_{min} = 1/n$, and no radiation takes place if velocity of the particle is less than $\beta_{min}c$. The corresponding threshold energy of

the particle is $E_{min} = \Gamma_{min} m_0 c^2$, where

$$\Gamma_{min} = \frac{1}{\sqrt{1 - \beta_{min}^2}}, \quad (2.2)$$

and m_0 is the rest mass of the particle. Secondly, if the particle moves ultra-relativistically (i.e. $\beta \sim 1$), the Cherenkov angle θ becomes maximum which is to be obtained from the following relation: $\cos \theta_{c,max} = 1/n$. The radiation intensity (W) per unit length (l) can be written as [75]

$$\frac{dW}{dl} = \frac{q^2}{c^2} \int_{\beta c > 1} \omega d\omega \left(1 - \frac{1}{\beta^2 n^2} \right), \quad (2.3)$$

where $q(= Ze)$ is the charge of the particle, e is the charge of the electron and ω is the angular frequency of the Cherenkov light. For practical purposes, radiation intensity per unit length can be expressed as number of Cherenkov photons per unit length. From Eqn. (2.3), it can be shown that the number of photons emitted by a charged particle within the spectral wavelength range of λ_1 and λ_2 is equal to

$$\frac{dN}{dl} = 2\pi Z\alpha \left(\frac{1}{\lambda_2} - \frac{1}{\lambda_1} \right) \left(1 - \frac{1}{\beta^2 n^2} \right), \quad (2.4)$$

where $\alpha(= \frac{e^2 \hbar}{2\pi c})$ is the fine structure constant. Since, $\cos \theta = 1/\beta n$, Eqn. (2.4) can be expressed as

$$\frac{dN}{dl} = 2\pi Z\alpha \left(\frac{1}{\lambda_2} - \frac{1}{\lambda_1} \right) \sin^2 \theta. \quad (2.5)$$

Now, the spectral distribution of Cherenkov photons can be written as

$$\frac{d^2W}{dld\omega} \propto \omega, \quad (2.6)$$

or,

$$\frac{d^2W}{dld\lambda} \propto \frac{1}{\lambda^3}. \quad (2.7)$$

Similarly, the number of photons per unit length per unit wavelength interval can be written as

$$\frac{d^2N}{dld\lambda} \propto \frac{1}{\lambda^2}. \quad (2.8)$$

Emission takes place in visible and near visible region for which $n > 1$. Emission in other wavelengths including x-ray and gamma-ray region is not possible, since for these energies, $n < 1$, which will not satisfy Eqn. 2.1. Thus radiation in X-ray or gamma-ray energies is forbidden. Equation 2.8 reveals that the bulk of the Cherenkov radiation in the optical band is emitted in ultra-violet and visible blue part of the electromagnetic spectrum.

In considering Cherenkov radiation from EAS we must take into account the variation of refractive index as a function of height. The energy threshold for emission of Cherenkov radiation increases with altitude, since the refractive index of air decreases with altitude. The refractive index n at altitude h can be written as

$$n(h) = \delta(h) + 1,$$

where δ depends on the density of air and hence on the altitude, and can be expressed as $\delta(h) = \delta_0 \exp(-h/h_0)$, where the scale height h_0 is 7.1 km and $\delta_0 = 2.9 \times 10^{-4}$. In the atmosphere at ground level at N.T.P., $n \simeq 1.00029$ in the visible range and $\theta_{c,\max}$ is

1.3°. Energy thresholds for Cherenkov emission from electron, muon and proton in the atmosphere are 21 MeV, 4 GeV and 39 GeV, respectively. The light yield for electrons is about $0.3 \text{ photons cm}^{-1}$. In the case of water, $n = 1.33$, and $\theta_{c,\max}$ is $\sim 41^\circ$ and the energy threshold for electron is $\sim 260 \text{ keV}$ and Cherenkov photon yield is $\sim 250 \text{ photons cm}^{-1}$. The Cherenkov photons from the air shower induced by a gamma-ray or a cosmic ray are distributed over a large area and form a circular pool of light of about 150 – 200 m radius. The size of this light pool is determined by the altitude of the emission and Cherenkov emission angle at that altitude. The Cherenkov light reaches the ground in a narrow time window, typically of about 5 ns width.

2.2 Extensive air shower (EAS)

Detection of the VHE gamma rays by satellite based detectors is limited by the size of the detectors as well as the steeply falling spectrum of cosmic gamma rays. Direct detection, on the other hand, of the VHE gamma rays by ground based telescopes is not possible due to atmospheric absorption. Gamma rays and charged particles initiate EAS when interacting at the top of the atmosphere. Cherenkov photons produced in the EAS can be detected by ground based telescopes, since the Cherenkov emission suffers little absorption in the atmosphere. In this case the atmosphere plays a significant role in detection of those gamma rays. Details about the EAS generated by both gamma rays and charged particles are described below.

2.2.1 Gamma-ray initiated air shower

When a gamma-ray enters into the Earth's atmosphere, it interacts with nuclei, and initiates an electromagnetic shower of charged particles (e^+ and e^-) and photons. In this interaction, an electron-positron (e^+e^-) pair is produced. This pair moves further down in the atmosphere and radiates through the bremsstrahlung process. The photons so pro-

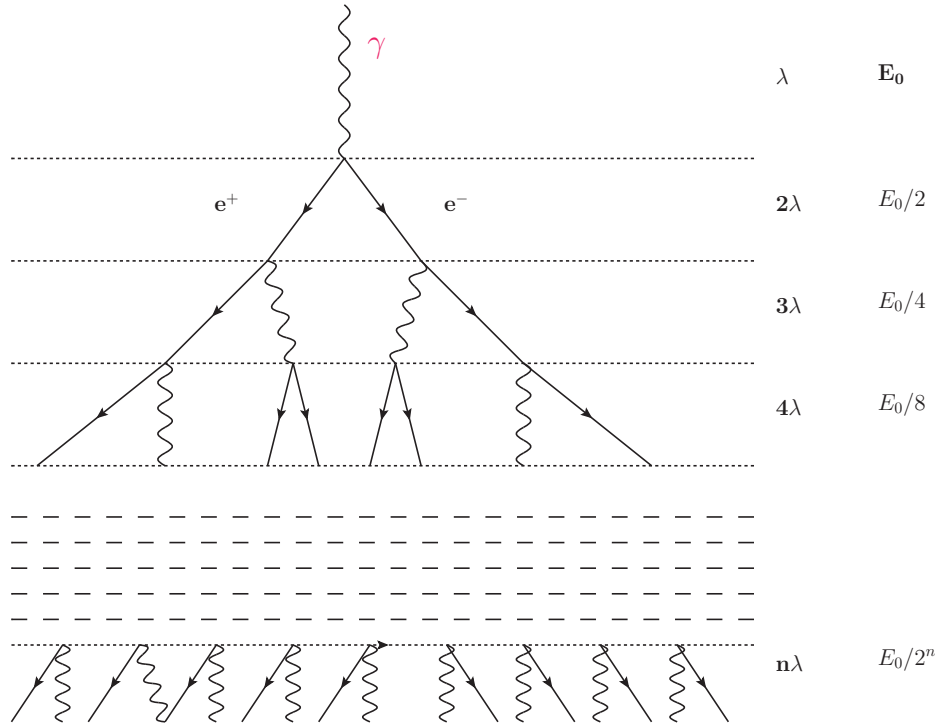


Figure 2.3: Simplified schematic of extensive air shower initiated by a cosmic gamma-ray.

duced further produce e^+e^- pairs. This process continues until the energy of the secondary photons is reduced to a value below which no e^+e^- pair production is possible, the shower development reaches its maximum and then it diminishes. Various information about the shower can be obtained using a simple toy model. It is assumed that in each electromagnetic interaction two particles are produced. Hence, after n radiation lengths there will be 2^n particles. At an atmospheric depth of X from the first interaction point, n can be written as $n = X/\lambda$, where λ is the mean radiation length. Hence, the number of charged particles at that position is $N(X) = 2^n = 2^{X/\lambda}$. The width of the shower along the horizontal direction will become maximum when the losses due to ionization is equal to losses due to bremsstrahlung for e^+e^- and the energies of those secondary photons or particles reach a critical energy, E_c . At this point the cascade will have maximum number of particles and hence the shower size becomes maximum. From this point onwards energy losses due to ionization and absorption become dominant for e^+e^- and the number of particles gradually decreases and the cascade dies away. If E_0 is the energy of the incident gamma-ray, then E_c can be written as $E_c = E_0/N(X_{max})$, where X_{max} is the maximum

value of atmospheric depth where shower width becomes maximum. Therefore, X_{max} can be expressed as $X_{max} = \lambda \ln(E_0/E_c)/\ln(2)$. The critical energy E_c is 81 MeV in the air for e^+e^- . The schematic diagram of the development of air shower initiated by a gamma-ray is shown in Figure 2.3.

2.2.2 Cosmic ray initiated air shower

A cosmic ray particle (proton or heavier nucleus) interacting with atmospheric nuclei produces mesons and baryons. These particles move down in the atmosphere and further interact with air molecules and produce the particles similar to those produced in the first interaction. Neutral pions (π^0 s), which are the lightest mesons, decay into gamma rays ($\pi^0 \rightarrow 2\gamma$), which then produce electromagnetic showers in the same way described above for a gamma-ray interacting at the top of the atmosphere. On the other hand, some of the charged particles such as pions and kaons decay depending on the relativistic time dilated mean free path. The charged pions produce showers of various charged particles through the decays into muons, neutrinos, neutral pions and electrons ($\pi^\pm \rightarrow \mu^\pm + \nu_\mu(\bar{\nu}_\mu)$ and $\mu^\pm \rightarrow e^\pm + \nu_e(\bar{\nu}_e) + \bar{\nu}_\mu(\nu_\mu)$). Kaons decay via two different channels into muons, neutrinos, or mesons ($K^\pm \rightarrow \mu^\pm + \nu$, or $K^\pm \rightarrow \pi^\pm + \pi^0$). In addition, nuclear cascade is produced through various interactions of baryons. Hence, a cosmic ray proton initiated shower mainly consists of three components: electromagnetic, hadronic and muonic components. It is to be mentioned that if a large fraction of proton energy goes to the π^0 s, then the shower can resemble a shower induced by a gamma-ray, and they cannot be easily separated from gamma-ray induced showers. In addition, the showers initiated by cosmic ray electrons behave as gamma-like showers, and they constitute irreducible background for ACT. Since the flux of cosmic ray electrons is low and falls rapidly with energy, the electron background is not very significant above 100 GeV.

In the case of cosmic ray initiated shower, X_{max} also depends on the energy of the primary cosmic ray the same way as that of a gamma-ray shower. A schematic diagram of shower

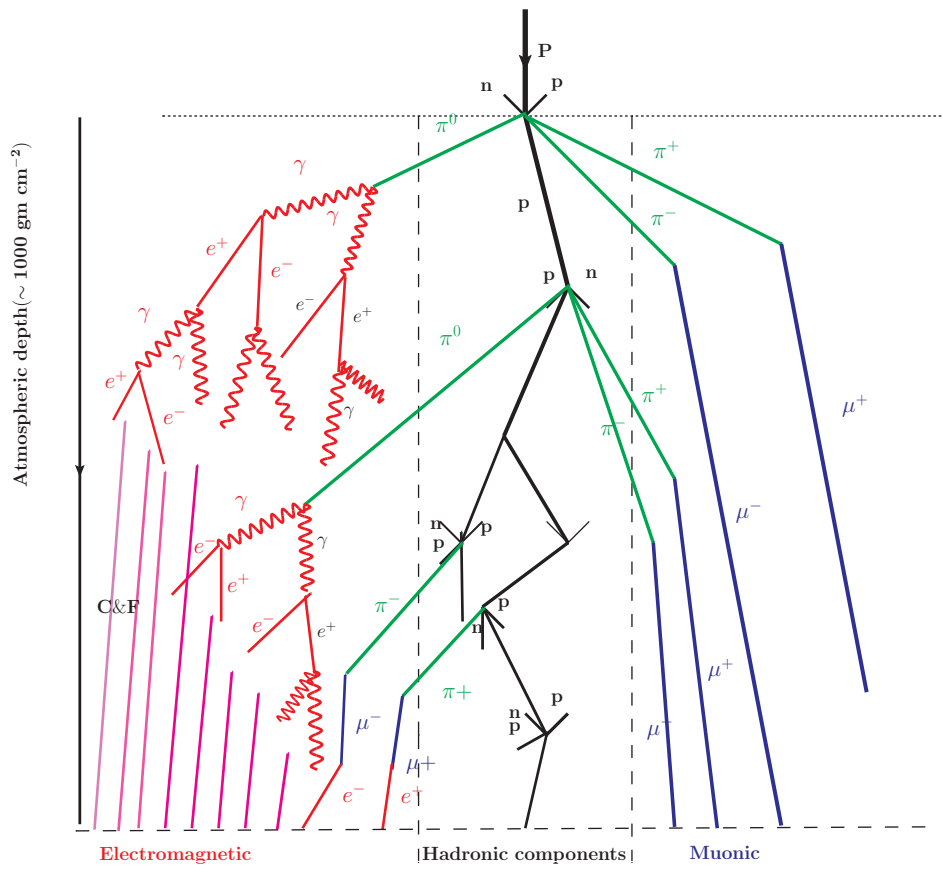


Figure 2.4: Air showers initiated by a cosmic ray proton.

development by a cosmic ray proton is shown in Figure 2.4.

2.2.3 Differences between gamma-ray and hadron induced showers

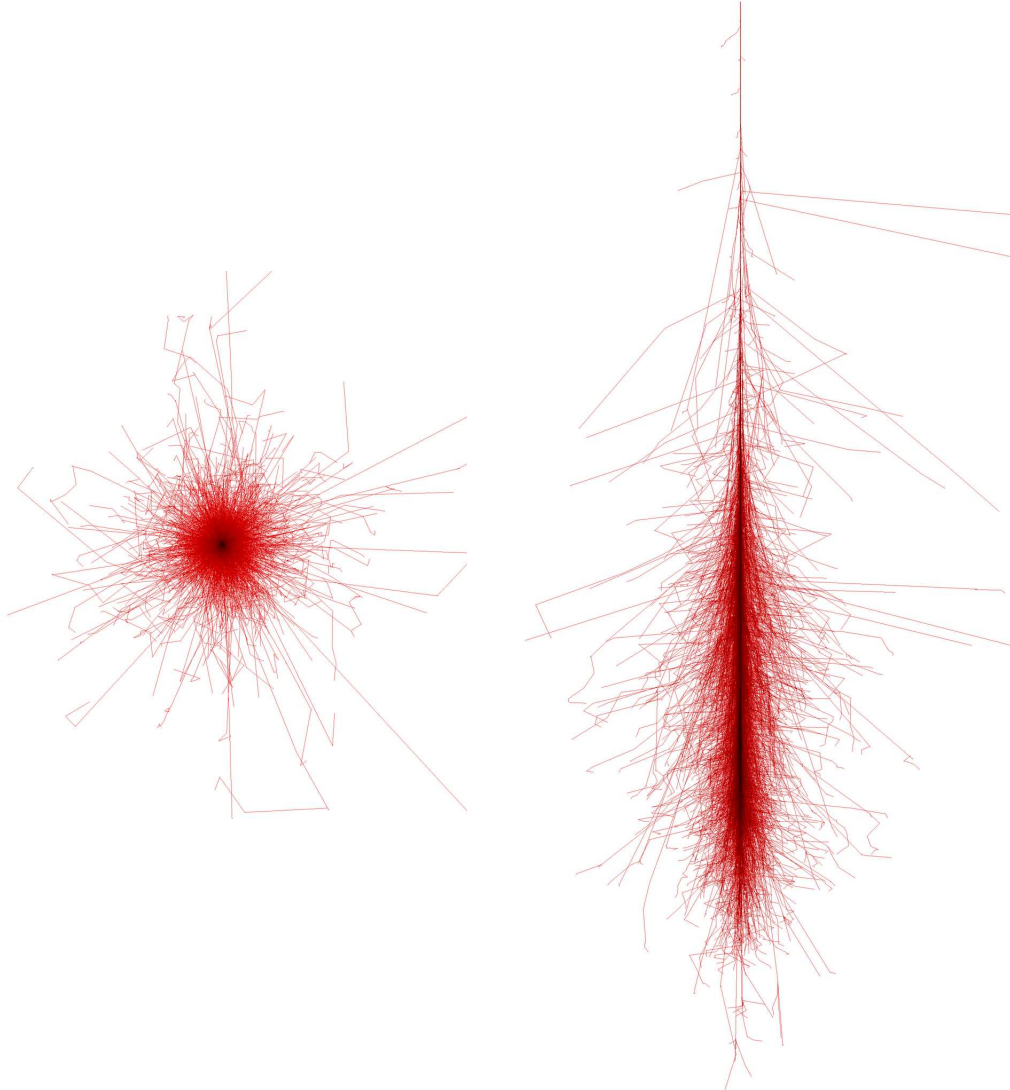


Figure 2.5: xy (left) and xz (right) projections of simulated EAS induced by a 100 GeV gamma-ray, when projected along z and y respectively. These shower images have been produced by F. Schmidt and J. Knapp at University of Leeds (2005); <http://www-zeuthen.desy.de/~jknapp/fs>

Both gamma-rays and cosmic rays initiate EAS in the atmosphere. However, there are significant differences in the development of showers initiated by gamma rays and cosmic rays. Cosmic ray initiated showers contain electromagnetic cascades, muonic cascades and nuclear cascades, whereas gamma ray initiated showers contain only electromagnetic

showers, as mentioned above. The density fluctuations of Cherenkov photons for hadronic showers are significantly larger than those gamma-ray showers. In the case of proton initiated showers, electrons are produced by the decays of π^0 s along with muons which are secondary products of charged mesons. The fluctuations in the multiplicities of the pion secondaries combined with the fluctuations due to larger mean free path of protons lead to larger electron number fluctuations which in turn gives higher density fluctuations in Cherenkov photon density. Hence, the development of hadronic EAS is more irregular compared to that of gamma-ray EAS as shown in Figures 2.5 and 2.6. The Cherenkov light pool from gamma-ray initiated showers is more uniform compared to that of cosmic ray showers. Since cosmic rays develop three different cascades, density of Cherenkov light on the ground becomes non uniform (see Figure 2.7). A hump like structure is also found in the lateral distribution of Cherenkov photon density produced by gamma-ray showers as shown in Figure 2.8 [76]. In the case of hadronic showers, this feature is absent. However, as we go to higher altitudes the discrimination between hadronic shower and gamma-ray shower based on this hump like feature gets diluted. Moreover, one of the distinct features of cosmic ray shower is the presence of muons in the EAS. Since, occasionally muons in cosmic ray showers survive at the detector level and they are able to produce Cherenkov light, therefore, the width of Cherenkov wavefront from cosmic rays is larger than that of gamma-ray showers. Also as mentioned earlier, because of larger non-uniformity in cosmic ray showers, these showers show larger fluctuations in Cherenkov photon density and larger arrival time jitter compared to gamma-rays showers.

In addition, the timing profiles of Cherenkov light pool generated by a gamma-ray shower and a hadronic shower are different. In general, Cherenkov wavefront resulting from gamma-ray shower has a concave timing profile, since the light striking at large radii on the ground has to travel a longer distance than the light near the center of the light pool. On the other hand, a hadronic shower is a mixture of several sub-showers, hence timing profiles of these showers give a very irregular shape at the ground level as shown in Figure 2.9. Based on these differences cosmic ray events can be distinguished from the

gamma-ray events.

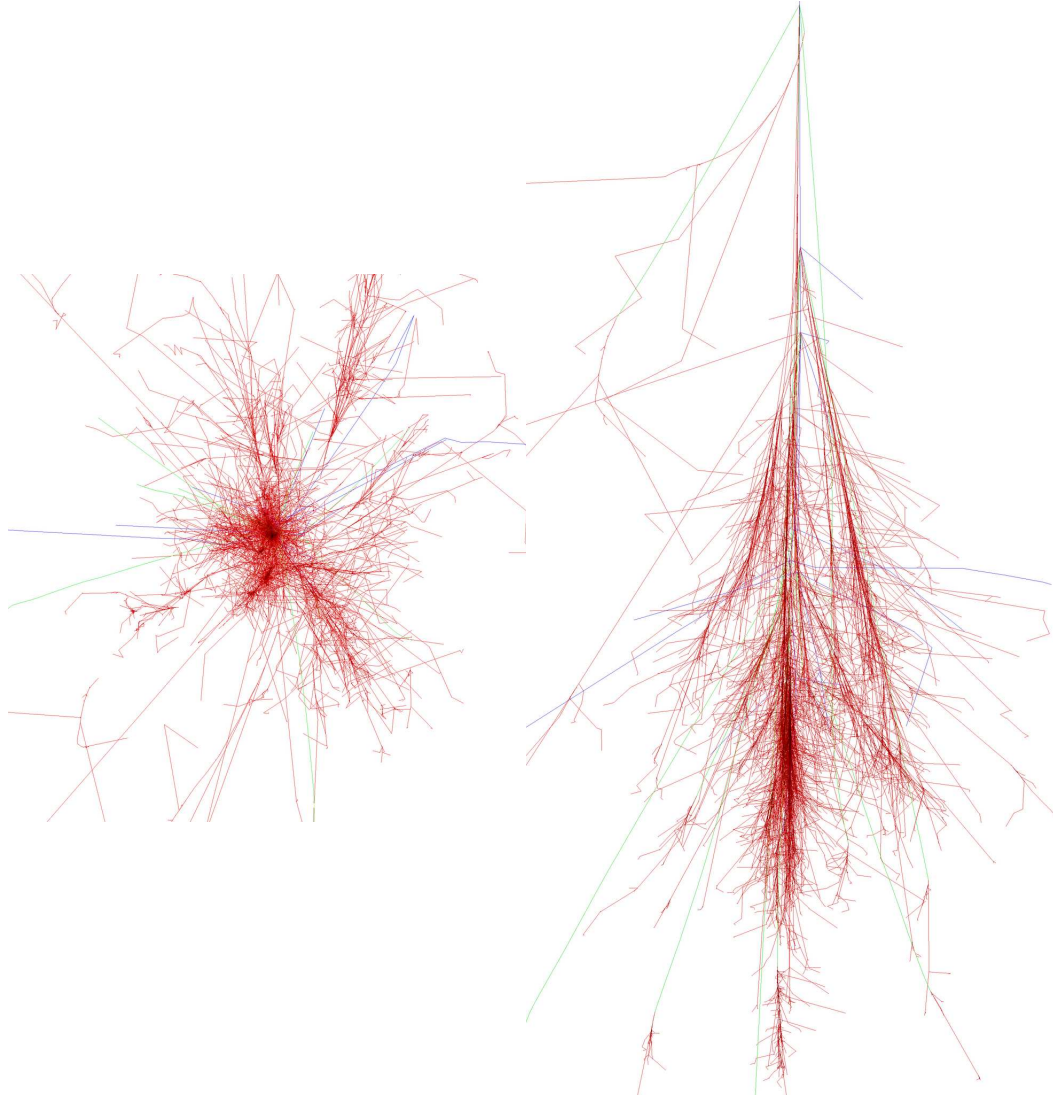


Figure 2.6: xy (left) and xz (right) projections of simulated EAS induced by a 100 GeV proton, when projected along z and y respectively. These shower images have been produced by F. Schmidt and J. Knapp at University of Leeds (2005); <http://www-zeuthen.desy.de/~jknapp/fs>

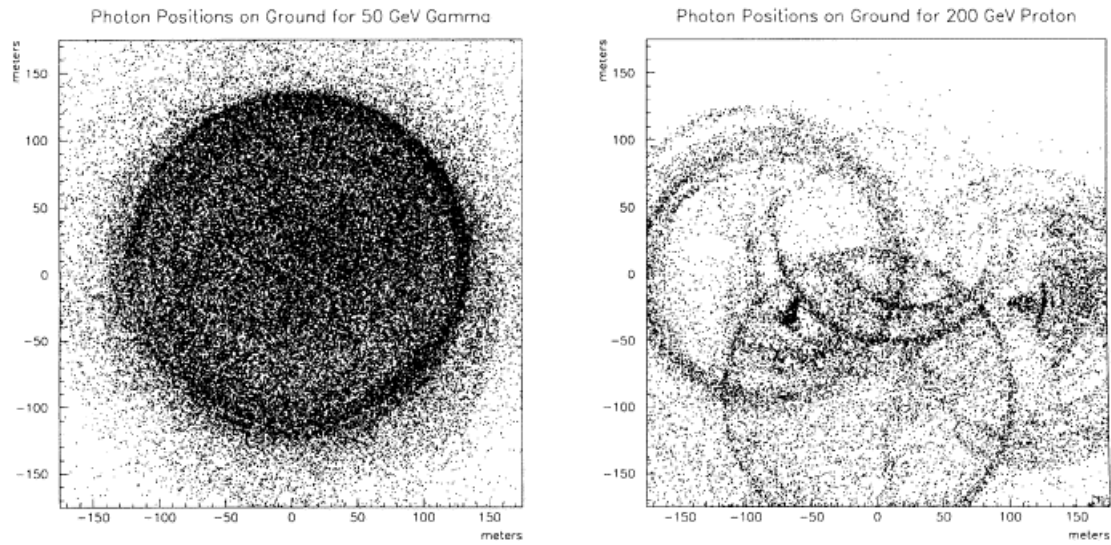


Figure 2.7: Position of Cherenkov photons on the ground, which are produced by a 50 GeV gamma-ray induced shower (left panel) and a 200 GeV cosmic ray proton induced shower (right panel). Each dot represents a photon hitting the ground [77].

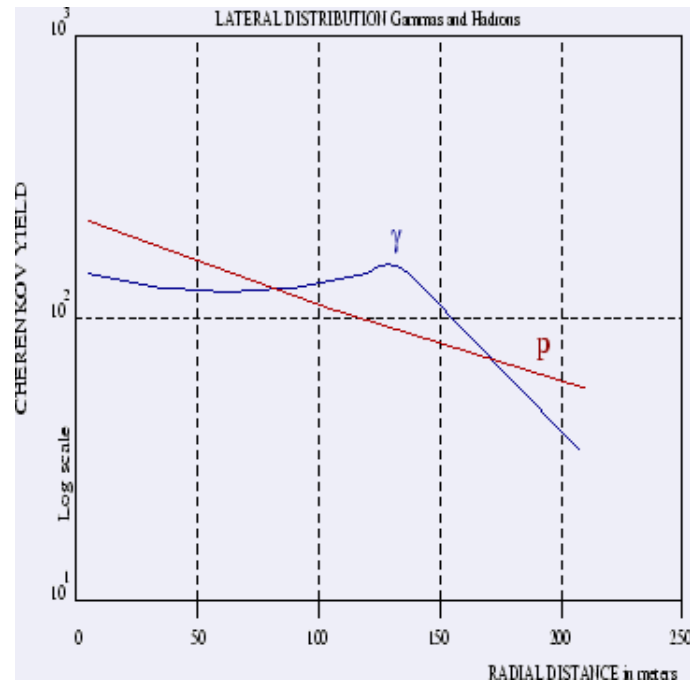


Figure 2.8: Lateral distribution of Cherenkov photons on the ground for both gamma- and cosmic ray showers [46].

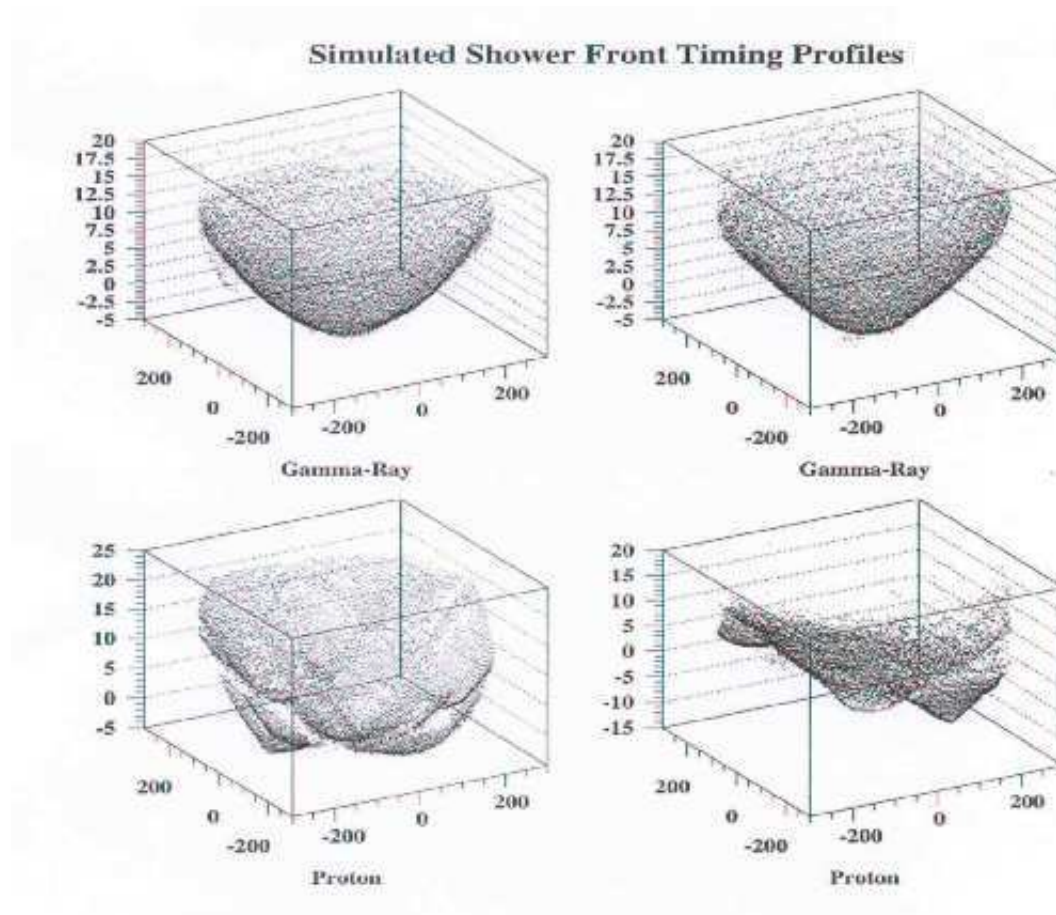


Figure 2.9: Lateral timing profiles of the arrival times of the shower wavefronts at different locations are shown for gamma-ray and proton showers. The timing profiles of proton are more irregular than that of gamma-ray showers. The horizontal axes are positions on the ground, in meters, while the vertical axes are arrival times in nanoseconds. This figure is taken from [78].

2.3 Detection Technique

Gamma rays are considered to span a large range of energies (10^6 eV - 10^{20} eV), which is divided into different energy regions. Although there is no confirmed detection of gamma rays above 10^{14} eV, photonic origin of cosmic-ray events detected beyond the so-called GZK cut-off ($\sim 10^{19}$ eV) cannot be excluded. Accordingly different detection techniques are required for detection of gamma rays of different energy ranges. Gamma-ray astronomy in the range of 10^{11} to 10^{13} eV is performed through detection of Cherenkov photons at the ground level and the corresponding detection technique is termed as *Atmospheric Cherenkov Technique* (ACT). For gamma rays in this energy range, the particles/photons constituting the EAS may or may not reach observation level depending upon the observation height. However, the Cherenkov photons reach observation level due to very little absorption in the atmosphere. But for gamma rays with energies above 10^{13} eV, the particles from EAS are able to reach the detectors at ground and can be detected by particle detectors at the ground level. Here, we will discuss the detection technique of Cherenkov photons rather than the charged particles at the ground level. Details about the ACT can be found in a review by Cawley and Weekes [79] and others [77, 80, 81].

2.3.1 Wavefront Sampling Technique

A charged particle travelling in the atmosphere produces Cherenkov radiation if its velocity is greater than the velocity of light in that medium. When a cosmic ray or gamma-ray enters into the Earth's atmosphere it produces showers of secondary charged particles as mentioned earlier. The Cherenkov light from these secondary particles creates a light cone on the ground. Cherenkov photons are collected by optical reflectors with a PMT at the focal point of each reflector. The Cherenkov photons are sampled from different locations of the Cherenkov light pool. Therefore, an array of detectors separated by distances in the range of 10 m to 100 m is required to collect Cherenkov photons in coincidence.

The arrival direction of the shower is determined by the relative time of arrival of the Cherenkov shower front at the individual detectors.

2.3.2 Imaging Technique

In this technique, Cherenkov photons are collected by a camera which is kept in the focal plane of a large reflector. The camera consists of a matrix of PMTs which act as pixels in the camera. The density of photons in all the pixels in the camera is mapped to form an image of the shower. The idea of capturing an image of the atmospheric air shower came from optical astronomy. A snapshot of an air shower was first realized by Hill and Porter in 1960 [82]. They used an image intensifier system, triggered by amplified pulses from a ~ 12 cm PMT. A Schmidt mirror with diameter of 30 cm and of aperture $f/0.5$ was used in this system. Their results raised the possibility of using the imaging technique for detection of gamma-ray showers. A typical image of a gamma-ray shower is shown in Figure 2.10. The shape of the image is elliptical. In case of multiple telescopes the direction of the shower axis is estimated from the point of intersection of major axes of the images and optical axes of the telescopes (see Figure 2.11). In addition, more information about the shower can be found from the shape of the images. The image of a shower was first characterised by Michael Hillas [83] to obtain the arrival direction of the shower, energy of the primary particle, etc. The image is approximated by an ellipse as shown in Figure 2.12 where the semi-major and semi-minor axes reflect the length and width parameters and represent the shape of the captured image. The ‘alpha’, ‘miss’ and ‘azwidth’ parameters (see Figure 2.12) relate to the orientation or pointing of the image. The ‘distance’ parameter is a measure of the position of the image centroid with respect to the centre of the camera’s field of view. The size of the image is proportional to the density of the Cherenkov photons, hence the energy and the position where the photons are hitting on the ground. Therefore the shower energy is estimated from the image size and nominal distance. Michael Hillas [84] also showed that the above parametrization of

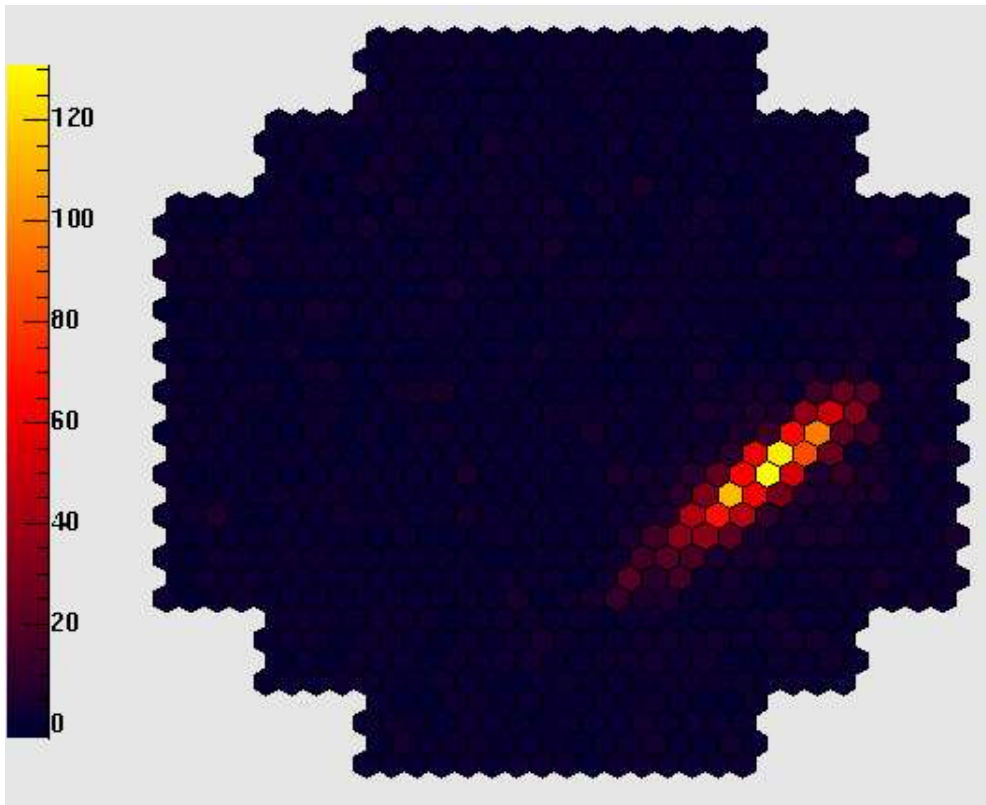


Figure 2.10: Snapshot of a typical image of a shower. This figure is taken from [86].

the shower images can be used to discriminate between gamma-ray and hadron initiated showers. This parametrization led to the first 9σ detection of the Crab nebula by the Whipple team in 1989 [41].

The Cherenkov images that result from a typical gamma-ray shower are elliptical and compact with an orientation that points towards the center of the field of view, whereas the Cherenkov images from cosmic ray showers are much more irregular and are randomly oriented in the focal plane of the imaging camera. The detailed Monte Carlo simulations are used to distinguish between the images that result from gamma-ray and cosmic ray initiated showers. The widths of the hadron initiated air showers are significantly wider than the corresponding gamma-ray initiated showers due to the large transverse momentum in hadronic interactions. Figure 2.13 shows the distributions of different Hillas parameters for gamma-ray and cosmic ray showers, and these indicate that the discrimination of cosmic ray events is possible on the basis of Hillas parameters [85].

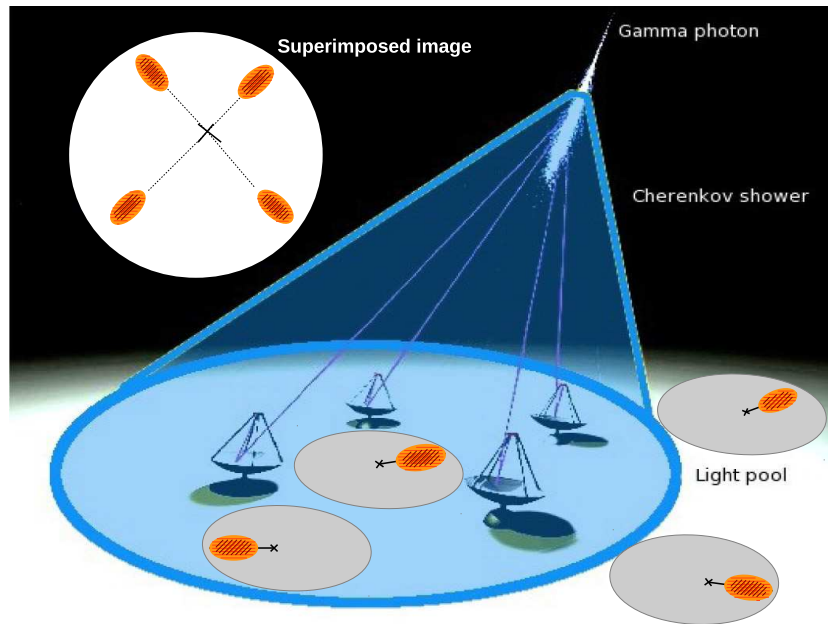


Figure 2.11: Response of an array of four detectors to air shower.

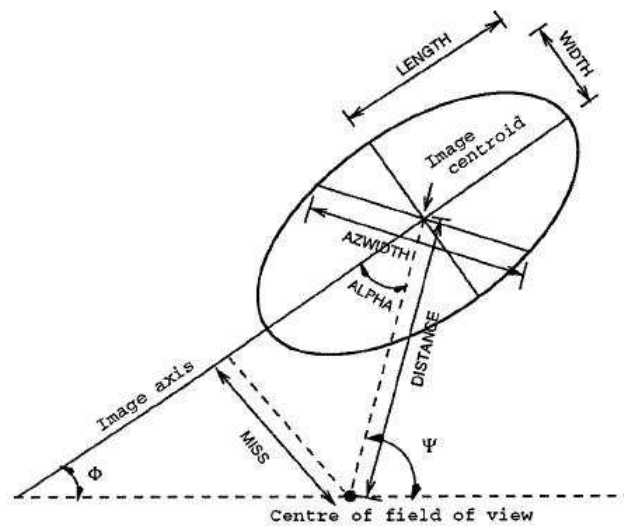


Figure 2.12: Hillas parameters to describe a shower image [85].

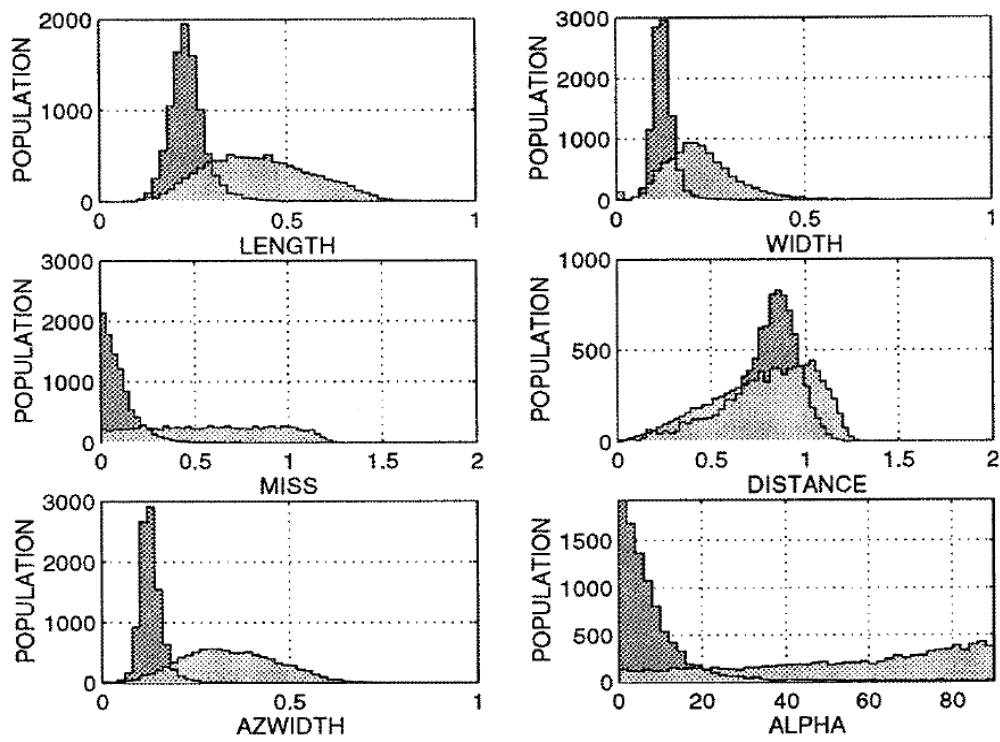


Figure 2.13: Distribution of Hillas parameters for gamma-ray and cosmic ray initiated showers. This figure is taken from [84].

2.4 HAGAR Array

The HAGAR array [87] consists of seven telescopes of which six are placed at the corners of a hexagon, with the seventh one placed at the center of the hexagon (see Figure 2.14). The telescopes are separated by 50 m from each other. Each telescope consists of seven front coated parabolic mirrors (see Figure 2.15), each of diameter 0.9 m, and with f/d ratio of 1. All the seven mirrors of each telescope are mounted para-axially on a single platform while the telescopes themselves are mounted alt-azimuthally. A photo multiplier tube (PMT) of type XP2268B manufactured by Photonis is kept at the focus of each mirror. The diameter of PMT photo cathode defines the field of view to be 3° at FWHM. This PMT has good sensitivity to photons in the ultraviolet to blue range, with a peak quantum efficiency of about 24 % at 400 nm. The HAGAR system can be broadly divided into two sub-systems: (a) Telescope control system and (b) Data acquisition system.

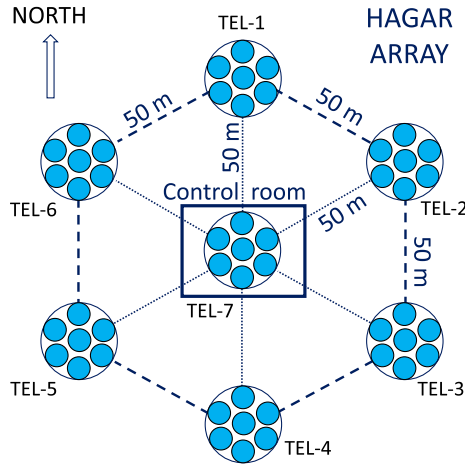


Figure 2.14: A schematic diagram of HAGAR telescope array setup.

2.4.1 Telescope Control System

Each of the telescope axes is driven by a stepper motor. The telescope movement control system consists of two 17-bit Rotary encoders, two stepper motors and a micro-controller

based Motion Control Interface Unit (MCIU). Steady state pointing accuracy of the servo is ± 10 arc-sec with maximum slew rate of 30 deg/minute. The resulting blind spot size while tracking the stars near zenith is found to be less than 0.6 deg. The telescope movement is manoeuvred by a control software written on a Linux platform. The pointing of the telescope is continuously monitored and corrected in real time during tracking [88]. The schematic of the telescope control system is shown in Figure 2.16.



Figure 2.15: One of the telescopes of the HAGAR array.

2.4.2 Data acquisition system (DAQ)

The HAGAR DAQ electronics can be divided into two parts, front end electronics (NIM) and the back end electronics which consists of CAMAC, VME.

The seven PMT pulses of a telescope are linearly added to form a telescope output called the Royal Sum (RS) pulse. The corresponding information of the RS pulses from each telescope are recorded. Information of the triggered telescopes and other house-keeping information are also recorded. In addition to the main DAQ system, a parallel DAQ (ACQIRIS make model DC271A) using commercial waveform digitizers with a sampling rate of 1 GS/s is also used.

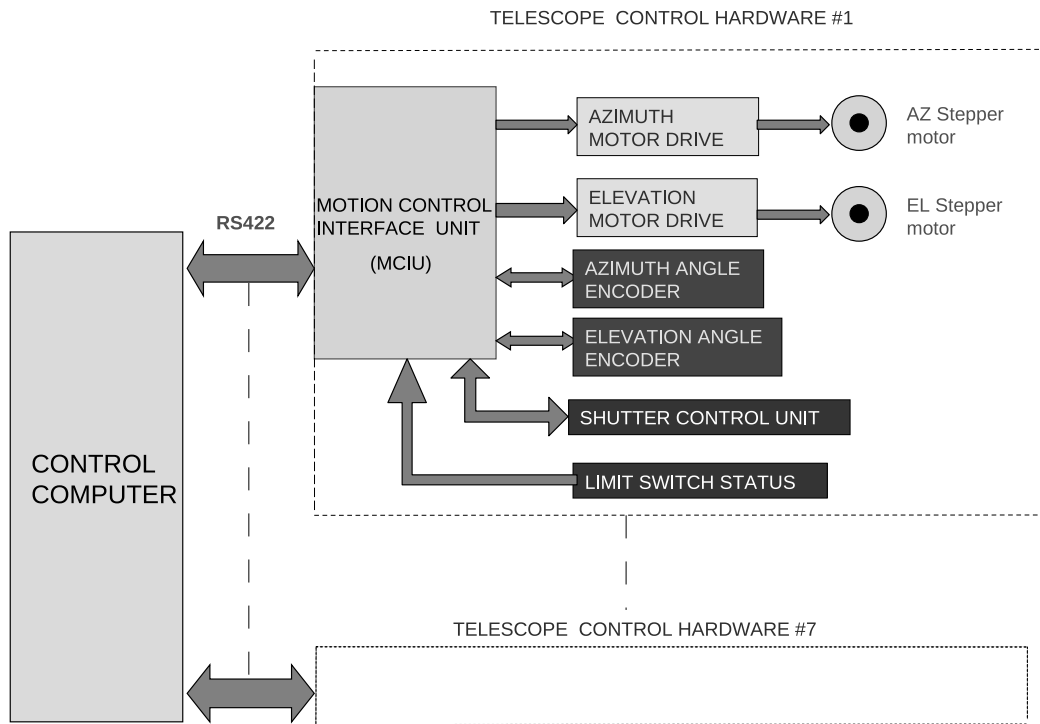


Figure 2.16: A schematic diagram of the HAGAR telescope control.

High voltages fed to PMTs are controlled and monitored using C.A.E.N controller (model SY1527). Pulses from the PMTs are brought to the control room situated below the central telescope via coaxial cables of length 85 m and of types LMR-ultraflex-400 (of length 30 m) and RG 213 (of length 55 m). The fast pulses from each of the seven PMTs of a telescope are amplified 10 times using an amplifier module. Amplified PMT pulses for each telescope are added to form the royal sum (RS) pulse using a Fan-in/Fan-out module. For trigger formation, the analog addition of pulses from seven PMTs of each telescope is performed within an accuracy of 1 ns to get seven telescope RS pulses, and they are given as inputs to the HAGAR trigger logic module. In this module, an event trigger is generated if there is a coincidence of at least 4 RS pulses out of 7, above a pre-assigned threshold, within a time window of 150 ns to 300 ns depending on the zenith angle of the pointing direction. The coincidence window of 150 ns is used up to zenith angle of 30 degrees, whereas the coincidence window of 300 ns is used for zenith angle within 30-60 degrees. This is calculated taking into account the extent of HAGAR array. The RS discriminator biases are adjusted to keep the RS rates within 25–35 kHz to maintain

a chance coincidence rate within a few percent of the trigger rate. Chance coincidence arises due to night sky background (NSB), PMT noise etc. Once a trigger is generated the CAMAC controller initiates data recording process. Information regarding pulse height or photon density are given by Charge-to-Digital Converters (QDCs) and relative arrival times of pulses are given by Time-to-Digital Converters (TDCs). TDC start pulses are generated from an event trigger. PMT pulses from different telescopes arrive at different times because of the different heights of the telescopes and the arrival angle of the shower front. Moreover, there is a small but finite delay required to form the trigger. Hence, PMT and RS *start* pulses are suitably delayed before they are fed into individual TDC stops. These are generated using discriminator outputs which are delayed using ECL-based digital delays. Philips TDC modules which have resolutions of 0.25 ns per count are used to get relative arrival delays of the PMT and RS pulses. The Cherenkov photon density at each telescope, given by the total charge in PMT pulses, is recorded using 12 bit QDCs. A Common QDC gate is also generated on event trigger. Analog RS pulses from a Fan-in/Fan-out module are delayed using cables and taken to Phillips QDC module. Apart from this, various rates are recorded every second for monitoring purposes using monitoring scaler modules. These include PMT rates, RS rates, trigger rates, chance rates, single-telescope rates, NSB rates etc. In experimental runs, gains of individual PMTs are adjusted for a PMT rate of 5 kHz for a discriminator bias of 150 mV, i.e. for pulses with amplitude above 150 mV. Equality of the PMT rates ensures equal efficiency for each channel. An absolute arrival time of an event accurate to μs is given by a Real Time Clock (RTC) module synchronized with GPS. In addition to the main DAQ system, a parallel DAQ (4 channel modules of ACQIRIS make model DC271A) using commercial 8 bit waveform digitizers with 1 GHz bandwidth with 50 ohm resistance and a sampling rate of 1 GS/s is also used. The seven RS pulses from the seven telescopes are input to this module. This enables us to study the pulse shape, use gamma-hadron separation parameters based on pulse shape and also reduce the NSB contribution by restricting the time window around the Cherenkov pulse. The diagrams showing all the modules of the

telescope electronics and trigger distribution in DAQ are shown in Figure 2.17 and Figure 2.18, respectively.

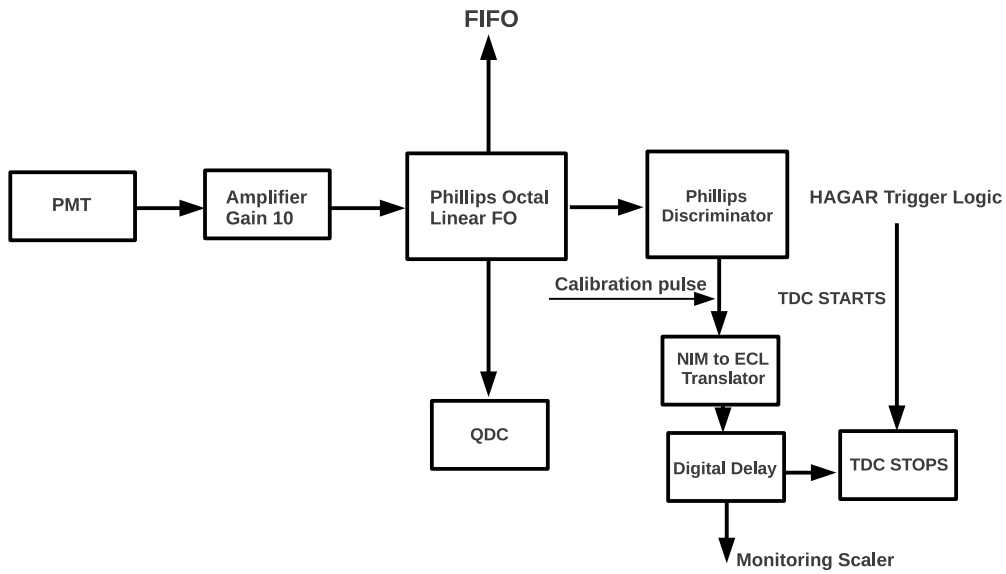


Figure 2.17: Flowchart of telescope electronics in the HAGAR DAQ.

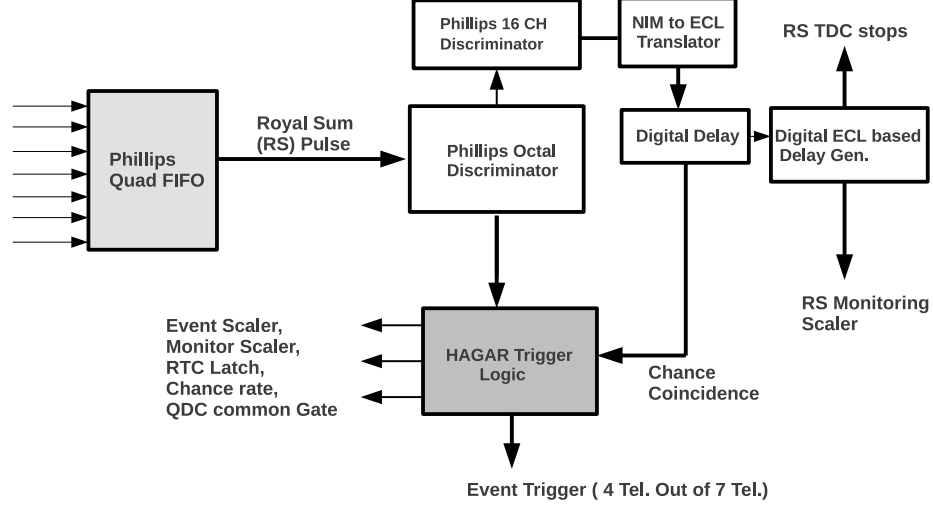


Figure 2.18: Flowchart of trigger setup and its distribution in the DAQ.

2.5 Observations

Observations of celestial sources with the HAGAR telescope array are restricted to moonless nights. We take observation of about 15–20 days before full moon. We take the following three types of runs in each season.

2.5.1 Fixed-angle run

When all the telescopes point towards a particular direction in the sky without tracking any source, the corresponding observation run is called a *fixed-angle run*. This run is required to calibrate the time-offsets of the telescopes. If the telescopes point towards zenith, then the run is called a *vertical run*. For vertically incident showers, delays in timing information in all the telescopes should be zero. But, practically that does not happen due to unequal cable lengths, differences in heights of the telescopes, delays in

propagation, photo-multiplier transit times, etc. Therefore, fixed-angle runs are essential to make corrections in the relative delays in the arrival of Cherenkov pulses for different channels. In addition to *vertical run*, we also take 10 degree north (10N), 20 degree north (20N), 10 degree south (10S), and 20 degree south (20S) runs as fixed-angle runs. Different fixed-angle runs are used for analysis of different sources depending upon their declinations during transit.

2.5.2 ON-source run

When all the telescopes point towards a gamma-ray source in the sky, the corresponding run is called *ON-source* run. Each source run is taken for a period of 40–80 minutes depending on the transit time of the source in a particular observation night.

2.5.3 OFF-source run

Each ON-source run is followed (or preceded) by an *OFF-source* run. During *OFF-source* observation all the telescopes point towards a position in the sky where no known source is present. The zenith angle for this observation run is kept the same as that of the corresponding source run. This is to ensure that the energy threshold of the system for all the incident showers is more or less the same. The duration of the *OFF-source* run is normally 40 minutes.

2.6 Data Analysis

The arrival time of the Cherenkov wavefront is recorded during observations. The arrival angle of each shower is then estimated from the differences in arrival times of Cherenkov photons in different telescopes in the array. Details on the analysis procedure are described below.

2.6.1 TZERO (t_0) estimation

To calibrate the system, we first need to find out the offset in time for each of the telescopes for a triggered event. Time offsets come from the differences in heights of the PMTs, cable delays, response of the PMTs, PMT time jitters, and delays in the electronics. Hence, we need to correct for these time offsets. The relative time difference, t_{ij} , between two telescopes i and j is expressed as

$$t_{ij} \equiv t_{0i} - t_{0j}, \quad (2.9)$$

where t_{0i} and t_{0j} are the time offsets for the telescope i and j , respectively. Here i and j run from 1 to 7. Values of t_{ij} 's are obtained from the fixed-angle runs or vertical runs. For different sets of telescope pairs we have different measured t_{ij} values ($t_{ij}^{measured}$). We estimate the relative time offset for each telescope by minimizing the total χ^2 defined as

$$\begin{aligned} \chi^2 &= \sum_{i,j=1;i \neq j}^7 w_{ij} (t_{ij}^{measured} - t_{ij}^{theoretical}) \\ &= \sum_{i,j=1;i \neq j}^7 w_{ij} (t_{ij}^{measured} - t_{0i} + t_{0j})^2, \end{aligned} \quad (2.10)$$

where w_{ij} s are statistical weight factors which are taken to be the estimated 1σ error on the mean of the measured t_{ij} distribution for the given telescope pair i, j ($i \neq j$). Demanding

$$\frac{\partial \chi^2}{\partial (t_{0i})} = 0, \quad (2.11)$$

we get a set of 7 equations of the form

$$\sum_{i,j=1;i \neq j}^7 w_{ij} (t_{0i} - t_{0j}) = \sum_{i,j=1;i \neq j}^7 w_{ij} t_{ij}^{measured} \text{ for } i = 1, \dots, 7. \quad (2.12)$$

This set of equations can be easily manipulated to eventually yield a set of six coupled equations for the 7 unknowns t_{0i} ($i = 1, \dots, 7$). Therefore, six of the t_0 values are estimated

w.r.t. the 7th one. In our data analysis method we estimate time offsets for 6 telescopes considering t_0 values for the central telescope as the reference time offset.

2.6.2 Space Angle estimation

Our main aim is to find the directions of the incident gamma rays, which are obtained from the timing information of the Cherenkov wavefront at different telescopes. Therefore, we need to calculate the direction cosines of the incident showers. In principle, the arrival angle of a shower can be estimated from the difference in arrival of Cherenkov photons at two different telescopes. To estimate that angle, Cherenkov wavefront is approximated as a plane wavefront. Referring to Figure 2.19, consider that the Cherenkov wavefront BC is at an angle θ w.r.t horizontal plane, and A, B are the positions of two telescopes. If δt is the difference in arrival time of the wavefront at telescopes A and B, then we can write θ as,

$$\sin \theta = \frac{c \delta t}{D}, \quad (2.13)$$

where D is the distance between the two telescopes. For vertically incident shower, the value of θ is zero, which means that the shower front reaches all the telescopes simultaneously. Since, we have an array of telescopes, we have to use all the timing information of a shower front together to estimate the angle θ . If l, m, n are the direction cosines of an incident shower, and t_i is the arrival time of the shower front at the i th telescope then we can write

$$lx_i + my_i + nz_i + c(t_i - t_0) = 0, \quad (2.14)$$

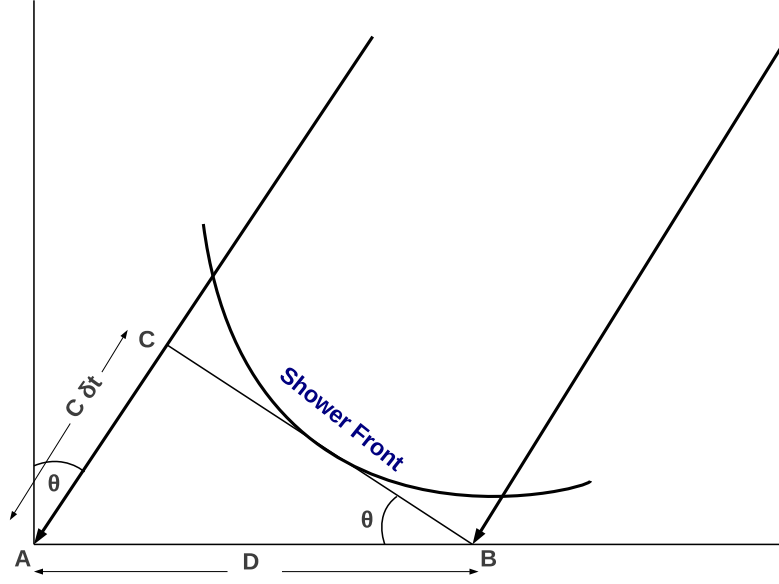


Figure 2.19: Two telescopes A and B are separated by a distance D . The shower arrives with an angle θ w.r.t zenith. The shower front arrives first at B, and after some delay of δt it arrives at A.

where position coordinates of the i th telescope are (x_i, y_i, z_i) , and t_0 is the time at which the shower front passes through the origin of the coordinate system. Now, we define

$$\chi^2 = \sum_{i=1}^7 w_i \left(lx_i + my_i + nz_i + c(t_i^{\text{measured}} - t_0) \right)^2, \quad (2.15)$$

where t_i^{measured} is the measured time of arrival of the shower front at the i th telescope and w_i is the statistical weight factor for the i th timing measurement and we consider constant weight factor for all measurements. Values of l , m , n , and t_0 are estimated by minimizing χ^2 w.r.t. l , m , n , and t_0 .

The direction cosines of an event is estimated from the timing information recorded in the array of telescopes as mentioned in the previous section. The arrival direction of the shower is obtained from these direction cosine estimates. Then the angle between pointing direction of the telescope and arrival direction of the shower is estimated. This angle is called “space angle”. Since cosmic rays are isotropic, with number of events within the

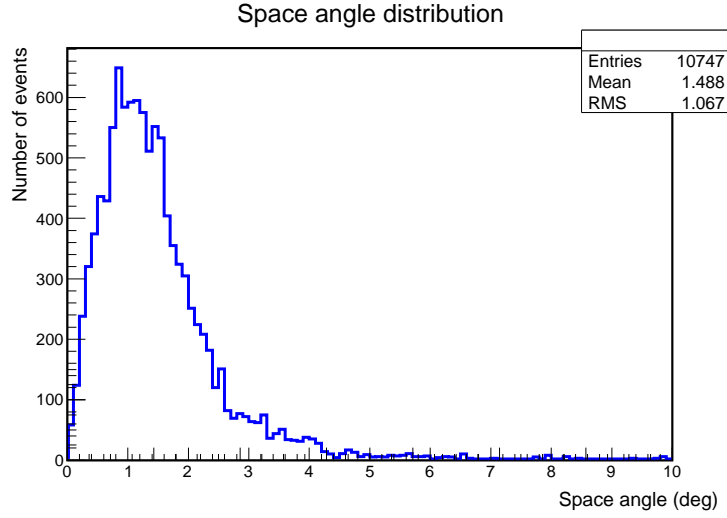


Figure 2.20: Space angle distribution of a typical ON-source run

opening angle (3°) of the telescope increasing as $\sin^2 \theta$ ($d\Omega \propto \sin^2 \theta d\theta$), the space angle distribution of cosmic ray events is expected to be broader than that for gamma-ray events. Space angle distribution for an ON-source run is shown in Figure 2.20.

Although Cherenkov shower front is spherical in shape, we approximate it by a plane front. Since extent of HAGAR array is just 100 m and radius of curvature of the shower front at Hanle is about 5000 m, plane front is a good approximation. However, it introduces some error in estimation of arrival angle of the shower, and this error increases with the core distance [46]. But this dependence of the error on core distance is smeared for the proton showers coming isotropically within the field of view of the telescope. As a result, error on reconstructed space angle does not show clear core distance dependence [46].

2.6.3 Signal extraction

Gamma-ray events are separated from the isotropic background of cosmic rays by comparing the space angle distributions of *ON-source* runs and *OFF-source* runs. By definition, the *ON-source* runs contain both gamma-ray and cosmic ray events, whereas *OFF-source* runs contain only cosmic ray events. If N_{ON} is the number of events present in an

ON-source run and N_{OFF} is the number of events present in an *OFF-source* run, then the number of gamma-ray events is obtained from the following relation:

$$Signal = N_{ON} - N_{OFF} \quad (2.16)$$

Since the *ON-source* runs and *OFF-source* runs are taken at two different times in the same night and the sky conditions are different for two different runs, we need to normalize N_{OFF} w.r.t. N_{ON} and the equation 2.16 can not be used in its present form. In order to normalize N_{OFF} w.r.t. N_{ON} several procedures can be adopted [89]. However, here we use the following procedure to do the normalization. We compare space angle distribution for a pair of *ON-source* and *OFF-source* runs. Since, the number of gamma-ray events at larger space angles are expected to be zero, we define the normalization constant (κ) to be the ratio of number of events within a space angle window around the tail of the space angle distribution for ON-source run to that for the OFF-source run. Thus we have a normalization constant κ for every ON-source, OFF-source run pair. There is no specific value at which the lower limit (LL) of the space angle window is to be chosen. We consider this at the tail of the distribution where FWHM of the space angle distribution intersects (see Figure 2.21), and the upper limit (UL) is set at 6.5° .

Once we find the normalization constant for a given ON-OFF pair, we can estimate the number of gamma-ray events using the following relation,

$$\text{Number of gamma-ray events} = \sum_{i=0}^{FWHM} (N_{ON}^i - \kappa N_{OFF}^i), \quad (2.17)$$

where, N_{ON}^i and N_{OFF}^i are number of events in i th bin of the space angle for ON- and OFF-source run, respectively, and κ is the the normalization constant for that pair.

At present, in analysis procedure, the gamma-hadron separation on event to event basis is not done. However, it can be done considering detail analysis of QDC data and FADC

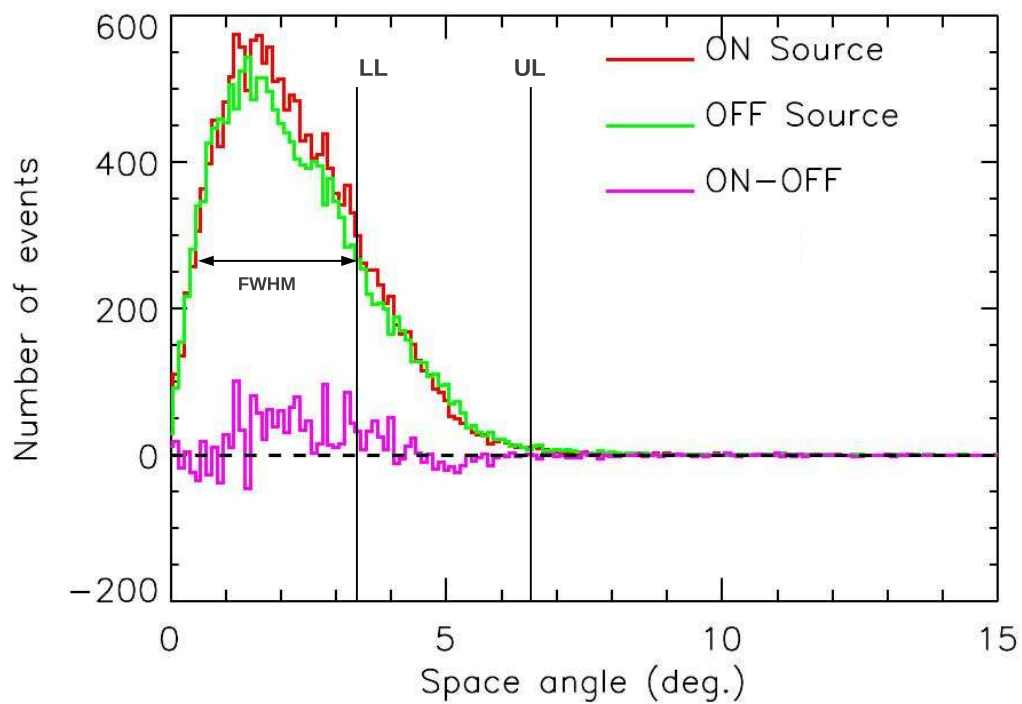


Figure 2.21: Space angle distributions of a source run (red) and a background run (green). The excess events at different space angles are also shown by histogram in magenta.

data based on Monte Carlo simulations which needs further study.

2.7 Summary

In this Chapter, we have discussed the basic theory of Cherenkov radiation and their detection by Cherenkov telescopes. Details of the HAGAR system including telescope control, data acquisition, and observation technique have been discussed. Finally, the procedure for estimation of gamma-ray signal from raw data pertaining to HAGAR system has been described.

Chapter 3

Monte Carlo Simulations for HAGAR

Simulations play a very important role in very high energy (VHE) gamma-ray experiment. Since VHE gamma rays cannot be produced in the laboratory, direct calibration of the instrument is not possible. So, we can only understand the performance of the instrument by estimating various performance parameters from simulations. In particular, the energy threshold of the telescope system can be determined only through simulations. We used the publicly available software package CORSIKA to simulate air showers induced by cosmic gamma-rays, protons and other nuclei. The detector simulation software for the HAGAR system has been developed in house. The details of the simulation [7] are described here.

3.1 Atmospheric air shower simulations

CORSIKA [5, 6] is a Monte Carlo program for studying the evolution of extensive air shower (EAS) in the atmosphere initiated by photons and various species of charged particles including protons, alpha particles and other nuclei. We use CORSIKA version 6.720 for atmospheric air shower simulations. The VENUS [90] code is used for high energy hadronic interactions and the GHEISHA [91] program is used for the low energy hadronic

interactions. For electromagnetic interactions EGS4 [92] program is used. We used our detector geometry in the input data card choosing the IACT [93] option in CORSIKA. We do not have measurements of the atmospheric profile at the Hanle site yet. So we have used the US standard atmospheric profile as best possible choice for the generation of Cherenkov photons. Wavelength dependent absorptions of Cherenkov photons caused by atmosphere, reflectivity of mirrors (average value of 80%) and quantum efficiency of PMT are given as input in CORSIKA.

Inputs to CORSIKA

We have used following inputs to the CORSIKA program, which are specific to the HAGAR system.

- **Type of the incident particle:** Gamma rays, protons, helium nuclei, and electrons.
- **Spectral index of the energy spectrum and the energy range**

Showers initiated by gamma rays, protons, alpha particles and electrons are simulated using the following spectral shapes [94, 95]:

$$\frac{dN_\gamma}{dE} = 3.27 \times 10^{-7} E_{TeV}^{-2.49} \text{ TeV}^{-1} \text{ m}^{-2} \text{ s}^{-1},$$

$$\frac{dN_p}{dE} = 8.73 \times 10^{-2} E_{TeV}^{-2.7} \text{ TeV}^{-1} \text{ m}^{-2} \text{ s}^{-1} \text{ sr}^{-1},$$

$$\frac{dN_\alpha}{dE} = 5.71 \times 10^{-2} E_{TeV}^{-2.6} \text{ TeV}^{-1} \text{ m}^{-2} \text{ s}^{-1} \text{ sr}^{-1},$$

$$\frac{dN_e}{dE} = 11.5 \times 10^{-5} E_{TeV}^{-3.08} \text{ TeV}^{-1} \text{ m}^{-2} \text{ s}^{-1} \text{ sr}^{-1},$$

respectively. The spectral index of the primary γ -rays (-2.49) is used in accordance with the energy spectrum of Crab nebula derived from Whipple data [57]. The spectral shape measured by Whipple is consistent with measurements from HEGRA [96] and MAGIC above 200 GeV [72]. The energies of primary particles

are selected using random numbers distributed according to the power law energy spectrum given above.

- **Angle of incidence of the primary particle (θ and ϕ):** For vertically incident showers the zenith angle (θ) is fixed to 0° . For inclined showers, both lower- and upper-limit of θ are changed accordingly. Azimuthal angles (ϕ) of the incident showers are selected uniformly in the range $0-360^\circ$.
- **Geomagnetic field at Hanle:** The geomagnetic field used is appropriate for the Hanle location with the horizontal and vertical components of the magnetic field being $B_x = 32.94\mu\text{T}$ and $B_z = 38.58\mu\text{T}$, respectively.
- **Altitude:** The altitude of Hanle is taken to be 4270 m.
- **Wavelength range:** Information about Cherenkov photons with wavelength in the range of 200 nm – 650 nm is stored.
- **Array size and co-ordinates of telescopes:** We have used the geometry of the HAGAR array as described in Chapter 2. An array of 7 telescopes is used, and six of them are kept at the corners of a hexagon and the 7th one is kept at the centre of the hexagon. The length of a side of the hexagon is 50 m.
- **Atmospheric attenuation:** The standard table for the atmospheric absorption given in the CORSIKA in the wavelength range of 180 – 700 nm is used. The table gives transmission coefficients of Cherenkov photons for various altitudes. In the case of Hanle altitude, the average transmission is about 90%.
- **Impact parameter and Viewing cone:** Impact parameter is varied over the range of 0 – 300 m. The viewcone option enables the generation of showers within the viewing cone of a Cherenkov telescope. The viewcone is kept at 0° around the pointing direction for gamma ray initiated showers and varied over $0^\circ - 4^\circ$ for cosmic ray generated showers. The azimuthal angle is selected over the range of $0^\circ - 360^\circ$.

Table 3.1: Samples generated for vertical showers.

Type	Energy range GeV	# of showers generated
Gamma rays	20-5000	1×10^6
Protons	50-5000	3×10^6
Alpha particles	100-10000	6×10^6
Electrons	20-5000	3×10^5

The number of showers generated using the above input parameters and energy ranges used in simulations are given in Table 3.1 for vertically incident showers. We have also simulated showers for inclination angles of 10° , 15° , 20° , 30° , 40° , and 45° .

3.1.1 CORSIKA output

The simulations give the positions of Cherenkov photons at the ground level along with their direction cosines. For vertical showers the telescopes are pointed towards the zenith. So the X-Y coordinates of photons on the mirror plane are the same as those at ground level. But for inclined showers we have calculated arrival times and locations of Cherenkov photons in the telescope plane (i.e. the plane perpendicular to the pointing direction) using appropriate transformations. The details of this coordinate transformation procedure for this kind of telescopes can be found in [46]. Finally, the CORSIKA simulations give the information about the number of Cherenkov photons falling on the mirrors, their arrival angle and arrival time.

3.2 Detector simulation

CORSIKA simulations give information about the arrival time of Cherenkov photons at each PMT. This information is then passed through the detector simulation program. This program takes into account details of the HAGAR system including PMTs, coaxial cables, trigger formation etc. In addition to Cherenkov photons, we must also take into account

the night sky background (NSB) photons. The NSB photons are simulated assuming a flux of $2 \times 10^8 \text{ ph cm}^{-2} \text{ s}^{-1} \text{ sr}^{-1}$ in the wavelength range of 200 – 650 nm, measured at Hanle using the single photo electron counting technique¹. The NSB levels at the different sites of the ground-based gamma-ray experiments are shown in Table 3.2. NSB photons are simulated in 0.2 ns bins using a Poissonian distribution around this measured value and following a typical wavelength dependence of the NSB given in [97]. For this purpose we have used a functional fit to the data given in [97] to obtain the normalized NSB distribution function, which has the following form:

$$\begin{aligned}
 f(\lambda) = & -161.92695 + 0.237421 \lambda - 0.0001422 \lambda^2 \\
 & + 4.46152 \times 10^{-08} \lambda^3 - 7.72914 \times 10^{-12} \lambda^4 \\
 & + 7.01583 \times 10^{-16} \lambda^5 - 2.60706 \times 10^{-20} \lambda^6.
 \end{aligned} \tag{3.1}$$

Table 3.2: The NSB fluxes at different sites of gamma-ray telescopes.

site	Experiment	Wavelength range (nm)	NSB flux ($10^8 \text{ ph/sr/m}^2/\text{s}$)	Reference
La Palma, Spain	MAGIC	300 – 650	2.60	[98]
Khomas, Namibia	HESS	300 – 650	2.12	[98]
Arizona, USA	VERITAS	300 – 500	2.50	[99]
Hanle, India	HAGAR	200 – 650	2.0	(Internal note by B. B. Singh)

Here λ is wavelength of the photons in units of Angstrom. The corresponding normalized NSB flux distribution is shown in Figure 3.1. The NSB photons are added to Cherenkov photons which are obtained from CORSIKA simulations. CORSIKA allows conversion of the Cherenkov photons into photo electrons according to the quantum efficiency curve for the PMT (see Figure 3.2). Similarly each NSB photon is converted into photo electron using the same quantum efficiency curve according to the wavelength assigned to the photon using equation (3.1). The PMT response function for a single photo electron measured in laboratory is approximated with a Gaussian with rise time of 3.0 ns and

¹NSB flux measured at Hanle varied between $(0.8 - 2) \times 10^8 \text{ ph cm}^{-2} \text{ s}^{-1} \text{ sr}^{-1}$ depending on the region of the sky as well as on the season.

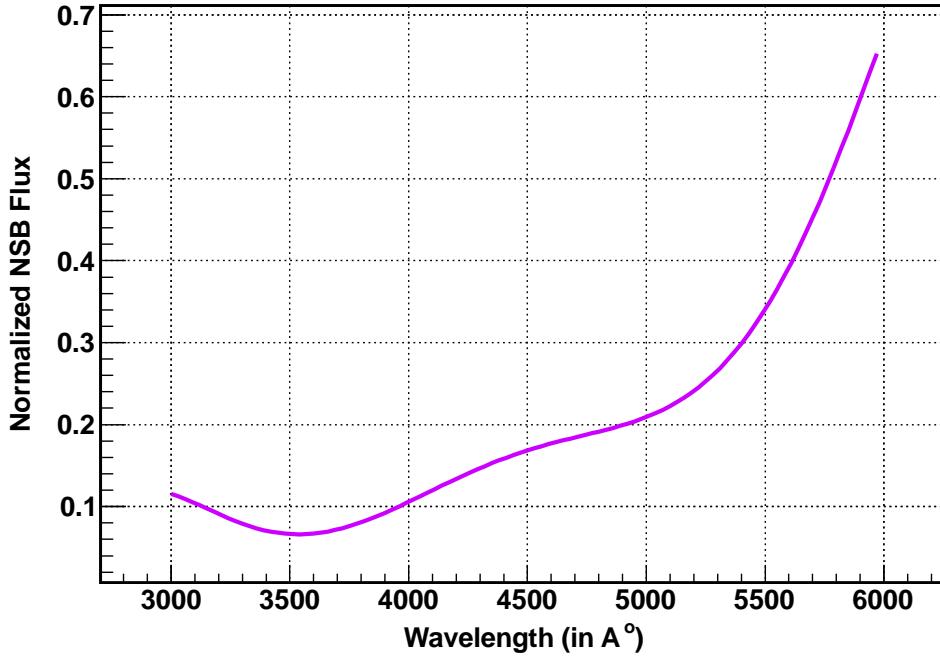


Figure 3.1: Normalized NSB flux distribution in the wavelength range of 3000 Å to 6000 Å.

FWHM ($= 2 \sqrt{2 \ln 2} \sigma$) of 4.2 ns as given by

$$f(t) = \frac{1}{\sigma \sqrt{2\pi}} \exp \frac{-(t - t_0)^2}{2\sigma^2}, \quad (3.2)$$

where $t_0 = 6.7$ ns.

The PMT pulses are generated by convolving the number of photoelectrons in each bin with the above PMT response function. The pulse shape profile is converted to voltage $v(t)$ using the relation, $v(t) = i R f(t)$, where, i is PMT current, R is load resistance of PMT and $f(t)$ is the pulse profile due to the single photo electron (equation 3.2). The PMT load resistance is kept at 50 ohms, and the PMT current, i , is calculated using the relation, $i = g/(e \times \text{FWHM})$, where e is the electron charge and g is the PMT gain. We use an average PMT gain of 6.78×10^5 . Attenuation of these pulses in coaxial cables (30 m of LMR-Ultraflex-400 and 55 m of RG213) is taken into consideration using frequency dependence of attenuation provided by manufacturer. A trigger is generated when at least

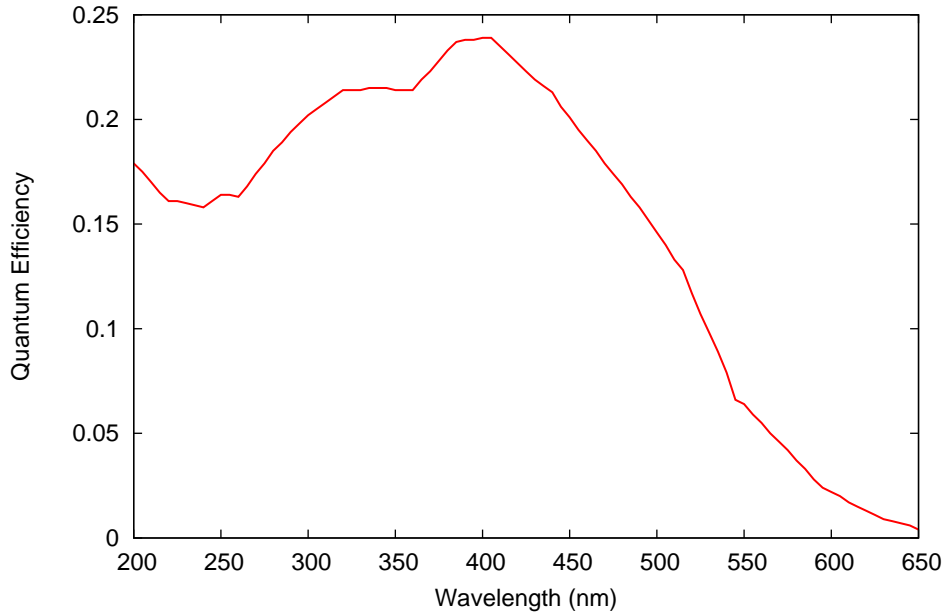


Figure 3.2: Quantum efficiency plot for PMT (XP2268B).

4 RS pulses out of 7 cross the discriminator threshold of 220 mV in a coincidence window of 150 ns for showers within zenith angles of 30° . For larger zenith angles a coincidence window of 300 ns is used. This is dictated by the largest arrival time differences for the telescope array. In terms of photo electrons this discriminator threshold corresponds to 17.5 photo electrons per telescope. Once a trigger is generated, TDC and QDC values are calculated using various calibrations carried out with the HAGAR setup. These values are written to the output file.

3.3 Performance parameters

3.3.1 Trigger rate

A HAGAR trigger is generated when at least 4 telescope pulses out of 7 cross a discriminator threshold within a narrow coincidence window. Performance parameters are estimated for this condition (≥ 4) as well as for other trigger conditions involving at least

Table 3.3: Performance parameter for HAGAR telescope array for vertical shower.

Trigger condition	Proton trigger rate (Hz)	Alpha trigger rate (Hz)	Electron trigger rate (Hz)	Gamma Ray rate (/min)	γ -ray Energy Threshold (GeV)	Effective Area for γ -rays (m^2)	Observed Trigger rate (Hz)
≥ 4	9.2	3.7	0.11	6.3	208	3.2×10^4	13.4 ± 0.2
≥ 5	4.5	2.7	0.05	3.9	234	2.4×10^4	8.5 ± 0.1
≥ 6	2.2	1.6	0.03	2.4	263	1.7×10^4	4.9 ± 0.1
$= 7$	1.1	0.9	0.01	1.5	275	1.2×10^4	2.4 ± 0.1

Table 3.4: Performance parameters for various zenith angles for the ≥ 4 trigger condition.

Zenith angle ($^\circ$)	Proton trigger rate (Hz)	Alpha trigger rate (Hz)	Gamma Ray rate (/min)	γ -ray Energy Threshold (GeV)	Effective Area for γ -rays (m^2)	Observed Trigger rate (Hz)
0	9.2	3.7	6.3	208	3.2×10^4	13.4 ± 0.2
15	9.1	3.7	6.4	234	3.4×10^4	12.9 ± 0.5
30	8.9	2.9	5.0	316	4.4×10^4	11.7 ± 1.0
45	6.8	2.7	3.8	549	7.8×10^4	10.1 ± 1.6

5 telescopes (≥ 5), at least 6 telescopes (≥ 6) and all 7 telescopes ($=7$) triggering. Performance parameters for various trigger conditions for vertically incident showers are given in Table 3.3 and those for various zenith angles are given in Table 3.4 (for ≥ 4 trigger condition only).

The cosmic ray trigger rate estimated from simulations, assuming that the bulk of the triggers come from protons, alpha particles and electrons, is 13 Hz for ≥ 4 trigger condition. This matches very well with the observed trigger rate from HAGAR for near-vertical showers. The expected gamma-ray rate for a Crab like source at near-vertical position is 6.3 counts/minute. The trigger rate decreases for higher-fold trigger conditions as seen from Table 3.3. It also decreases for higher zenith angles as seen from Table 3.4.

3.3.2 Energy threshold

The energy threshold of HAGAR is obtained from the differential rate plot (Figure 3.3 and Figure 3.4). The energy corresponding to the peak of the differential rate curve is conventionally quoted as energy threshold. Differential rate curves for various trigger conditions and for different zenith angles are shown in Figure 3.3 and Figure 3.4 respectively. Values of the energy threshold so obtained for various conditions and zenith angles are listed in Tables 3.3 and 3.4. In the case of vertically incident gamma rays, the energy threshold is about 208 GeV for ≥ 4 trigger condition and increases at most restrictive trigger conditions. This is because, in order to trigger larger number of telescopes, the Cherenkov photon density must be higher, which requires higher-energy showers. Also, as we go to higher zenith angles, the showers need to travel through larger atmospheric mass. Hence, atmospheric attenuation becomes more effective for higher zenith angle. Moreover, the Cherenkov light pool is distributed over larger area, thereby reducing the number of Cherenkov photons per unit area. As a result, higher energy showers are required to trigger the system. The energy threshold for ≥ 4 trigger condition increases from 208 GeV near vertical to 549 GeV for zenith angle of 45° .

In addition to the energy threshold for gamma-ray showers, we have also estimated the energy threshold for proton showers. It is about 435 GeV for ≥ 4 trigger condition, which is about twice the gamma-ray energy threshold. This indicates that the peak of the differential rate curve for proton showers will be shifted towards the right of the corresponding curve for gamma-ray showers in Figure 3.3.

We have performed simulations to study the dependence of the trigger rate on the discriminator threshold keeping the NSB flux level fixed. The discriminator threshold defines the photo-electron threshold and hence the energy threshold. If we reduce the discriminator threshold the trigger rate will increase. Reducing the discriminator threshold results in acceptance of lower-energy gamma-ray events. However, in reality, using lower discriminator thresholds will make the system susceptible to accepting chance events. So we

Table 3.5: Variation of trigger rate and energy threshold with discriminator bias.

Discriminator Threshold (mV)	Photo-electron Threshold	Trigger Rate (Hz)	γ -ray Energy Threshold (GeV)
170	13.5	62.0	138
180	14.3	36.2	151
190	15.1	20.4	169
200	15.8	16.0	181
210	16.7	13.3	199
220	17.5	13.0	208
230	18.3	11.2	218
240	19.0	9.2	230

always operate our system at 220 mV (i.e. 17.5 photo-electrons) threshold which gives a chance rate well within a few percent of the trigger rate.

Figure 3.5 shows the variation of trigger rate with energy threshold (hence photo electron threshold). These results are given in Table 3.3.2 along with thresholds in terms of number of photo electrons.

Since we encounter different levels of background brightness for different sources, the variation of the trigger rate with the NSB photon flux was also studied. The NSB was varied in the range $(1.0 - 2.5) \times 10^8 \text{ ph cm}^{-2} \text{ s}^{-1} \text{ sr}^{-1}$ in steps of $0.5 \times 10^8 \text{ ph cm}^{-2} \text{ s}^{-1} \text{ sr}^{-1}$ and PMT gains are changed accordingly to get individual PMT rates of 5 KHz as done in experiment. The royal sum discriminator thresholds are also changed to get royal sum rates within 25–35KHz. Then the corresponding trigger rates and γ -ray energy thresholds are estimated and are shown in Table 3.6. The energy threshold decreases as we go from a brighter region to a darker one. The reason for this is explained in the following: the individual PMT rate increases with the NSB. As a result, the royal sum rates also increase and this gives higher trigger rates leading to higher chance events as already mentioned above. Hence, we decrease the gain of each PMT such that individual PMT rates are brought to about 5 KHz. As a result, low energy showers become inefficient to trigger the system, and trigger rate decreases as shown in Table 3.6.

Table 3.6: Variation of trigger rate and energy threshold with NSB flux level.

NSB ($\times 10^8$ $\text{cm}^{-2}\text{s}^{-1}\text{sr}^{-1}$)	Trigger Rate (Hz)	γ -ray Energy Threshold (GeV)
1.0	20.7	158
1.5	15.8	177
2.0	13.0	208
2.5	9.3	251

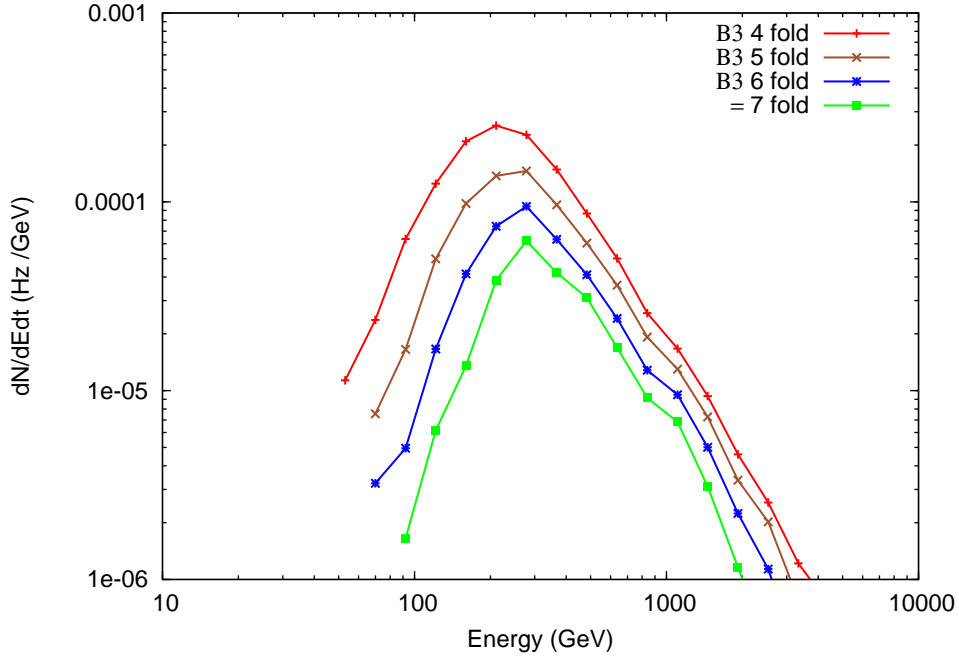


Figure 3.3: Differential rate plots for different trigger conditions for simulated gamma-ray showers.

A setup similar to the HAGAR but at lower altitudes is PACT(Pachmarhi Array of Cherenkov Telescopes)[2, 46, 100] in INDIA. It is installed at Pachmarhi, on the hills of Satpura mountain range, in the state of Madhya Pradesh (Central India). The altitude of PACT is 1075m amsl. The energy threshold for this PACT array was estimated to be 700 – 800 GeV, about a factor of 4 higher than that achieved by the HAGAR.

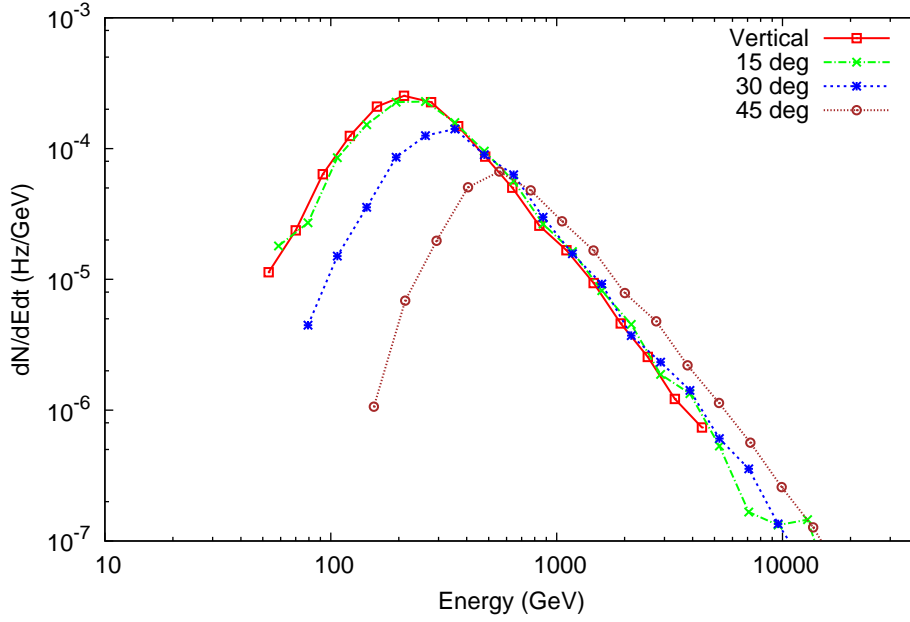


Figure 3.4: Differential rate plots for different zenith angles for the ≥ 4 trigger condition.

3.3.3 Effective area

We have estimated the “effective collection area” for various trigger conditions. This area is an energy-dependent quantity which depends on the details of detector elements and trigger conditions for the detector. The effective area is defined as

$$A_{eff}(E) = \int_0^{r_{max}} \epsilon(r, E) 2\pi r dr, \quad (3.3)$$

where ϵ is the fraction of showers which trigger the system, r_{max} is the maximum impact parameter and E is the energy of the incident primary particle. The value of r_{max} is taken to be 300 m above which $\epsilon(r, E) \equiv 0$. Figure 3.6 shows the variation of the effective area with energy for vertically incident γ -ray, proton and alpha particle showers, for the trigger condition ≥ 4 . The average value of the effective area for ≥ 4 trigger condition is 3.2×10^4 m², which decreases for higher-fold trigger condition (see Table 3.3). The effective area also increases with zenith angle (see Table 3.4).

We have simulated γ -ray showers using γ -ray spectral indices in the range 2.0 – 3.0. The

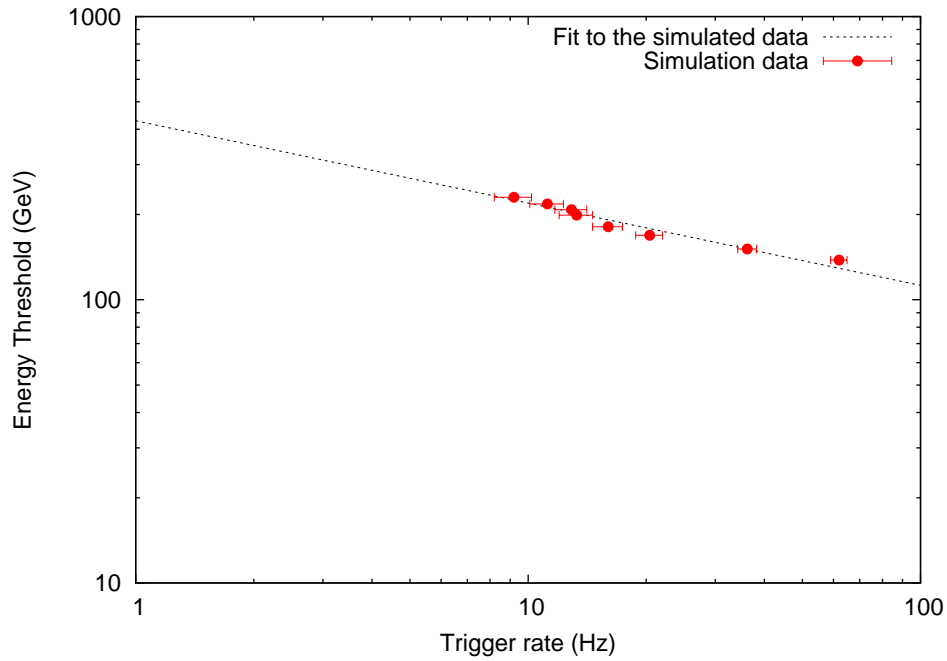


Figure 3.5: Energy threshold vs trigger rate from simulations.

energy threshold as well as the average effective area of the system decrease with the increase of spectral index; see Table 3.7.

3.3.4 Detection efficiency

The detection efficiency of γ -rays depends on their energy range as well as the impact parameter. It increases with the energy of the primary particles. For example, with the \geq

Table 3.7: Dependence of the energy threshold and effective collection area on the spectral shapes of the γ -ray energy spectrum.

Spectral index	γ -ray Energy Threshold (GeV)	Effective area for γ -rays (m^2)
2.0	223	3.6×10^4
2.2	223	3.5×10^4
2.4	213	3.3×10^4
2.49	208	3.2×10^4
2.6	199	3.0×10^4
2.8	190	2.7×10^4
3.0	173	2.3×10^4

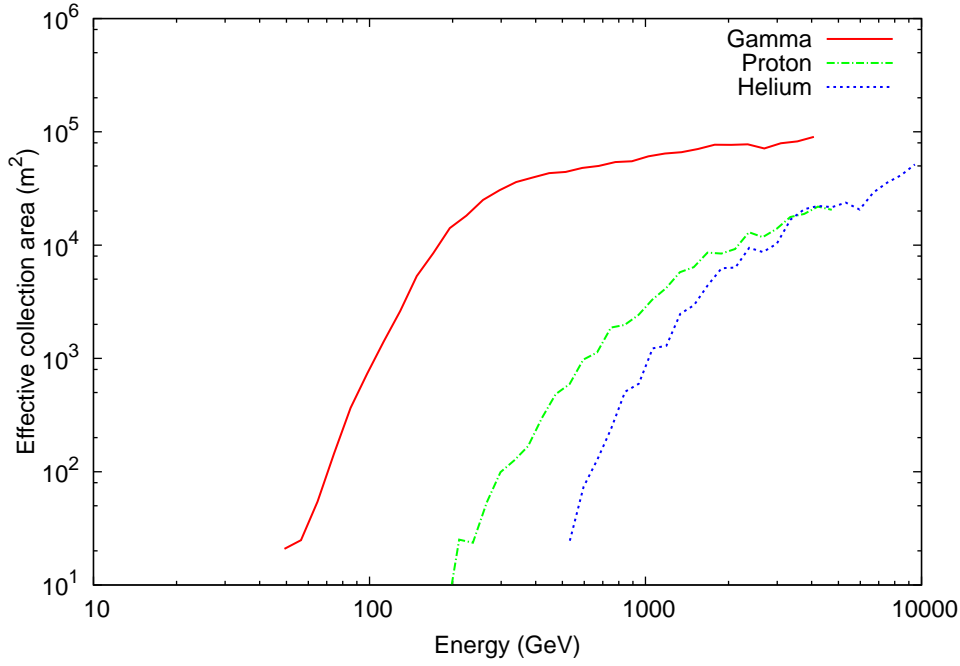


Figure 3.6: Effective collection area vs energy of primary from simulations for vertical incidence for ≥ 4 trigger condition.

4 trigger condition, for γ -ray energy $E \geq 20$ GeV, 0.5% of the simulated showers trigger the system. But, 5.4% and 25.2% of showers trigger the system for $E \geq 100$ GeV and $E \geq 1$ TeV, respectively. The detection efficiency decreases with the impact parameter. For impact parameter $R \geq 0$ m, 0.5% of the gammas trigger the system and it is only 0.12% for $R \geq 100$ m and 0.01% for $R \geq 150$ m. Proton showers are simulated keeping viewcone, θ , in the range of $0^\circ - 4^\circ$. The detection efficiency for proton showers also decreases with θ . For $\theta \geq 0^\circ$, 0.02% of showers trigger the system. But for $\theta \geq 2.5^\circ$, this becomes 0.003%. These numbers are subject to the parameter ranges (in energy, impact parameter, viewcone) considered here. Figures 3.7, 3.8 and 3.9 show how the detection efficiency changes with the change of primary energy, impact parameter and viewcone, respectively.

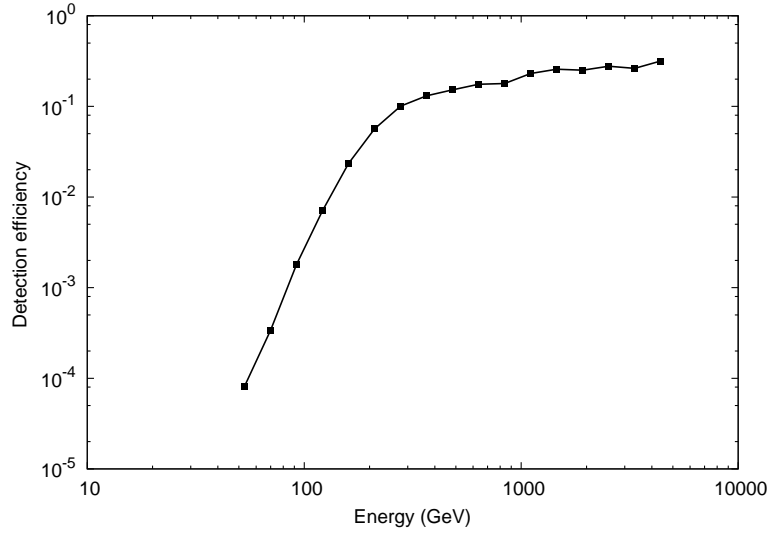


Figure 3.7: Detection efficiency vs energy for γ -rays from simulations for the ≥ 4 fold trigger condition.

3.3.5 Sensitivity

The gamma-ray flux sensitivity of an ACT system is defined as the lowest gamma-ray flux that can be detected over the isotropic cosmic ray background at a predefined level of significance ($n\sigma$) which can be expressed as

$$n\sigma = \frac{N_{ON} - N_{OFF}}{\sqrt{N_{ON} + N_{OFF}}}, \quad (3.4)$$

with N_{ON} = number of showers from the source direction which includes γ -ray showers from the source as well as cosmic ray showers from the source direction and N_{OFF} = number of background showers (which are essentially cosmic ray showers) away from the source direction.

Since, $N_{ON} = R_\gamma t + (R_p + R_\alpha) t$ and $N_{OFF} = (R_p + R_\alpha) t$, the equation 3.4 can be written as

$$n\sigma = \frac{R_\gamma \sqrt{t}}{\sqrt{R_\gamma + 2(R_p + R_\alpha)}}, \quad (3.5)$$

where R_γ , R_p and R_α are trigger rates of photons, protons and alpha particles, respectively, and t is the observation duration. We can increase the sensitivity of our measurement by

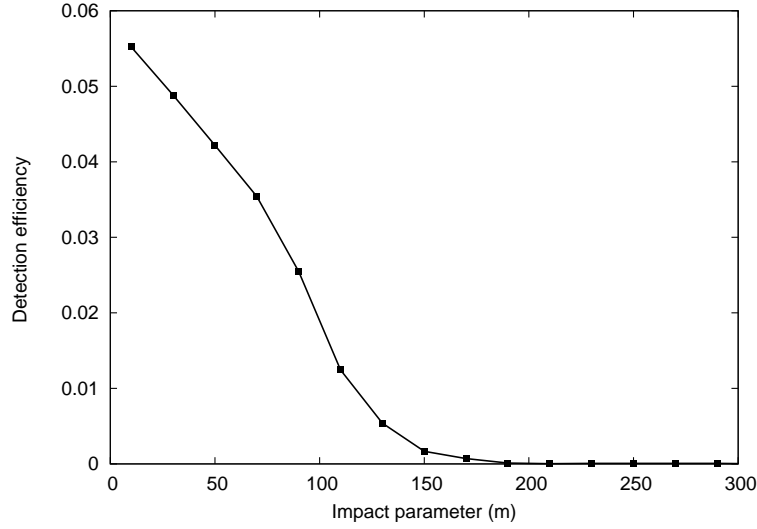


Figure 3.8: Detection efficiency vs impact parameter for γ -rays from simulations for the ≥ 4 fold trigger condition.

increasing the observation duration of the source. For different sources, R_γ , which is related to the flux from the source, will be different. As a result $n\sigma$ also depends on the flux of the observed source. So using different flux level we can plot the time duration (t) required to get a given value of the significance, $n\sigma$. Figure 3.10 shows the observation duration needed for HAGAR to detect a source at 5σ (i.e. $n = 5$) significance level as a function of the source flux in units of the Crab flux. This implies that HAGAR will be able to detect a source like the Crab nebula at a significance level of 5σ in 17 hours of observation duration, assuming no additional criteria for the rejection of background cosmic ray events. This corresponds to the HAGAR significance for the Crab Nebula of $1.2\sigma \times \sqrt{\frac{T}{\text{hour}}}$, where T is the duration of observation. The sensitivity could be improved if more cosmic ray background events are rejected by imposing additional criteria².

²Some amount of cosmic rays gets rejected at the trigger level due to the choice of 4-fold or higher fold trigger.

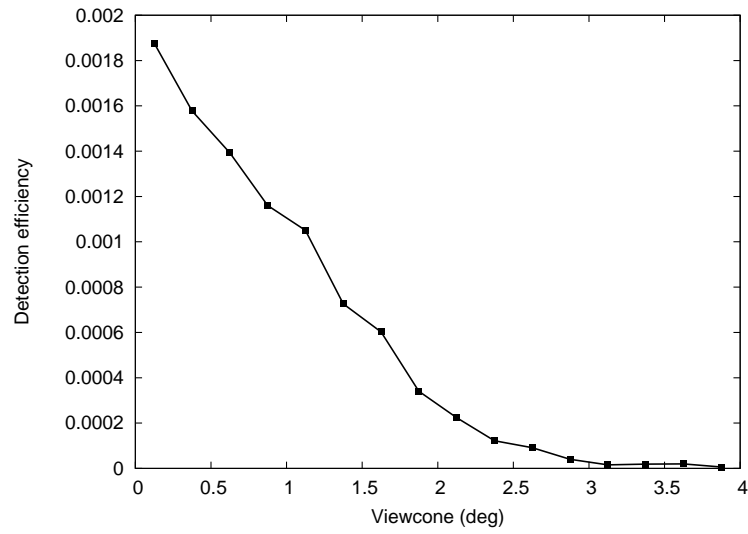


Figure 3.9: Detection efficiency vs viewcone for proton showers from simulations for the ≥ 4 fold trigger condition.

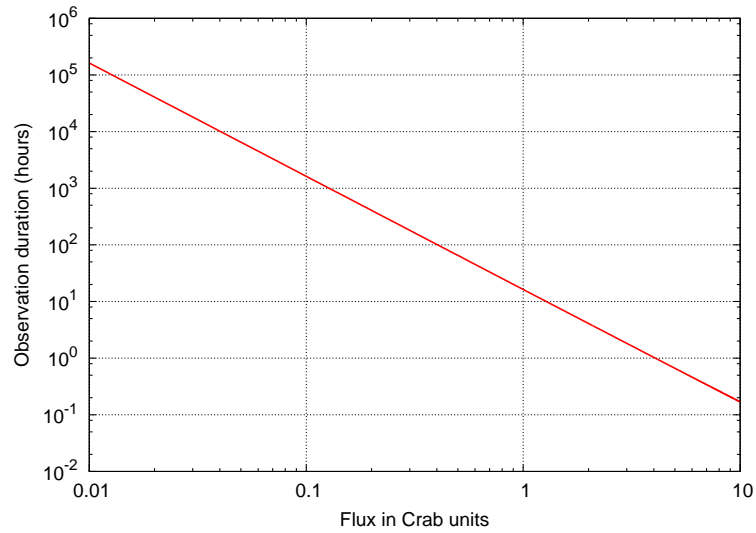


Figure 3.10: Observation duration vs source flux for detection of a source at 5σ significance level with HAGAR with no additional criteria for the rejection of cosmic ray events.

3.4 Comparison of observational data with Monte Carlo simulations

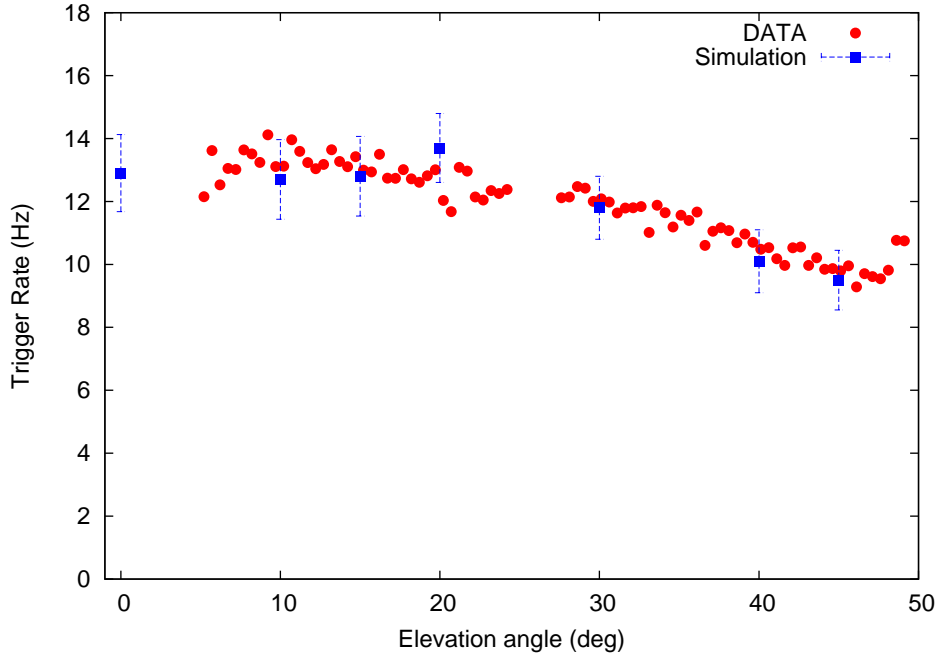


Figure 3.11: Comparison of the data with simulations for trigger rates at different elevation angles.

- **Trigger rate**

As mentioned earlier, the estimate of the cosmic ray trigger rate from our simulations matches well with the observed rate near vertical. For vertical showers the trigger rate obtained from simulations is about 13 Hz which is consistent with the observed trigger rate of about 13.4 Hz. We have also compared the variation of the observed and simulated trigger rates for different zenith angles. For this purpose, data obtained by tracking dark region of the sky passing through zenith was used. Figure 3.11 shows the comparison of the observed trigger rate as a function of zenith angle with the simulated rates for various zenith angles. A good agreement between the two is seen.

- **Trigger ratio**

Table 3.8: Telescope Trigger Ratio, R_N , for simulated data, $R_{N,s}$, and for observed data, $R_{N,o}$ with N, the number of telescopes.

N	Simulated Trigger Ratio $R_{N,s}$	Observed Trigger Ratio $R_{N,o}$
4	6.4	5.6
5	3.6	3.5
6	1.9	2.0

Another check on the performance of the telescope system is provided by the “Telescope Trigger Ratio (TTR)”, which we define as follows:

$$R_N \equiv \frac{\text{Number of showers triggering } \geq N \text{ telescopes}}{\text{Number of showers triggering all 7 telescopes}} \quad (3.6)$$

Table 3.8 shows the comparison between simulation and observed data for R_N , indicating a good agreement between the two except the tail region of the space angle distribution.

- **Space angle distribution**

Finally, Figure 3.12 shows the comparison of the space angle distributions obtained from simulations and observed data for vertical showers for various trigger conditions. For each triggering event, the direction of the shower axis is reconstructed from the TDC data using the plane front approximation for the Cherenkov wavefront. The space angle is defined as the angle between the pointing direction of the telescope system (position of the source in the sky) and the reconstructed shower direction. Details about the analysis of data using the space angle distribution are described in Chapter 2. There is a fair agreement between the two distributions. We have also compared the space angle distributions between cosmic-ray (proton and helium) showers and γ -ray showers, both obtained from simulations, as shown in Figure 3.13. The distributions of space angle for cosmic-ray showers are somewhat broader than the γ -ray showers as expected because of isotropic nature of cosmic-rays.

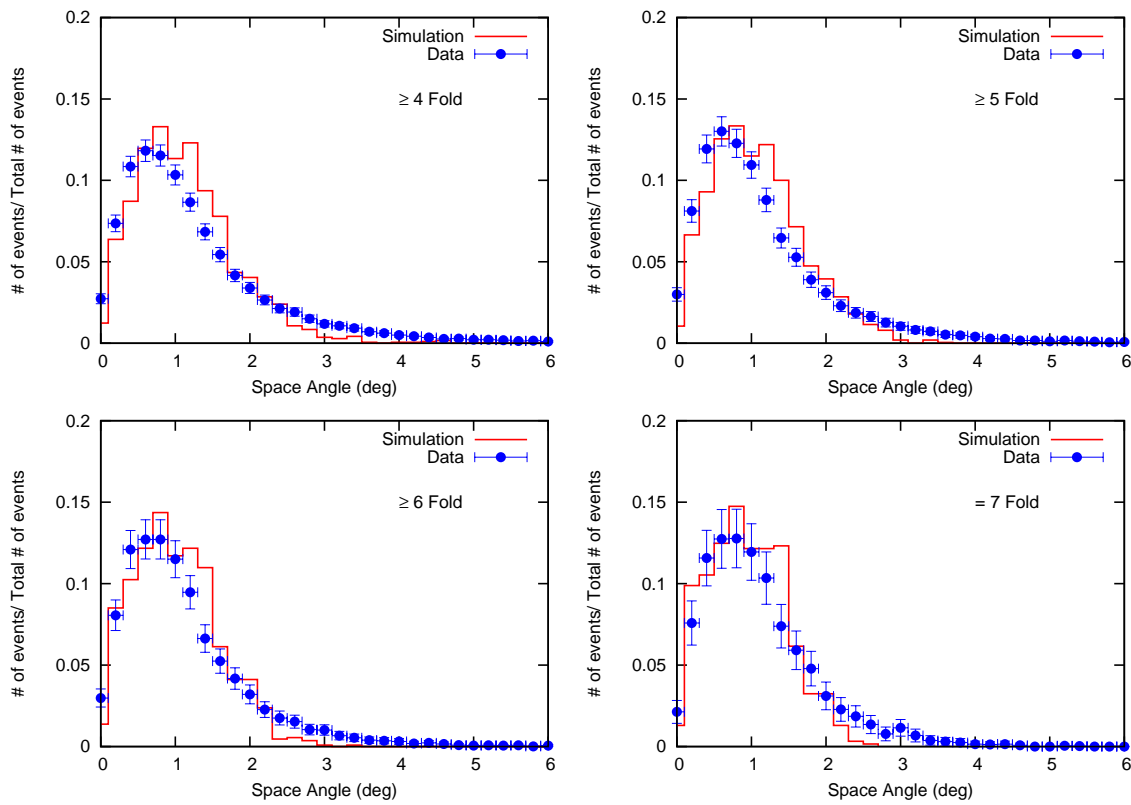


Figure 3.12: Comparison of space angle distributions from simulations with observed data, both for vertical directions.

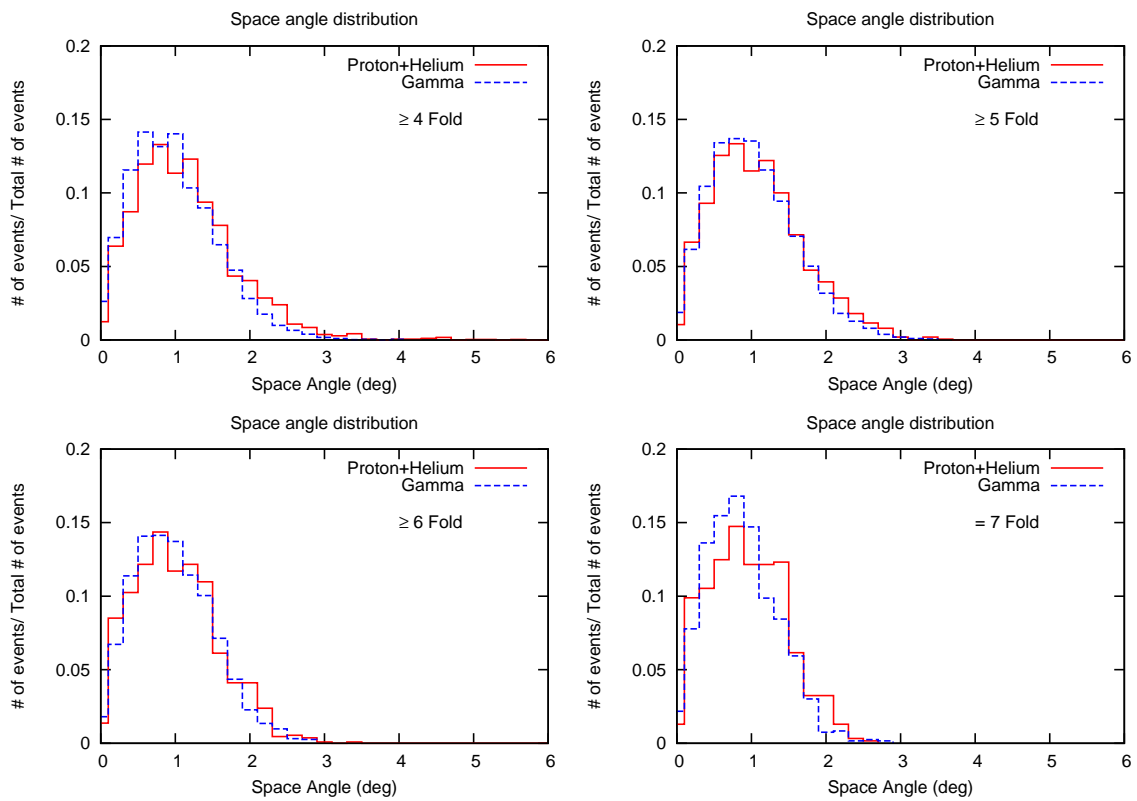


Figure 3.13: Comparison of space angle distributions from simulated cosmic ray (proton and helium) and γ -ray showers, both for vertical directions.

3.5 Summary

Monte carlo studies show that energy threshold of HAGAR is about 210 GeV, about a factor of 4 lower than that achieved by PACT. Thus, by installing the HAGAR system at high altitude, it was possible to bring down the energy threshold by a factor of 4 without significantly increasing the mirror area. We have also estimated that this telescope system will be able to detect Crab-like sources in 17 hours of observations with the significance of 5σ without further rejecting cosmic ray events. Comparison between the space angle distributions and variation of trigger rates with zenith angle obtained from simulations are in good agreement with the observed data, indicating that the HAGAR telescope system is well understood and accurately modelled.

Chapter 4

TeV Gamma-ray sources

The HAGAR array saw its first light in September, 2008, and since then it is successfully taking data on several Galactic and extra-galactic sources. The estimation of the sensitivity of the experiment is performed using several hours of data from the direction of the Crab nebula, the standard candle of TeV gamma-ray emitting sources. Data were acquired using the ON-source/OFF-source tracking mode as described in Chapter 2. By comparing the space angle distribution of an ON and OFF pair, the strength of the gamma-ray signal is estimated. Monte Carlo simulations yield an estimation of the HAGAR energy threshold to be around 210 GeV for vertically incident showers considering a Crab-like gamma-ray spectrum. Apart from the Crab nebula, several other sources are also observed with the HAGAR telescope system. The observation log for all the sources observed so far is shown in Table 4.1. The total observation time during the period of September 2008 to September 2013 is about 2700 hours, including both ON and OFF source observations. This gives us an estimate of about 540 hours per year of observation at HAGAR site. For the first two years we did not have observation runs for about three months during winter due to lack of manpower at site, whereas for the last three years observation runs were taken throughout the year. Figure 4.1 shows the total observation time available and the used time during the period of October 2012 to September 2013. The total available time

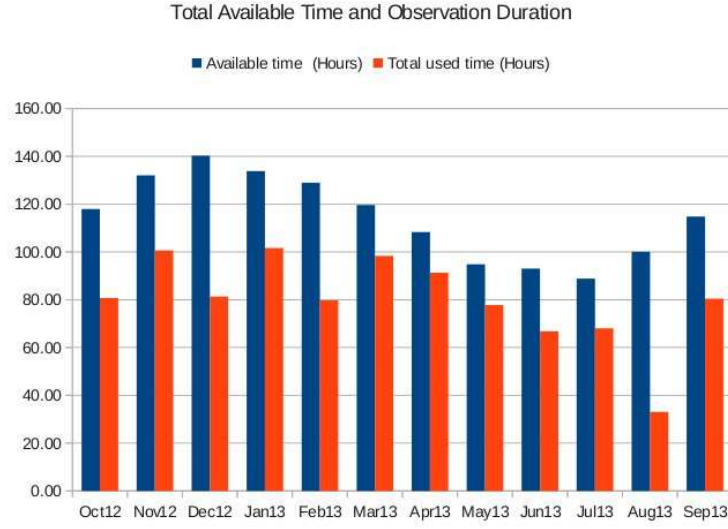


Figure 4.1: Observation period during October 2012 to September 2013.

and used time during this period were about 1372 and 950 hours, respectively, and the used time (~ 950 hours) is comparable to the observation times (~ 1000 hours) for the sites of MAGIC and VERITAS telescope systems.

In this Chapter, we will discuss our results for the observations of three Galactic sources: the Crab nebula, LSI 61+303 and MGRO J2019+37.

Table 4.1: Observation log from September, 2008 to September, 2013 (Run number 1 to 3690)

Source	ON (Hrs)	OFF (Hrs)	Remarks
Galactic Sources :			
LSI+61 303	44.95	47.73	Detected (this thesis)
Crab	202.39	189.3	Detected [101]
Geminga	126.3	76.07	Not detected [102]
Fermi Pulsar J0358+3208	20.56	9.47	Not detected [102]
Fermi Pulsar J0633+0632	34.49	11.53	Not detected [102]
Fermi Pulsar J1846+0919	35.84	12.51	Data not analysed yet
Fermi Pulsar J2055+25	45.01	20.64	Not detected [102]
MGRO J2019+37	30.21	29.47	No definite detection (this thesis)
PSR 0007+73	43.75	16.28	Data not analysed yet
Extra Galactic Source :			
Markarian 421	196.09	227.07	Detected [89]
M87	2	2.69	Insufficient data
Markarian 501	121.5	127.12	Analysed and Submitted
1ES1218+304	47.74	56.15	Data not analysed yet
1ES1959+650	6.91	9.46	Insufficient data
BL Lac 2203+4220	40.31	40.34	Data not analysed yet
1ES2344+514	114.04	131.03	Partially analysed
3C454.3	15.29	15.32	Insufficient data
S5 0716+714	8.92	8.95	Insufficient data
H 1426+428	22.25	23.32	Insufficient data
CALIBRATION RUNS:			
3rd magnitude Star	35.69	36.05	—
delta Leo	10	9.35	—
Dark region	153.8	—	—
Fix Angle	199.63	—	—
Vertical	49.1	—	—
Milky Way	17.5	—	—

4.1 Data selection

Depending upon atmospheric conditions, electronic noise, discontinuity in data recording during an observation run, the data may contain some fluctuations in the event rate. As a result, some systematic errors might be present in the final result. Therefore, for estimating gamma-ray fluxes, it is necessary to check the health of the raw data before using them for more detailed analysis. In order to reduce systematics, some parameters which characterize good quality data, are considered in our analysis. One of such parameters is the fluctuation in the event rate. We check whether the event rate of the run is stable within the normal statistical fluctuation during the observation. If it is stable throughout the observation period (~ 40 minutes or ~ 80 minutes) of a run then we consider it as a good quality run. The left panel of Figure 4.2 shows an example of event rates during a 40 minute run. We reject those runs for which individual event rates fluctuate randomly from the mean value beyond what is expected from statistical fluctuations. An example of such a run is shown in the right panel of Figure 4.2. We have also noticed that the event rates in a data file fluctuate during a small period of time, or some spike could be present due to some electronic noise or sudden appearance of clouds in the sky. In this situation, we do not reject the whole run, rather we just consider that portion of the run where the event rate is stable. In our data analysis procedure the stability of the event rate of each run is quantified using one variable, which is called R_{stab} , that is defined as the ratio of the RMS of the rate to the square root of its mean,

$$R_{stab} = \sqrt{\left(\frac{\sum_{i=0}^{nbins} (R_{10}(i) \times 10 - R_{mean} \times 10)^2}{nbins \times R_{mean} \times 10} \right)}, \quad (4.1)$$

where, $nbins$ is the number of bins in a 40 minutes or 80 minutes run with a bin size of 10 seconds, $R_{10}(i)$ is the total event rates in the i th bin and R_{mean} is the average event rate

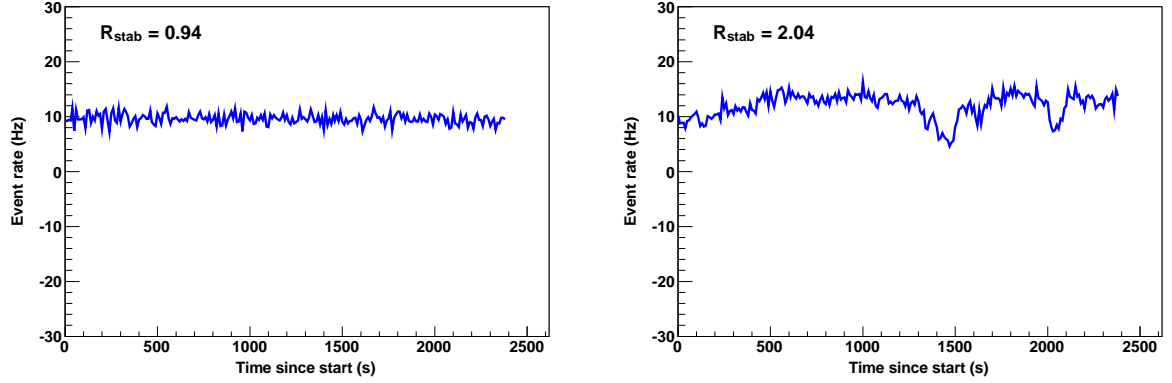


Figure 4.2: *Left:* event rates of a good quality run. *Right:* event rates of a bad quality run

in the run. The rates are measured in units of Hz. For perfect Poissonian fluctuations, this variable is expected to be equal to 1. Figure 4.3 shows the distribution of R_{stab} values for 50 runs. If the R_{stab} of a specific run is greater than 1.2, as indicated in Fig. 4.3 with a vertical line, then we reject this run.

Our next step is to select a good ON and OFF pair. An ON/OFF pair is always selected from the observation runs taken in the same night. The sky brightness will be different for an ON-source and an OFF-source run due to presence of stars in the field of view and as they are taken at two different times in the same night. As a result, trigger rate will be different for two different observations. In order to ensure that there is no significant differences in the trigger rates between an ON and an OFF run, the difference between the mean trigger rates of an ON and an OFF run is restricted to be less than 2 Hz. Since events in both ON and OFF runs are dominated by cosmic rays (as mentioned in section 2.6.3), the difference should be nearly equal to 0. However, the sky brightness during observation of an ON-OFF pair changes which leads to different energy thresholds for the ON and OFF runs, thereby giving rise to different trigger rates. Hence, by imposing this above criterion we control dramatic changes in the atmospheric condition and data acquisition within a pair. Some additional selection criteria can be found in Refs. [101, 46].

After selection of good quality ON and OFF pairs, some of the pairs are rejected based on different criteria as mentioned in Ref [46]. For some of the ON runs, it is found

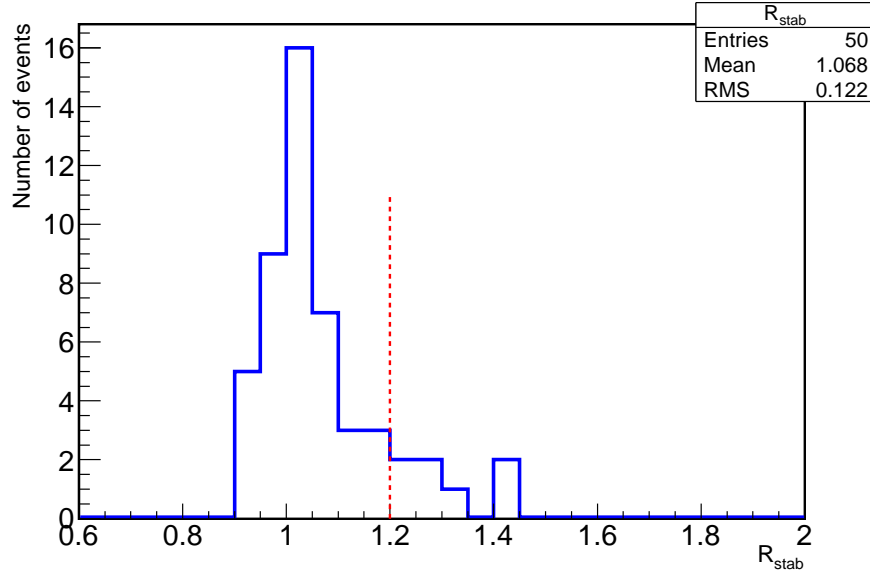


Figure 4.3: Distribution of R_{stab} of 50 runs with a vertical line which separates good and bad quality runs.

that the peak positions of the space angle distributions are shifted with respect to the corresponding OFF runs. Another rejection criterion is imposed based on the value of normalization constant for an ON-OFF pair. Runs with normalization constants roughly within 0.6 to 1.2 were accepted depending on the source. Since both the ON and OFF runs consists of triggers corresponding to cosmic rays, the normalization constant should be close to 1. Any large deviation of the normalization constant from 1 indicates either an excess or deficit in the gamma-ray events.

4.2 Crab Nebula

The Crab Nebula is a remarkably well studied Galactic object in almost all the accessible electromagnetic wavebands. It is the relic of a core-collapse supernova explosion that occurred in 1054 AD at a distance of $d \sim 2$ kpc [103]. The right ascension (RA) and declination (dec) of the Crab nebula for the epoch J2000 are $5^h 34^m 31^s.97$ and $22^\circ 00' 52''.1$, respectively. This young supernova remnant, with an age of 950 years, is pow-

ered by the Crab pulsar with a rotational period of 33 ms and a spin-down luminosity of $L = 5 \times 10^{38} \text{erg s}^{-1}$. The Crab nebula is believed to be an ideal acceleration site for relativistic electrons. The rotational energy of the Crab pulsar is carried away by a wind of relativistic electrons and positrons, and the interaction of this wind with the surrounding medium gives rise to a standing termination shock [54, 104]. These accelerated electrons produce synchrotron photons while interacting with the nebular magnetic fields. Furthermore, interaction of the relativistic electrons with the synchrotron photons in the nebula produces high energy gamma rays through inverse Compton and bremsstrahlung processes. Thus the Crab nebula is observed in radio to VHE gamma rays. The VHE gamma-ray signal from the Crab nebula was first detected with high statistical significance by the Whipple telescope in 1989 [41].

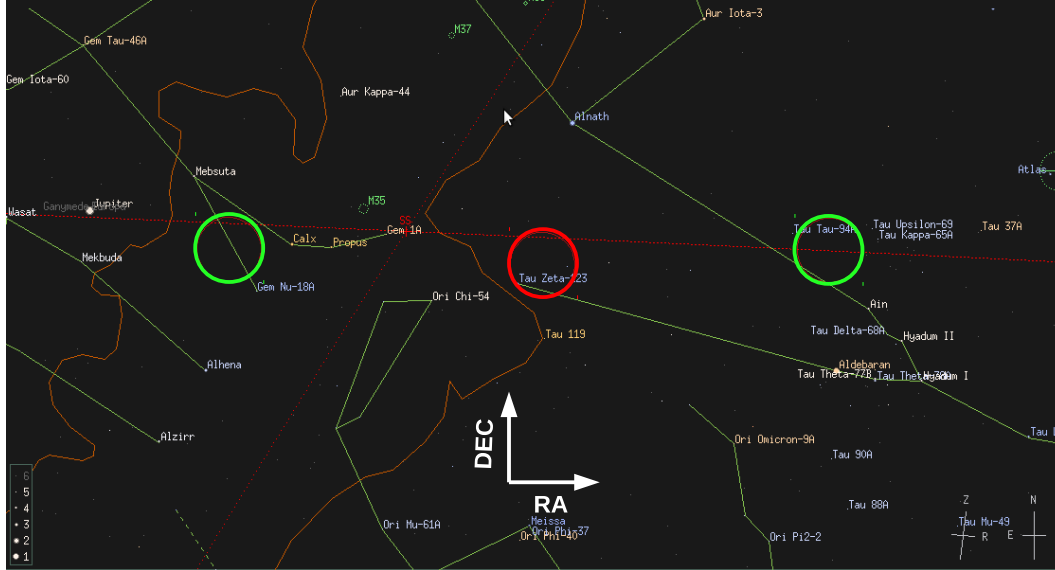


Figure 4.4: Location of the Crab nebula (red circle with radius 3 degrees; ON-source region) in the sky along with the two background regions (green circles with radius 3 degrees; OFF-source regions).

4.2.1 Analysis and results

HAGAR has observed the Crab nebula over the period from 2008 to 2013. However, in this thesis, the gamma-ray signal from this source is estimated based on data taken during the period of 2010 and 2011. In order to measure the relative propagation delays or the time Offsets in the transmission of signals from PMTs/Telescopes to the various TDC channels in the control room due to unequal cable lengths, pulse widths etc., a fixed angle run is considered in this analysis (see section 2.5.1). We mostly use 10 degree south (10S) fixed angle runs for analysis of data in each season, provided those runs are present in that season. If not, then vertical runs from that season or the 10S runs from the consecutive seasons are used. Additionally, for all the runs analysed here, all 7 telescopes were operational during the observation period, and the corresponding hour angle of the runs were within -15° and $+15^\circ$. Checks on the data quality were routinely carried out, and only good quality data (with $R_{stab} < 1.2$) were taken for this analysis. After imposing different analysis cuts as mentioned in section 4.1, we had 23 good ON-OFF pairs that corresponds to 14.3 hours of data. These selected pairs for final analysis are shown in Table 4.2. All the OFF runs mentioned in Table 4.2 are 40-minutes runs, whereas some of the ON runs like 1388, 1405 are 80-minutes runs. First 40 minutes of these runs are used to make pairs with runs 1387 and 1404, respectively, and remaining 40 minutes of these ON runs are used to make pair with 1389 and 1406, respectively. In all these cases, RA of an OFF run is chosen in such a way that it covers the same zenith angle range as that of the paired ON-source run. Figure 4.4 indicates the location of the Crab nebula in the sky with a red circle with size 3 degrees which corresponds to ON-source run and the locations of two background regions (green circles) which correspond to OFF-source observations. The distribution of gamma-ray rates estimated for all the pairs are shown in the upper panel of Figure 4.5, and the light curve of the Crab nebula for different telescope trigger conditions are shown in the lower panel of Figure 4.5. In two of the pairs, much higher gamma-ray rates are seen. In principle, this may indicate the variability of the

source. However, it should be noted that we have not considered systematic errors in our analysis. These errors are to be added in quadrature with statistical errors, and this may increase error bars significantly, thereby diluting the significance in these runs. Hence, based on these data we cannot attribute the higher gamma-ray rates to variable nature of the source. In order to estimate systematic error we need to take many more runs tracking dark regions. At present our data sample for these runs are not sufficient to estimate systematic error.

The estimated gamma-ray rates for different triggering criteria are given in Table 4.3 and Table 4.4. The analyses results show that the HAGAR has detected the Crab nebula with a significance of 13σ at the energy threshold of about 208 GeV for number of triggered telescopes (NTT) ≥ 4 . The corresponding average flux is $(5.6 \pm 0.4) \times 10^{-10}$ photons $\text{cm}^{-2} \text{s}^{-1}$. The estimated gamma-ray rate for NTT ≥ 4 is higher than the value estimated from Monte Carlo simulations as shown in Chapter 3 (see Table 3.3). However, the gamma-ray rates for NTT greater than or equal to 5-fold, 6-fold and 7-fold are consistent with simulated results. The possible reason for this inconsistency for NTT greater than 4-fold is discussed below.

Table 4.2: Selected pairs for the Crab nebula analysis.

Year	Months	Run No. of Pairs	Number of pairs	duration (minutes)
2010	October-November	1262/1261; 1267/1268; 1277/1278; 1287/1288; 1296/1297; 1298/1299;	6	236
	November-December	1373/1372; 1388/1387; 1388/1389; 1405/1404; 1405/1406	5	198
2011	January-February	1562/1561; 1566/1565; 1568/1567; 1622/1621;	4	155
	September-October	2062/2061; 2082/2081; 2088/2087; 2097/2096;	4	115
	October-November	2184/2185	1	40
	November-December	2204/2205; 2222/2223; 2245/2246;	3	115

There is a bright star of magnitude 3 located at $67.5'$ from the Crab nebula. As a result, the

estimated signal could be biased by the light of the star. The presence of a bright star in the field of view (FOV) of the Crab nebula contributes to the star light and hence to the night sky background light. Higher NSB means more NSB triggers for same discriminator bias. This leads to different threshold energy for ON and OFF runs. ON runs will have lower energy threshold than that of OFF runs and this leads to fictitious signal counts even if the source is not emitting gamma rays. Monte Carlo simulations also establish the fact that the gamma-ray energy threshold increases with the increase in NSB (see Table 3.6). In order to reduce the effect of higher NSB or effect of a bright star, higher coincidence logic such as NTT greater than or equal to 5, 6, etc. has to be considered. To estimate the fictitious signal counts due to presence of the star, some observations were performed keeping this bright star (or a star of similar magnitude and colour) in the FOV of HAGAR, but with the Crab nebula outside the FOV. Then comparing ON/OFF differences, the fictitious signals were estimated [101, 105], and the artificial signal was obtained for $\text{NTT} \geq 4$ -fold. These studies [101, 105] indicates that the systematic effects induced by the bright star in the FOV is higher for lower telescope triggering threshold, and it can be reduced by keeping higher coincidence logic, that is, different trigger conditions. By taking higher telescope trigger threshold such as 5-fold and above, the systematics in the signal could be reduced. The requirement of a coincidence of larger number of telescopes in an event, like NTT greater than or equal to 5, 6, etc., increases the energy threshold but significantly rejects the events due to fluctuations in NSB.

Analysis of 2 years' data of the Crab nebula shows that the estimated flux is consistent with the observed fluxes by other experiments for NTT greater than 5 fold. The fluxes measured by different other experiments and HAGAR (for NTT greater than 5-fold) from the Crab nebula are shown in Figure 4.6. The estimated gamma-ray rate matches well with the simulated gamma-ray rates (see Table 3.3) for NTT greater than or equal to 5-fold and above. The estimated gamma-ray rate for NTT greater than 4-fold is higher than the simulated value, and the possible reason for this is the systematic effect induced by the light from the 3 magnitude star in the FOV of the Crab nebula.

Table 4.3: Results of the Crab nebula for NTT equal to 4-fold, 5-fold, 6-fold and 7-fold.

fold	pairs	Excess	Error Excess	Duration (min)	Gamma rate (/min)	Significance (σ)
=4	23	4481.1	406.8	860.5	5.20 ± 0.47	11.0
=5	23	1226.3	347.0	860.5	1.92 ± 0.40	3.5
=6	23	1646.6	309.0	860.5	1.91 ± 0.35	5.3
=7	23	1549.9	294.7	860.5	1.80 ± 0.34	5.2

Table 4.4: Results of the Crab nebula for NTT \geq 4-fold, 5-fold, 6-fold and 7-fold

fold	pairs	Excess	Error Excess	Duration (min)	Gamma rate (/min)	Significance (σ)
≥ 4	23	8904.0	684.3	860.5	10.83 ± 0.79	13.0
≥ 5	23	4422.9	550.3	860.5	5.63 ± 0.63	8.0
≥ 6	23	3196.6	427.0	860.5	3.71 ± 0.49	7.4
=7	23	1549.9	294.7	860.5	1.80 ± 0.34	5.2

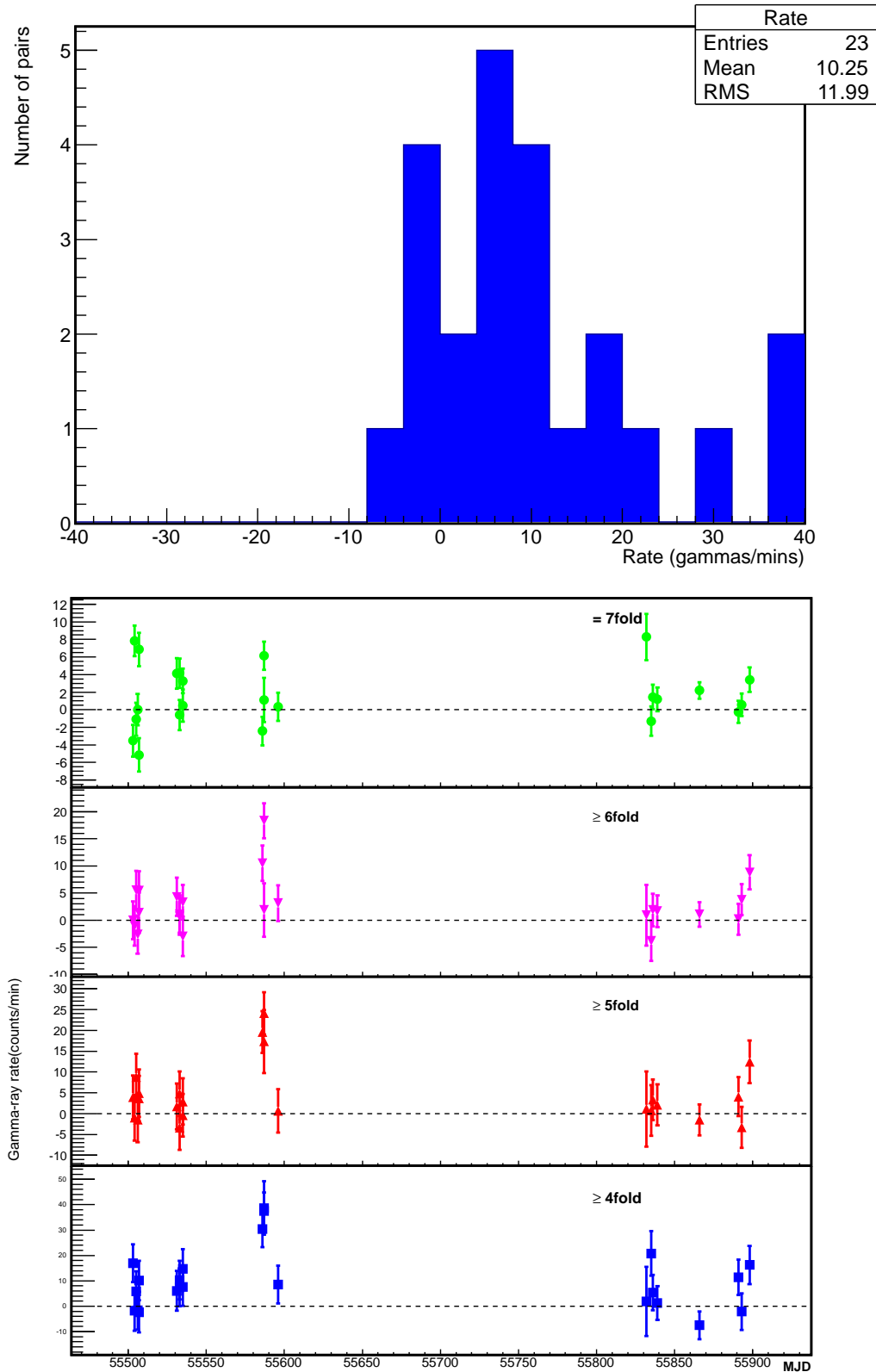


Figure 4.5: *Upper*: Distribution of gamma-ray rates for 23 pairs of the Crab nebula data for $\text{NTT} \geq 4$. *Lower*: Gamma-ray light curve of the Crab nebula for all 23 pairs for different telescope triggering conditions.

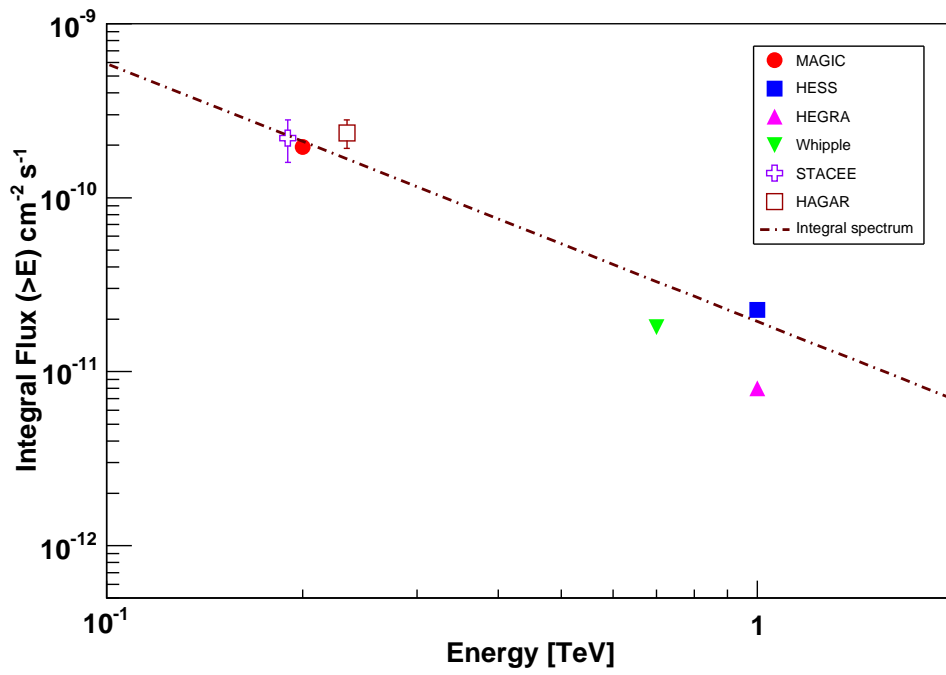


Figure 4.6: The integral flux of the Crab nebula from HAGAR along with HESS [72], MAGIC [71], Whipple [57], STACEE [106] and HEGRA [107] experiments. The flux estimated here is for NTT greater than 5-fold.

4.3 LSI 61+303

LSI 61+303 is a Galactic high-mass X-ray binary star system located at a distance of 2 kpc. The RA (J2000) and dec (J2000) of the source are $2^h 40^m 31^s.7$ and $61^\circ 23' 46''$, respectively. It was first detected as a TeV source by the MAGIC collaboration in 2005 [59]. This TeV gamma-ray source emits also in radio and x-ray wavelengths, and exhibits strong variable emission from the radio to X-rays. It is a B0 main-sequence star with a circumstellar disk which is of a Be star. The orbital cycle of the companion star is about 26.49 days. The mass of the compact source is still debated. LSI 61+303 is identified as a potential microquasar by detection of structures in radio observations, with high energy emission produced in jets driven by accretion onto the compact object. Microquasars are a type of binary stars. The central star is considered to be a neutron star or a black hole. The companion star losses its mass to the central one, and there is a relativistic outflow of jets from the vicinity of the central one. They emit high energy jets in the interstellar medium is comprising of high energy charge particles which produce high energy gamma rays.

LSI 61+303 has been observed in multiple wavelengths from radio all the way up to very high-energy gamma rays. The most recent radial velocity measurements show that the orbit of the compact companion is elliptical ($e = 0.537 \pm 0.034$), with the periastron passage determined to occur around phase $\phi = 0.275$, and the apastron passage at $\phi = 0.775$ [108] as shown in Figure 4.7. LSI +61 303 was observed by the MAGIC telescope system between October 2005 and March 2006. The maximum flux was detected at 8.7σ significance on MJD 53797 in the orbital phase of 0.67, and the corresponding flux was about 16% of the Crab nebula flux [59]. The first VERITAS observation of this source was made between 2006 September and 2007 February. The highest fluxes at different orbital cycles are measured between orbital phases 0.6 and 0.8, which corresponds to 10%–20% of the flux of the Crab nebula [109]. However, the results obtained by the VERITAS group based on observations made from 2008 October until 2010 December (MJD 54760.3 –

MJD 55506.2) are different from the results obtained earlier [59, 109]. No significant detection was made during 2008-2009 in any of the orbital phases previously detected by MAGIC and VERITAS. However, the source showed the maximum observed flux on 2010 October 8 (MJD 55477, $\phi = 0.07$; close to superior conjunction at phase 0.081) with 5.2σ significance [110], and the corresponding flux was approximately 7% of the Crab nebula flux. It was again observed between 2009 October and 2010 January [111] by the MAGIC telescope system. The source was detected with 6.3σ significance in the orbital phase interval of 0.6–0.7, and the estimated flux was 10 times lower than previously measured in this phase interval. Furthermore, VERITAS observations [112] during 2011 December (MJD 55911) – 2012 February (MJD 55947) suggested that the source was highly active in the orbital phases of 0.5–0.8, and the corresponding flux was 5% – 15% of the Crab nebula flux. These observations suggest that the emission from this source is variable in nature.

4.3.1 Analysis and results

Data taken during the period of 2010 to 2012 by HAGAR telescope system is used in our analysis. These observations covered six separate 26.5 day orbital cycles. Total 44.95 hours of ON-source data and 47.73 hours of OFF-source data were taken, which constitute 57 ON-OFF pairs. For all the runs analysed here, all 7 telescopes were operational during the observation period, and the corresponding hour angle of the runs were within -15° and $+15^\circ$. Preliminary checks and other analysis cut together rejected 23 pairs. The remaining 34 pairs corresponding to about 22 hours' data were finally used in this analysis. Details of these selected pairs are shown in Table 4.5. In this case, runs with run number 1244, 1251, 1357, 1363, 1370, 2139, and 2181 are 80 minutes ON-source observations. First 40 minutes of these runs are used to make pairs with 1243, 1250, 1358, 1364, 1369, 2138, and 2180, respectively and the remaining 40 minutes are used to make pairs with 1245, 1252, 1359, 1365, 1371, 2140, and 2182, respectively. For each pair the OFF run is taken over

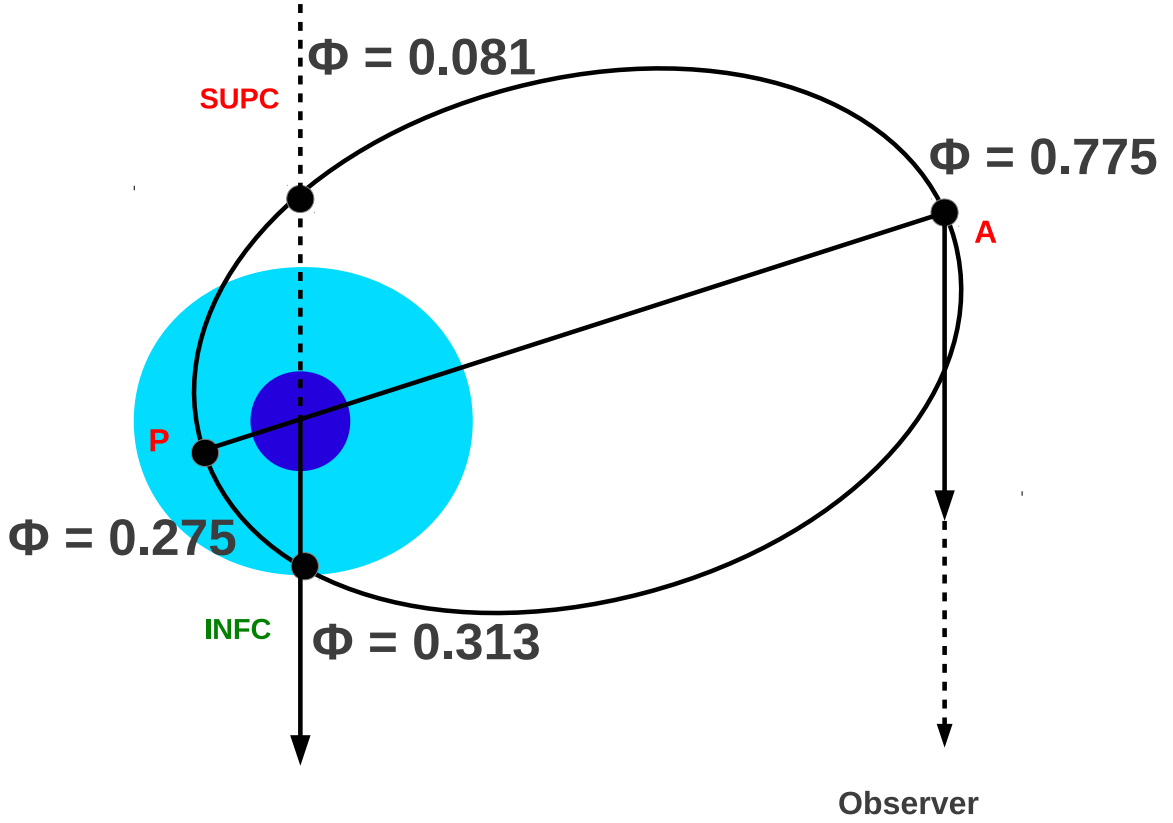


Figure 4.7: Orbital geometry of LSI 61+303. The phases for Inferior conjunction (INFC), Superior conjunction (SUPC), periastron (P), and apastron (A) are shown following Ref. [108] and they occur at orbital phases 0.313, 0.081, 0.275 and 0.775, respectively.

the same zenith angle range as that of ON-source run. Figure 4.8 indicates the location of the LSI 61+303 in the sky (red circle with size 3 degrees) corresponding to ON-source run and the locations of two background regions (green circles) which correspond to OFF-source observations. We have considered only those ON-OFF pairs for which the source was near transit, that is, the hour angle is in between -15° to $+15^\circ$ during observations, and all the 7 telescopes were participating in trigger formation. To measure the time offsets in each TDC channels, 10 degree and 20 degree north fixed angle runs are used in this analysis. Observation time, duration and corresponding orbital phases for all the ON-source runs and ON-OFF pairs are shown in Table 4.6 and Table 4.7, respectively.

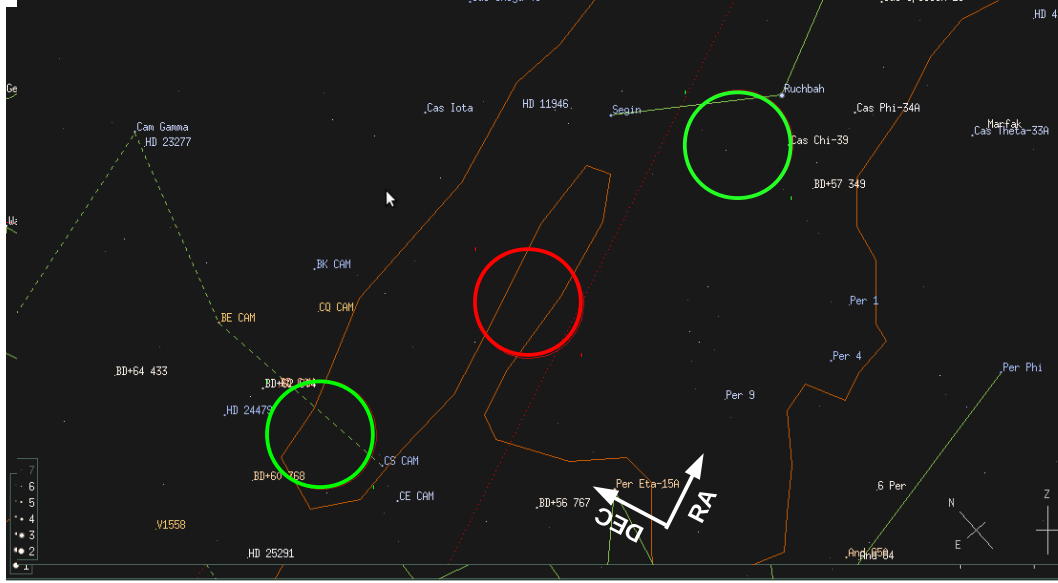


Figure 4.8: Location of LSI 61+303 (red circle with radius 3 degrees; ON-source region) in the sky along with the two background regions (green circles with radius 3 degrees; OFF-source regions).

The orbital phase is computed with the orbital period of 26.496 days and zero phase at JD 2443366.775. The total exposure times of each orbital phase are shown in Figure 4.9. The orbital phases 0.0–0.1 and 0.7–0.8 are observed for longer periods of time, whereas there were no observations for orbital phases 0.3 to 0.5. The distribution of gamma-ray fluxes and the light curve of LSI 61+303 are shown in upper and lower panels of Figure 4.10, respectively. The estimated gamma-ray rates for different telescope trigger conditions are given in Table 4.8 and Table 4.9. HAGAR detected LSI +61 303 with a significance of 7σ at the energy threshold of about 300 GeV for $\text{NTT} \geq 4$ -fold. The corresponding time average flux over all the orbital phase is $(1.84 \pm 0.25) \times 10^{-10} \text{ cm}^{-2} \text{ s}^{-1}$. This observed flux is about 56% of the Crab nebula flux, which is much higher than that of the fluxes estimated by VERITAS and MAGIC telescope systems. In addition to the flux estimate, it is important to see how the fluxes change over each orbital cycles. Since HAGAR data

is not enough statistically significant for each orbital cycles, we have taken the average of all the six orbital cycles to estimate the gamma-ray rate at different orbital phases. Figure 4.11 shows the gamma-ray rates at different orbital phases for different trigger conditions. Among the orbital phases, phases 0.0–0.1 and 0.8–0.9 show positive detection for NTT greater than or equal to 4-fold and above. The negative rates are seen in phase bin 0.6 – 0.7, and this result is based only on two pairs. So, we need to increase statistics in this phase bin.

Our analysis results show that the source was bright in the orbital phases of 0.0–0.1 and 0.7–0.8, and the estimated average flux over all the orbital phases during the period 2010 October to 2012 February was about 56% of the Crab nebula flux. The estimated fluxes by the VERITAS and the MAGIC are about 5-15% of the Crab nebula flux, and their observation periods do not exactly overlap with the HAGAR observation period. In our data analysis, we have used 20N and 10N fixed angle runs to estimate the time offsets as mentioned above. Since the source position is at about 30 degrees north from the zenith at Hanle during transit, we need 30N fixed-angle run to estimate accurately the time offsets. However, we do not have any 30N fixed-angle runs, and we have seen that t_0 's have slightly directional dependence. Therefore, this could be possible reason for estimating higher fluxes from this source. Moreover, LSI 61+303 showed variability in the gamma-ray fluxes at different orbital cycles. Therefore, we cannot rule out this possibility for observing higher fluxes from this source with the HAGAR telescope system.

The observations made with the MAGIC, VERITAS and HAGAR telescope systems suggest that the fluxes of this source at different orbital phases vary from orbit-to-orbit and year-to-year. Several models have been proposed to explain the observed fluxes at different orbital phases and their variability over the time. Some of these models are based on hadronic mechanisms. According to these models the relativistic protons in the jet interact with the ions of non-relativistic stellar wind, producing high energy gamma rays via neutral pion decay process [113, 114]. Others are based on leptonic mechanisms which

take into account the interaction of the relativistic jet particles with the magnetic field and all the photon and matter fields. For instance, high energy gamma rays can be produced via IC scattering of the relativistic electrons in the jet with the synchrotron photons of massive stellar companion and/or via relativistic bremsstrahlung where electrons in the jet interact with the ions of non-relativistic stellar wind [115, 116, 117].

Table 4.5: Selected pairs for the LSI 61+303 analysis.

Year	Months	Run No. of Pairs	Number of pairs	duration (minutes)
2010	October-November	1244/1243; 1244/1245; 1251/1250; 1251/1252; 1259/1258; 1264/1263; 1274/1273; 1284/1283; 1295/1294	9	358
	November-December	1357/1358; 1357/1359; 1363/1364; 1363/1365; 1370/1369; 1370/1371; 1377/1376; 1386/1385; 1396/1395	9	357
2011	October-November	2139/2138; 2139/2140; 2170/2169; 2176/2175; 2181/2180; 2181/2182; 2186/2187;	7	254
	November-December	2210/2211; 2220/2221;	2	79
2012	Dec2011-January	2260/2559; 2265/2264; 2284/2283; 2294/2293; 2304/2303;	5	189
	January-February	2355/2356; 2361/2362;	2	80

Table 4.6: Observation time, orbital phase, and duration for all ON-source runs for the observations of LSI 61 +303, horizontal lines separate different orbital cycles. MJD and orbital phase for each run are calculated considering the middle of each run.

MJD	ON runs	Duration (mins)	Phase
55501.027	1244	80	0.9852 ± 0.001
55502.066	1251	78	0.0244 ± 0.001
55503.020	1259	40	0.0604 ± 0.0005
55504.985	1264	39	0.1346 ± 0.0005
55505.982	1274	40	0.1722 ± 0.0005
55506.986	1284	40	0.2101 ± 0.0005
55507.021	1295	40	0.2114 ± 0.0005
55529.930	1357	80	0.0760 ± 0.001
55530.937	1363	78	0.1140 ± 0.001
55531.937	1370	78	0.1518 ± 0.001
55532.937	1377	40	0.1895 ± 0.0005
55533.937	1386	40	0.2273 ± 0.0005
55534.937	1396	39	0.2650 ± 0.0005
55860.007	2139	80	0.5337 ± 0.001
55864.992	2170	40	0.7218 ± 0.0005
55865.001	2176	33	0.7221 ± 0.0005
55866.021	2181	80	0.7606 ± 0.001
55867.011	2186	39	0.7980 ± 0.0005
55892.917	2210	40	0.7757 ± 0.0005
55893.950	2220	39	0.8147 ± 0.0005
55913.866	2260	40	0.5664 ± 0.0005
55915.843	2265	40	0.6410 ± 0.0005
55917.852	2284	29	0.7168 ± 0.0005
55918.849	2294	39	0.7544 ± 0.0005
55920.852	2304	40	0.8300 ± 0.0005
55943.813	2355	40	0.6966 ± 0.0005
55944.808	2361	40	0.7342 ± 0.0005

Table 4.7: Orbital phase and corresponding exposure time for all the pairs for LSI 61+303.

Run No. of Pairs	durations (mins)	orbital phase	Run No. of Pairs	durations (mins)	orbital phase
1244/1243	40	0.9852	1396/1395	39	0.2650
1244/1245	40	0.9862	2139/2138	40	0.5337
1251/1250	39	0.0244	2139/2140	19	0.5347
1251/1252	39	0.0254	2170/2169	40	0.7218
1259/1258	40	0.0604	2176/2175	33	0.7221
1264/1263	39	0.1346	2181/2180	40	0.7606
1274/1273	40	0.1722	2181/2182	41	0.7616
1284/1283	40	0.2101	2186/2187	39	0.7980
1295/1294	40	0.2114	2210/2211	40	0.7757
1357/1358	40	0.0760	2220/2221	39	0.8147
1357/1359	40	0.0770	2260/2259	40	0.5664
1363/1364	39	0.1140	2265/2264	40	0.6410
1363/1365	39	0.1150	2284/2283	29	0.7168
1370/1369	39	0.1518	2294/2293	39	0.7544
1370/1371	39	0.1528	2304/2304	40	0.8300
1377/1376	40	0.1895	2355/2356	40	0.6966
1386/1385	40	0.2273	2361/2362	40	0.7342

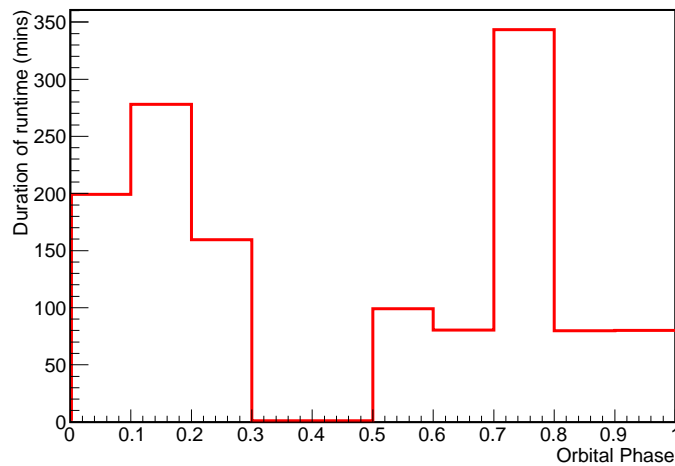


Figure 4.9: Distribution of orbital phase vs exposure time for the observation of LSI 61+303.

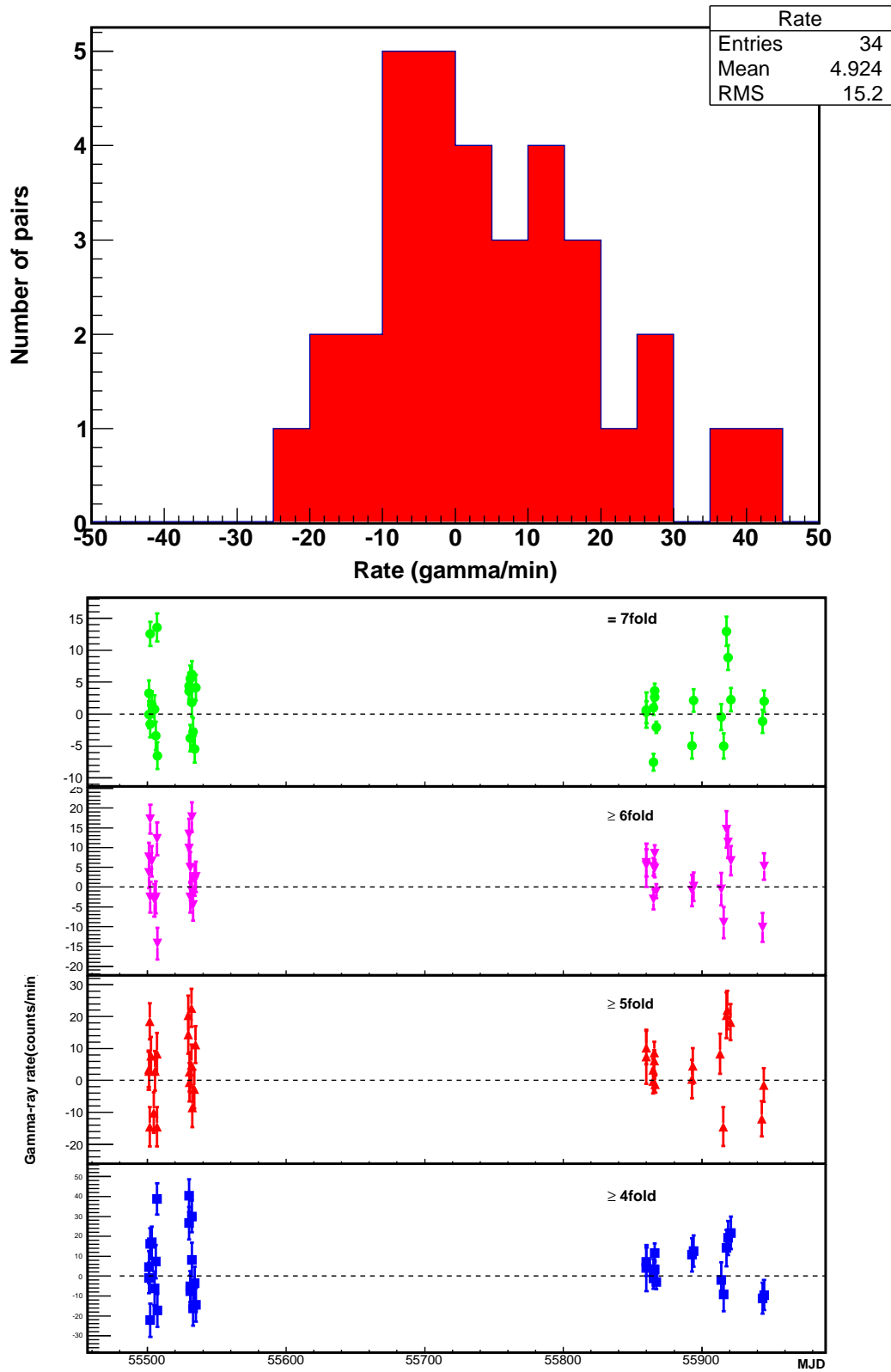


Figure 4.10: *Upper*: Distribution of gamma-ray rates for 34 pairs of LSI 61+303 for $\text{NTT} \geq 4$. *Lower*: Light curve of LSI 61+303 for different trigger conditions.

Table 4.8: Results of LSI + 61 303 for NTT equal to 4-fold, 5-fold, 6-fold and 7-fold.

fold	pairs	Excess	Error Excess	Duration (min)	Average gamma rate (/min)	Significance (σ)
=4	34	1434.9	469.3	1319.3	1.08 ± 0.35	3.1
=5	34	951.7	457.4	1319.3	0.72 ± 0.34	2.1
=6	34	2251.9	404.1	1319.3	1.70 ± 0.30	5.5
=7	34	1812.2	437.6	1319.3	1.37 ± 0.33	4.1

Table 4.9: Results of LSI + 61 303 for $\text{NTT} \geq 4$ -fold, 5-fold, 6-fold and 7-fold

fold	pairs	Excess	Error Excess	Duration (min)	Average gamma rate (/min)	Significance (σ)
≥ 4	34	6450.6	885.7	1319.3	4.88 ± 0.67	7.28
≥ 5	34	5015.8	751.1	1319.3	3.80 ± 0.56	6.67
≥ 6	34	4064.1	595.7	1319.3	3.08 ± 0.45	6.82
=7	34	1812.2	437.6	1319.3	1.37 ± 0.33	4.14

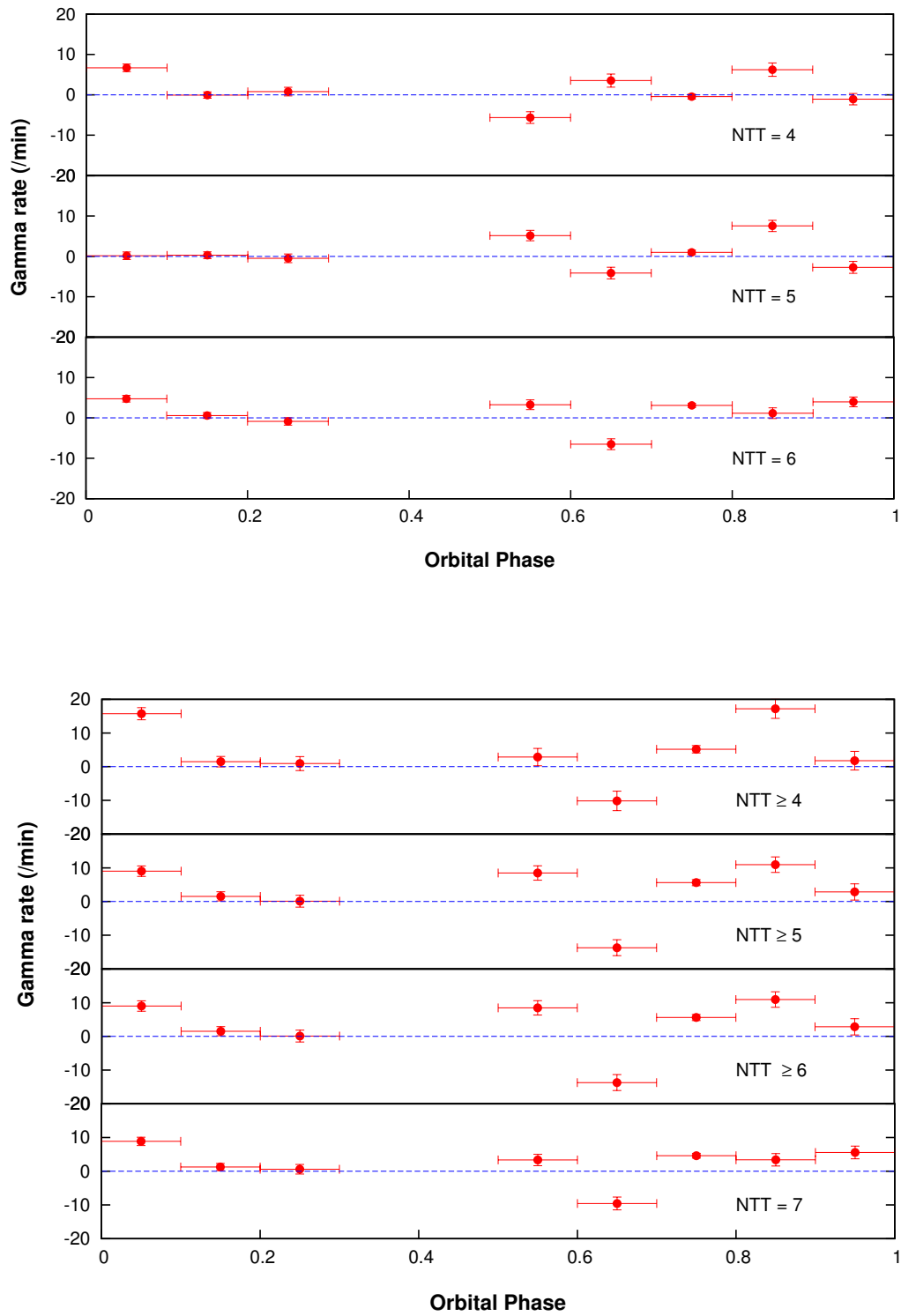


Figure 4.11: Gamma ray rates of LSI +61 303 as a function of orbital phase for different telescope trigger conditions.

4.4 MGRO J2019+37

MGRO J2019+37 is one of the brightest sources in the Cygnus region and was first discovered by the Milagro water Cherenkov telescope with very significant diffuse gamma-ray background. The Milagro collaboration detected it with 10.9σ significance above the isotropic background level [8] and reported this to be a new source in this region. The corresponding flux is about 70% of the Crab nebula flux at about 12 TeV. It is located towards the rich star-formation region in Cygnus and it is the brightest in gamma rays in this region. The RA (J2000) and dec (J2000) of the source are quoted to be $20^h 20^m 0^s$ and $36^\circ 43' 00''$, respectively. Since its detection in VHE gamma rays, although several studies have been done to explore the nature of this source, it still remains unknown. In addition, no confirmed counterparts of this TeV source at lower energies have yet been observed. However, several possible associations with other observed sources have been suggested. The air-shower array ARGO-YBJ [118] reported no signal from this source, and it concluded that the source could be variable. It has also been mentioned that the ARGO-YBJ exposure at energies above 5 TeV was not sufficient to draw a definite conclusion in this regard. Very recently, VERITAS has resolved MGRO J2019+37 into two VERITAS sources: VER 2016+371 and VER J2019+368 [119] and both of them are considered PWN type sources. The second one is detected at the level of 9σ significance and reported as the main contributor of MGRO J2019+37. Multi-wavelength modelling of this source based on available data is described in Chapter 5. In this section, we describe the results of observation with HAGAR system from the direction of this source.

4.4.1 Analysis and results

Data taken during 2010 is used in this analysis. Although, the MGRO J2019+37 was observed for a total of nearly 15 hours of data, after data quality check and analysis cuts only about 5.2 hours data are included in this analysis, which corresponds to 9 ON-OFF

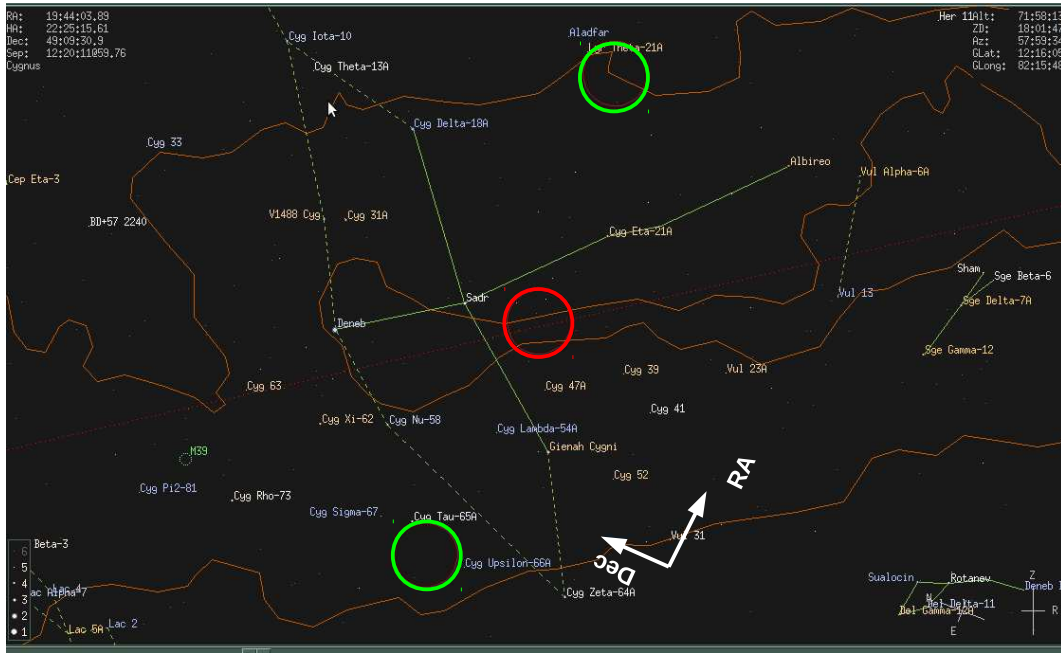


Figure 4.12: Location of the MGRO J2019+37 (3 degree radius red circle; ON-source region) in the sky along with the two background regions (green circles with radius 3 degree; OFF-source regions).

pairs. Those selected pairs for final analysis are shown in Table 4.10. The ON-source run with run number 1107 is a 80-minutes run, and the first half of this run is used to make a pair with the run 1106 and the second half is used to make a pair with 1108. Figure 4.12 indicates the location of the MGRO J2019+37 in the sky (red circle with radius 3 degrees) corresponding to ON-source run and the locations of two background regions (green circles) which correspond to OFF-source observations. The recorded relative delays in the arrival of Cherenkov pulses using TDCs are corrected by time offsets of each TDC channel, which are measured by vertical fixed-angle runs. The gamma-ray rates for different telescope triggering conditions are shown in Table 4.11 and Table 4.12. The distribution of gamma-ray rates and the light curve of MGRO J2019+37 are shown in the upper and lower panels of Figure 4.13, respectively. In one of the pairs, much higher value of gamma-ray rate could be due to systematic error which is not estimated for the

Table 4.10: Selected pairs for the MGRO J2019+37 analysis.

Year	Months	Run No. of Pairs	Number of pairs	duration (minutes)
2010	June-July	1049/1048; 1055/1054; 1057/1056; 1059/1058;	4	139
	July-August	1078/1077	1	40
	September-October	1107/1106; 1107/1108 1110/1109; 1114/1115	4	135

present analysis. The estimated flux is about $(5.39 \pm 0.72) \times 10^{-10}$ photons $\text{cm}^{-2} \text{s}^{-1}$ for energy above 210 GeV for $\text{NTT} \geq 4$. This flux is much higher than the corresponding flux of the Crab nebula. This could be due to systematic effect as explained in the case of the Crab nebula. In the case of higher telescope trigger conditions ($\text{NTT} \geq 4$ and above), the gamma-ray rates are lower than the rates estimated from simulations. However, they are slightly higher than the flux estimated by Milagro.

Table 4.11: Results of MGRO J2019+37 for NTT equal to 4-fold, 5-fold, 6-fold and 7-fold.

fold	pairs	Excess	Error Excess	Duration (min)	Gamma rate (/min)	Significance (σ)
=4	9	2103.91	244.36	314.76	6.68 ± 0.77	8.60
=5	9	540.44	219.74	314.76	1.71 ± 0.69	2.45
=6	9	203.34	202.97	314.76	0.64 ± 0.64	1.00
=7	9	413.30	210.80	314.76	1.31 ± 0.66	1.96

Table 4.12: Results of MGRO J2019+37 for $\text{NTT} \geq 4$ -fold, 5-fold, 6-fold and 7-fold.

fold	pairs	Excess	Error Excess	Duration (min)	Gamma rate (/min)	Significance (σ)
≥ 4	9	3260.99	440.04	314.76	10.36 ± 1.39	7.41
≥ 5	9	1157.08	365.95	314.76	3.67 ± 1.16	3.16
≥ 6	9	616.64	292.63	314.76	1.95 ± 0.92	2.10
=7	9	413.30	210.80	314.76	1.31 ± 0.66	1.96

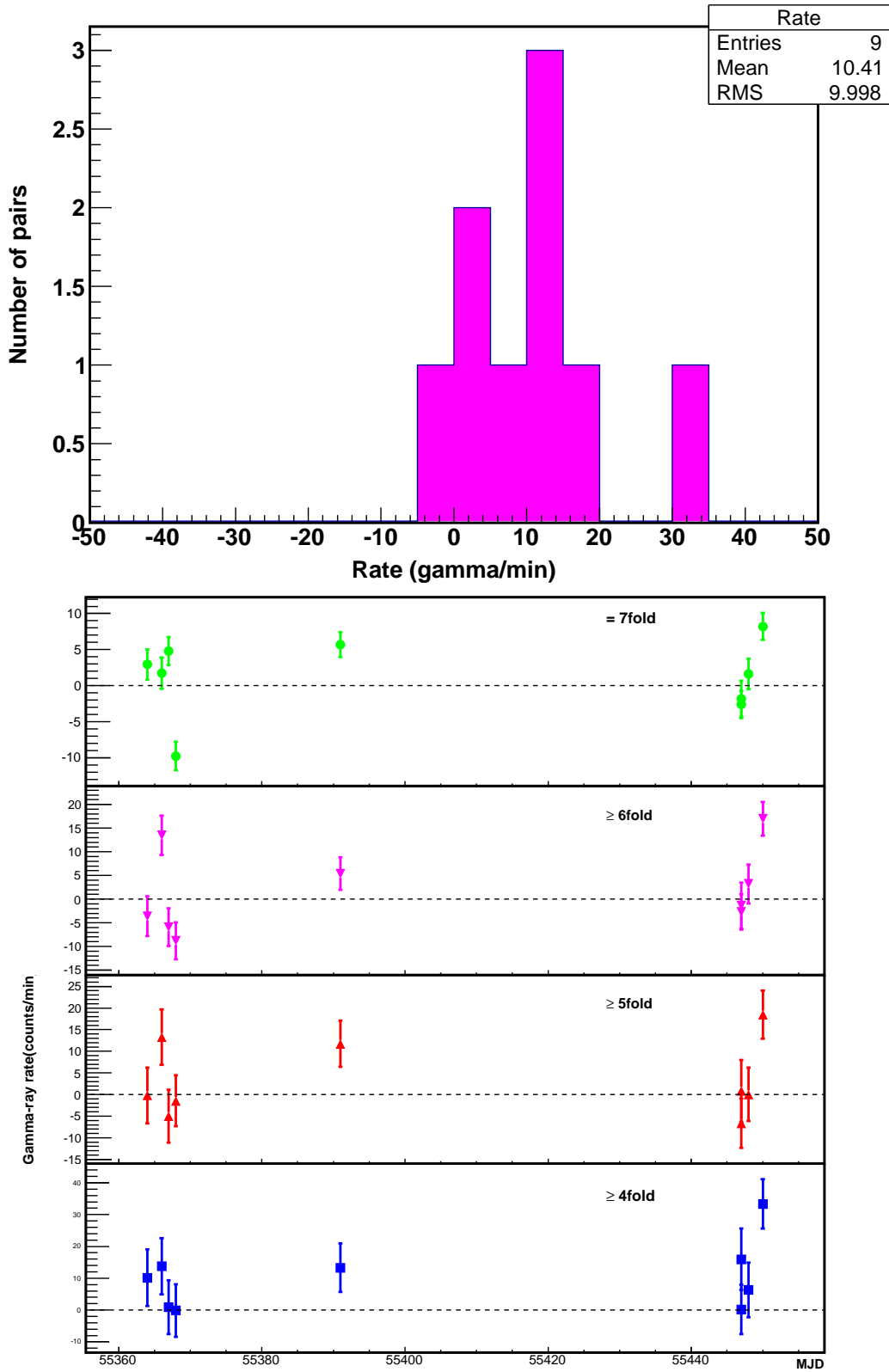


Figure 4.13: *Upper*: Distribution of gamma-ray rates for all 9 pairs for $\text{NTT} \geq 4$. *Lower*: Light curve for MGRO J2019+37 for all 9 pairs for different telescope triggering conditions.

4.5 Summary

Analysis of the Crab nebula data shows that the estimated Crab nebula fluxes for NTT greater than or equal to 5-fold and higher folds are consistent with the simulated results as well as with the results given by other experiments. However, due to higher systematics the estimated flux for $\text{NTT} \geq 4$ is higher than that estimated from simulations. In the case of LSI +61 303 analysis, we have detected the source in the orbital phases of 0.0–0.1 and 0.7–0.8 during the period 2010–2012. The MAGIC and the VERITAS telescopes had detected the source in the orbital phases 0.6–0.7 during 2005–2006. However, VERITAS observations during October 2010 showed the significant detection in the orbital phase of 0.07. These observations suggest that the source is variable in nature. Although MGRO J2019+37 is an extended source, we analysed the observed data assuming it as a point source. The analysis results of the MGRO J2019+37 showed that within the present HAGAR analysis procedure the estimated fluxes for $\text{NTT} \geq 5$ and above are higher than the flux estimated by Milagro and VERITAS collaboration. This inconsistency in flux measurement for MGRO J2019+37 reveals that present HAGAR data analysis which is restricted to point source observation, cannot be applied directly for analysis of extended sources. The possible way of making the data analysis compatible for extended sources is mentioned in the last Chapter of this thesis.

Chapter 5

Multi-wavelength modelling of TeV gamma-ray sources

As already mentioned, multi-wavelength modelling can provide important information about the nature of the sources of TeV emission. In this Chapter we discuss such modelling [25, 120] of two interesting TeV gamma-ray sources, namely Cassiopeia A and MGRO J2019+37.

5.1 Modelling of Cassiopeia A

Cassiopeia A (Cas A) is a historically well-known shell-type supernova remnant (SNR) observed in almost all wavebands, which includes radio [16, 121, 122, 123], optical [17], IR [18, 124], and X-rays [19, 20, 125, 126]. Cas A has been observed in TeV gamma rays by the HEGRA [127], MAGIC [21], and VERITAS [22] telescopes. Upper limits on the GeV gamma-ray emission were first reported by EGRET [128]. However, the first detection at GeV energies was reported by the Large Area Telescope on board the Fermi satellite (Fermi-LAT) [23]. The brightness of this source in all wavelengths makes it a unique Galactic astrophysical source for studying the origin of Galactic cosmic rays and

high-energy phenomena in extreme conditions. The distance to Cas A was estimated to be ~ 3.4 kpc [17].

Cas A has a symmetric and unbroken shell structure. Short and clumpy filaments have also been observed on the outer shell of Cas A [129]. However, there is no clear evidence, such as OH maser emission, for interaction between dense molecular clouds and the shell of Cas A. In X-rays, Chandra observed the shell of Cas A with high angular accuracy ($\sim 0''.5$). Since the angular resolution is worse for gamma-ray measurements ($\sim 360''$) [21, 22], Cas A was observed as a point-like source in gamma rays. There is a CCO (compact central object) located very close to the centre of Cas A [130]. Unlike a typical energetic pulsar [131], a CCO is not capable of producing enough TeV gamma rays for detection. Therefore, the gamma-ray emission from Cas A is likely to originate from the shell of the SNR.

Evidence for acceleration of cosmic electrons was found at the location of outer shocks [129, 132, 133] and at the reverse shock inside the Cas A [134]. Ref. [134] showed that the X-ray filaments and knots in the reverse shock are efficient acceleration sites. Acceleration of particles to TeV energies was established by HEGRA [127], MAGIC [21], and VERITAS [22] data. The diffusive shock acceleration mechanism is a well-established model for the acceleration of cosmic-ray particles (both electrons and protons). The studies [135, 136] on the spectral energy density (SED) of Cas A at GeV–TeV energies were limited to the whole remnant and did not extend to different regions of the shell. Recently, based on the analysis of the 44 months' Fermi-LAT data, it has been reported [137] that the hadronic emission is dominating in the GeV energy range.

In this section, we present the study of five regions, south (S), south-east (SE), south-west (SW), north-east (NE), and north-west (NW), of the shell of Cas A in X-ray energies (see Figure 5.1), which show different levels of X-ray fluxes (see Figure 5.2). We model the X-ray spectra from these regions using a leptonic model following Ref. [61]. We use the multi-wavelength data, that is, radio data [16], X-ray data from Chandra [20, 125],

Fermi-LAT data [25], MAGIC [21], and VERITAS [22] data. Results of Fermi-LAT data that was taken over ~ 60 months of operation during the period 2008 August to 2013 June are considered in this study. We interpreted the multi-wavelength SED and determine the region of the shell which contributes the most to the total gamma-ray emission from Cas A.

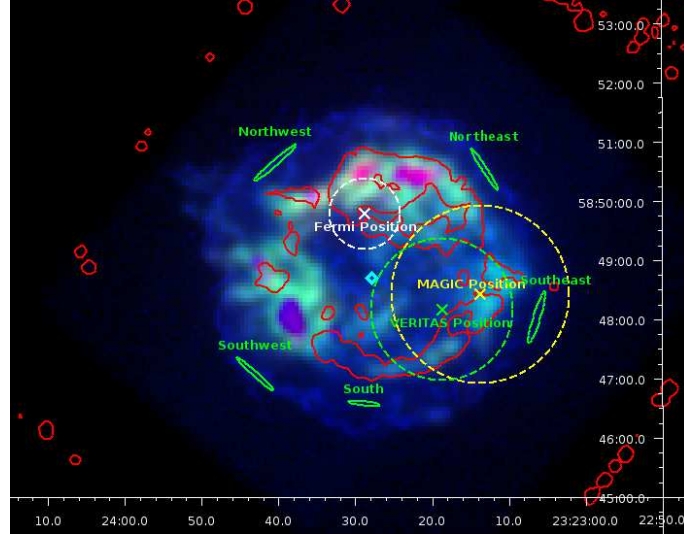


Figure 5.1: Multi-colour image (dec vs. RA in J2000) of Cas A produced using Chandra X-ray data. The red, green, and blue colour hues represent the energy ranges of $[0.7, 1.0]$, $[1.0, 3.5]$, and $[3.5, 8.0]$ keV, respectively. The red and green hues are smoothed in linear colour scale, while the blue hues are shown in logarithmic scale to enhance the view of the smallest number of X-ray counts existing in the outer shell. The green ellipses represent the S, SW, SE, NW, and NE of the shell. The green and yellow crosses and dashed circles correspond to the VERITAS and MAGIC observation locations and approximated location error circles. The white cross and dashed circle are for the GeV gamma-ray emission best-fit location and the location error circle from the analysis in this thesis. The CCO location is shown with a cyan open diamond. The red contours represent the CO-detected regions by Spitzer-IRAC for infrared flux densities starting from a value of 0.4 MJy/sr and higher [138].

5.1.1 Modelling the spectrum

Leptonic model

The non-thermal X-ray emission in the selected regions (i.e., S, SE, SW, NE, and NW) can be explained by the synchrotron emission from relativistic electrons in the source. Since relativistic particle spectra fall off roughly exponentially based on either an acceleration

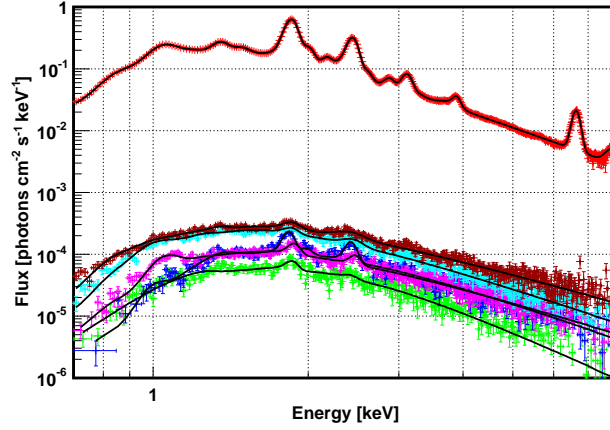


Figure 5.2: X-ray spectra of the five different shell regions and the whole remnant: (a) green for S, (b) blue for SE, (c) magenta for SW, (d) cyan for NE, (e) brown for NW, and (f) red for the whole remnant. Corresponding best-fit X-ray spectra are shown by black lines [25].

time scale [139] or radiative loss [140], we consider a relativistic electron distribution that follows a power-law with an exponential cut-off, namely

$$\frac{dN}{d\gamma} = N_e \gamma^{-\alpha} \exp\left(-\frac{\gamma}{\gamma_{\max}}\right), \quad (5.1)$$

where N_e and γ_{\max} are the constant of proportionality of electron distribution and the Lorentz factor of the cut-off energy of the electrons, respectively. The spectrum of the synchrotron radiation for a power-law distributed electrons can be written as [61],

$$F_\nu \propto N_e B^{(\alpha+1)/2} \nu^{-(\alpha+1)/2}, \quad (5.2)$$

where B is the magnetic field in the emission volume. Equation (5.2) shows that the synchrotron radiation depends on three parameters, N_e , B , and α . From the observed radio spectrum, $S_\nu \propto \nu^{-0.77}$ [16], the power-law spectral index, α , is estimated to be 2.54. Hence, the value of F_ν now changes with N_e (which is a measure of the electron density in the SNR) and magnetic field (B). In the case of two-zone model [135], the source

is considered to be consisted of two different regions, namely zone 1 and zone 2. The zone 1 consists of compact, bright steep-spectrum radio knots (radio-emitting filamentary structures with angular size of about 1 arcmin and compact structures with size less than $2.0 \text{ arcsec} \times 2.3 \text{ arcsec}$.) and the bright fragmented radio ring and the zone 2 consists of the diffuse plateau of CasA. The magnetic fields from the radio knots (zone 1) and from the shell of the remnant (zone 2) were estimated based on the observed radio data. In this two-zone scenario of Cas A, the magnetic field energy densities are different for the two zones, but the density of relativistic electrons in these zones are comparable to each other [135]. Hence, we used the uniform electron density for all the shell regions in our model calculations. If N_e is fixed, then the level of synchrotron flux depends only on the magnetic field.

Table 5.1: The magnetic field parameters for the synchrotron spectra for all selected regions.

Region	Magnetic Field (B) [μG]
South	250 ± 30
Southwest	330 ± 18
Southeast	330 ± 18
Northeast	410 ± 21
Northwest	510 ± 15

The Chandra observations from different regions of the shell show unequal levels of X-ray fluxes, which can be attributed to different magnetic fields in those regions. These different magnetic fields thus contribute to the gamma-ray fluxes through inverse Compton (IC) and bremsstrahlung processes. To estimate the contribution to gamma rays, we first considered that the whole remnant is uniform in X-ray flux and the southern part of the remnant contains only a fraction of the flux from the whole remnant. In the two-zone model of Cas A [135], the mean magnetic field in the shell region was found to be $300 \mu\text{G}$, and the energy content of relativistic electrons in this region was calculated to be about 10^{48} erg. Here, we assume a somewhat lower magnetic field, that is, $250 \mu\text{G}$ for the S-region of the shell and the other model parameters for the synchrotron emission

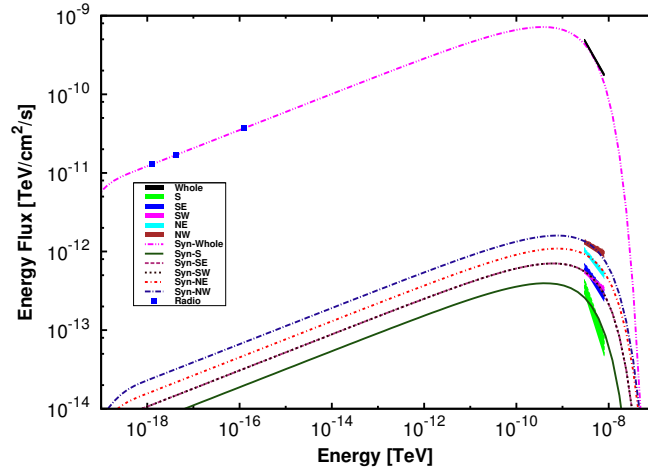


Figure 5.3: Synchrotron spectra with the observed best-fit X-ray data for different regions of the shell. The spectral index describing radio emitting electrons for all the regions is $\alpha = 2.54$. The estimated magnetic fields for different shell regions are: $250 \mu\text{G}$ for S (solid line); $330 \mu\text{G}$ for SE (dashed line) and SW (dotted line); $410 \mu\text{G}$ for NE (dot-dashed line); $510 \mu\text{G}$ for NW (long dash-dotted line), and $250 \mu\text{G}$ for the whole remnant (double dot dashed line). The best-fit X-ray fluxes of the S, SE, SW, NE, NW, and the whole remnant are shown with green, blue, magenta, cyan, brown, and black stripes.

process are estimated from the fit to the corresponding observed best-fit X-ray data. We then estimate the magnetic fields for all other regions using the same electron density and same power-law spectral index. The calculated magnetic field values for all the shell regions are shown in Table 5.1. Based on the flux upper limit given by SAS-2 and COS B detectors, a lower limit on the magnetic field in the shell of Cas A was estimated to be $80 \mu\text{G}$ [141], and our estimated magnetic fields are consistent with this lower limit on the magnetic field. The rest of the parameters are fixed for all the regions, which are the following: spectral index, $\alpha = 2.54$, $\gamma_{\text{max}} = 3.2 \times 10^7$, and distance = 3.4 kpc. The fitted synchrotron spectra and the observed best-fit X-ray spectra for different regions are shown by lines and stripes, respectively, in Fig. 5.3.

The inverse Compton (IC) emission spectrum for the whole remnant was estimated using the parameters of the leptonic model obtained for each of the regions in the shell. The IC spectrum can be estimated in two different ways for each of the regions in the shell. First, the magnetic field for each region was considered to be the mean magnetic field for the whole remnant. Then parameters for the input spectrum were obtained from the fit to

the observed radio and X-ray data. Once all the parameters for leptonic model were estimated, IC spectrum could be calculated. Secondly, we multiplied the radio synchrotron spectrum for each region by a scale factor, which was estimated by dividing the whole remnant's observed radio or X-ray flux by the corresponding estimated synchrotron flux of this shell region. By considering scattering of electrons on far infra-red dust emission at $T = 97$ K, which dominates over cosmic microwave background photons as seed photons in the emission process [135], the estimated IC spectra are shown in Fig. 5.4 for the shell regions. If the shell region is dominated by strong magnetic field (e.g. $510 \mu\text{G}$), then the IC component of radiation is reduced, which is evident from Fig. 5.4. It shows that the TeV flux from the S-region of the shell is higher than those from other regions of Cas A.

Table 5.2: Parameters used for calculating the bremsstrahlung spectrum contributing to the emission from the S-region of the SNR.

Parameters	Values
γ_{max}	3.2×10^7
n_H	10 cm^{-3}
α	2.54
Energy (W_e)	$4.8 \times 10^{48} \text{ erg}$

It is evident from Fig. 5.4 that the TeV data at higher energy bins fit better with the IC prediction for the S-region among all other regions. However, the Fermi-LAT spectral data points at GeV energies cannot be explained by the IC mechanism alone, and it has to be modelled by an additional component, like the bremsstrahlung process or the neutral pion decay model.

Therefore, we estimated the contribution of bremsstrahlung process to explain fluxes at both GeV and TeV energies. The parameters corresponding to the S-region was used to calculate the bremsstrahlung spectrum considering ambient proton density to be $n_H = 10 \text{ cm}^{-3}$ [142]. The total energy of the electrons was estimated to be $W_e = 4.8 \times 10^{48} \text{ erg}$. The parameters used for this emission process is shown in Table 5.2. Figure 5.5 shows that the bremsstrahlung process alone cannot explain the GeV and TeV data simultaneously.

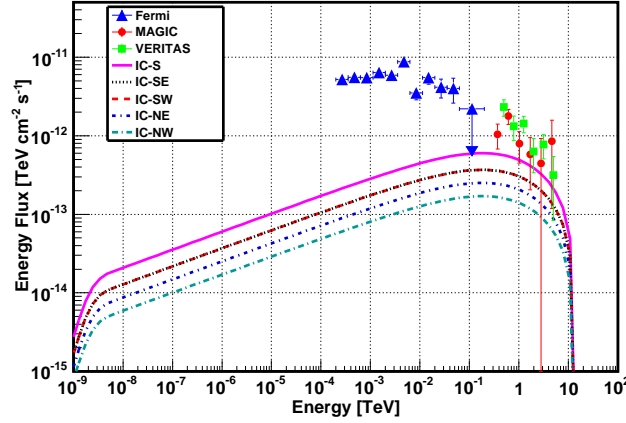


Figure 5.4: IC spectra of the whole remnant, based on parameters related to different regions of the shell. The spectra for the different regions are as indicated: S (solid line), SE (dotted line), SW (dashed line), NE (dot-dashed), and NW (long dashed-dotted). The spectra for SE and SW are overlapping. The parameters for radio emitting electrons are $\alpha = 2.54$, $\gamma_{max} = 3.2 \times 10^7$.

Since the bremsstrahlung flux depends linearly on the ambient proton density, higher values of ambient proton density can increase the GeV–TeV fluxes to observed fluxes at these energies. Using the mass of supernova ejecta, $M_{ejecta} = 2M_{\odot}$ [143, 142], where M_{\odot} is the solar mass, the effective gas density was found to be $n_{eff} \simeq 32 \text{ cm}^{-3}$ [23]. It is also not possible to explain GeV–TeV data with this density of ambient gas. Moreover, Fig. 5.5 shows that the shape of the observed GeV spectrum near 1 GeV is different from that of bremsstrahlung spectrum, which rises as it goes from GeV to lower energies.

Hadronic model

Since the leptonic model is not able to account for the observed gamma-ray emission at GeV energies, we need to invoke hadronic scenario to explain the observed GeV fluxes. The gamma-ray flux resulting from the neutral pion (π^0) decay of accelerated protons was estimated by considering ambient proton density to be 10 cm^{-3} . The accelerated protons were considered to follow a broken power-law spectrum with an exponential cut-off as

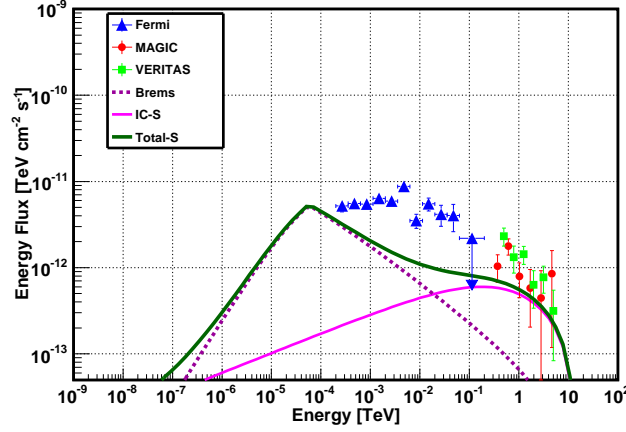


Figure 5.5: Gamma-ray spectrum for Cas A. The IC (solid line) and bremsstrahlung (dashed line) spectra are estimated for the whole remnant when parameters are based on S-region of the shell. Bremsstrahlung spectrum is calculated for $n_H = 10 \text{ cm}^{-3}$. The thick solid line corresponds to total contribution to gamma rays from leptons. The parameters for radio emitting electrons are $\alpha = 2.54$, $\gamma_{max} = 3.2 \times 10^7$.

shown in Equation (5.3).

$$\begin{aligned}
 \frac{dN}{dE_p} &= N_1 E_p^{-\rho} \text{ for } E_p^{min} \leq E_p < E_p^{break} \\
 &= N_2 E_p^{-\beta} \exp\left(-\frac{E}{E_p^{max}}\right) \text{ for } E_p^{break} \leq E_p,
 \end{aligned} \tag{5.3}$$

where N_1 and N_2 are two normalisation constants and ρ and β are spectral indices before and after the break at E_p^{break} . Figure 5.6 shows the contribution of gamma-ray flux from the π^0 decay calculated following [63]. The gamma-ray spectrum was fitted within the observed GeV–TeV energy range (see Fig. 5.6), and the corresponding best fit parameters are shown in Set-I of Table 5.3. The total energy of the protons in the hadronic model was estimated to be $W_p = 5.7 \times 10^{49} (10 \text{ cm}^{-3}/n_H) \text{ erg}$. We would like to note that we are considering gamma-ray spectrum for the whole remnant, because the angular resolutions of the current generation gamma-ray instruments are not comparable to those of the X-ray instruments.

It has been already mentioned in Section 5.1.1 that the leptonic model can only account for the TeV fluxes at the highest energy bins, whereas the observed GeV fluxes can be

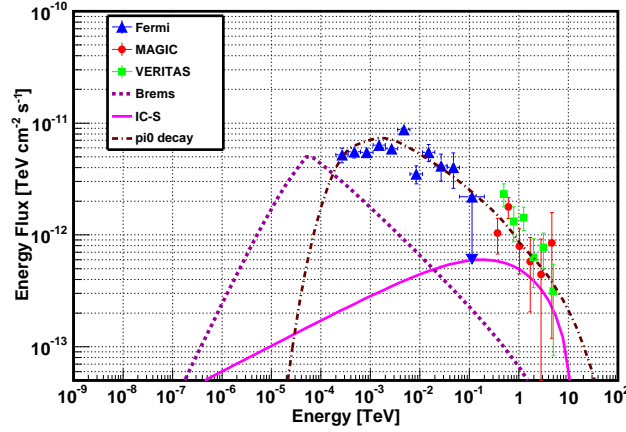


Figure 5.6: Same as Fig. 5.5. Only π^0 decay spectrum for the power-law distributed proton spectra (long dash-dotted line) is included. The parameters used to get the π^0 decay spectrum are shown in Table 5.3 by parameter Set-I. The estimated total energy of the protons, $W_p = 5.7 \times 10^{49}$ erg.

explained by hadronic model as shown in Fig. 5.6. To get a complete understanding of the spectrum at GeV–TeV energies, we have to estimate the combined spectrum resulting from both leptonic and hadronic model (hereafter, lepto-hadronic model). Since the parameters for the leptonic model are fixed by observed radio and X-ray fluxes, the resulting parameters for the hadronic model for the combined GeV–TeV spectrum are different from the parameters listed in Table 5.3 (see Set-I). The best-fit parameters for the lepto-hadronic model are given in Set-II of Table 5.3, and it shows that the corresponding χ^2 value is less than that of purely hadronic model. The corresponding spectrum is shown in Fig. 5.7. The maximum energy of protons (E_p^{max}) is fixed to 100 TeV for both pure hadronic and lepto-hadronic model. The total energy of the charged particles for the lepto-hadronic model is $W_e + W_p = 3.4 \times 10^{49}$ erg, which gives a conversion efficiency of supernova explosion energy to be less than 2%, which is consistent with the value reported in Ref. [137]. The estimated electron to proton ratio is about 0.05, and this is consistent with the values of the ratio for the observed cosmic rays. Although the GeV data corresponds to the best fit location as shown in Fig. 5.1 using white dashed circle, it is to be mentioned that the gamma rays are not being emitted from other regions of Cas A. Hence, there is no inconsistency in combining GeV–TeV data to get best fitted emission

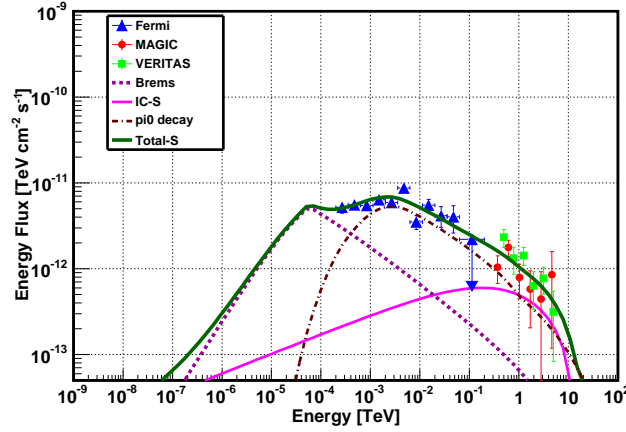


Figure 5.7: Gamma-ray spectrum (thick solid line) for Cas A obtained by combining both leptonic and hadronic contributions to the whole remnant data. Parameters for leptonic model spectra (IC: solid line and bremsstrahlung: dashed line) correspond to S-region of the remnant. Parameters for hadronic model are shown in Table 5.3 by Set-II (long dash-dotted line).

model.

Table 5.3: Parameters for gamma-ray production through decay of neutral pions.

Parameters	Set-I (hadronic)	Set-II (hadronic+leptonic)
ρ	2.05 ± 0.05	1.26 ± 0.2
β	2.36 ± 0.02	2.44 ± 0.03
E_p^{max} (TeV)	100	100
E_p^{break} (GeV)	17	17
Energy (W_p) (erg)	5.7×10^{49}	2.97×10^{49}
χ^2/dof	2.5	1.8

5.1.2 Discussion

The aim of this study was to locate the region of the shell of Cas A which is brightest in gamma rays and to interpret the observed fluxes at GeV–TeV energies in the context of both leptonic and hadronic models. From the different levels of X-ray flux in several shell regions, we found that the magnetic fields are different in those regions. Since IC flux becomes less significant with higher magnetic field, the NW region of the shell of the remnant is the least significant in producing gamma-ray fluxes through IC process

among all other shell regions. On the other hand, the S-region of the remnant becomes a significant region for production of IC fluxes due to the lower magnetic field in this region. Although we have considered same spectral index for radio emitting electrons, different choices of spectral indices do not change the overall conclusion.

In addition, we see from Fig. 5.5 that IC fluxes can explain the data only at TeV energies while the bremsstrahlung process is unable to explain the GeV–TeV data for ambient gas density 10 cm^{-3} . Moreover, the bremsstrahlung process was also unable to explain the observed fluxes properly with higher values of ambient gas density ($\sim 32 \text{ cm}^{-3}$). Therefore, we conclude that the leptonic scenario is insufficient to explain the observed GeV and TeV gamma-ray fluxes simultaneously. Hence, we need to invoke hadronic contribution to account for the observed gamma-ray fluxes. The gamma-ray spectrum that results from decay of π^0 s in Fig. 5.6 shows that it alone can explain the GeV and TeV fluxes with a χ^2 value of 2.5. Since we have already seen that the leptonic scenario can contribute to TeV energies, we cannot ignore this completely. So we estimated the total contribution from both the leptonic and hadronic model to explain the data. Figure 5.7 shows that the gamma-ray spectrum due to decay of π^0 along with leptonic model is able to explain the GeV–TeV gamma rays for the ambient gas density of 10 cm^{-3} . Moreover, the best fit χ^2 value for this case is less than that of the case of purely hadronic model, as shown in Table 5.3. Although increasing the effective density of the ambient gas to higher values (than the estimated average density) may help the bremsstrahlung model to reach the level of GeV–TeV data, the gamma-ray fluxes due to the π^0 decay of accelerated protons also increase. Therefore, the π^0 decay process would no longer be able explain the GeV–TeV data unless the total energy budget of the protons is reduced. That, in turn, indicates a lower conversion efficiency of the explosion energy of Cas A into accelerating protons. The GeV flux that falls below 1 GeV is considered to be a clear indication for the π^0 decay origin of gamma-ray emission. Very recently, it was reported [137] that the Fermi-LAT data analysis of Cas A resulted in the gamma-ray emission to be hadronic in nature. A higher density of ambient gas may establish the fact of having higher potential for pro-

ducing gamma rays through π^0 -decay process for the S-region. Nevertheless, the total contribution to TeV energies due to both leptonic and hadronic models cannot be ignored.

According to Ref. [129], the magnetic field at the forward shock is within the range of 80–160 μG , whereas the mean magnetic field value in the shell of Cas A was estimated to be $\sim 300 \mu\text{G}$ [135, 144]. Although it was showed [23] that the leptonic model for the magnetic field of 120 μG can broadly explain the observed GeV–TeV fluxes, the corresponding spectrum from leptonic model does not fit well. With a lower value of the magnetic field (i.e. $< 120 \mu\text{G}$), the TeV fluxes can be overestimated by IC emission spectrum. If we consider the magnetic field for the S-region of the shell to be about 120 μG , the lepto-hadronic model has to be sufficiently modified to explain the total fluxes. The total fluxes from the lepto-hadronic model exceeds the observed values, and the corresponding χ^2 value for the best fit parameters becomes large. This overestimated flux cannot be compensated by lowering the contribution from hadronic model. Hence, we need to consider higher values of magnetic field ($\sim 250 \mu\text{G}$), so that the total spectrum from lepto-hadronic model can explain the data better than both a pure leptonic and a pure hadronic model.

The most interesting result is the relatively low total accelerated particle energy (of the order of 2% conversion efficiency) that is combined with the high magnetic field estimate. This amplification of a magnetic field can either be related through magneto-hydrodynamic waves generated by cosmic rays [145, 146] or could result from the effect of turbulent density fluctuations on the propagating hydrodynamic shock waves, which has been observed through two-dimensional magneto-hydrodynamic numerical simulations [147]. The low conversion efficiency of cosmic rays suggests that the cosmic ray streaming energy may not be sufficient enough to be transferred to the magnetic fields that result from magnetic amplification. Hence, the magnetic field amplification in the down-stream of shocks due to presence of turbulence could be favourable in this particular remnant.

It is to be mentioned that the differences in the X-ray flux levels for different regions of Cas A can be attributed to the different densities of the injection of the electrons. For different densities, however, there may not be any difference in gamma-ray fluxes from different regions of the shell. However, this needs a detailed investigation of the density profile of the relativistic electrons in this source.

5.1.3 Summary & conclusion

We found that the gamma-ray emission from the S-region of the shell through IC process has the highest flux value, and this predicted flux matches better to the TeV data in comparison to flux predictions from other regions of the shell. The second best-fit IC prediction with the TeV data is from the SE and SW and then the NE region. We also found that the leptonic model alone is unable to explain the observed GeV fluxes for any regions of the shell. However, the GeV and TeV gamma-ray data fit reasonably well to the hadronic model, which is independent of the selected regions on the shell.

If the SNR would be perfectly symmetric in shape, we would expect that the radiation fluxes from each region of the shell should be approximately equal. Apparently, the shell's emission is not homogeneously distributed. The reason for the variations in X-ray and gamma-ray fluxes can be due to different amounts of particles or variations in the magnetic field at different regions of the SNR's shell. The molecular environment might also be different at different sides of the shell. Future gamma-ray instruments with far better angular resolution (e.g., CTA) will be required to understand the spectral and spatial structure of the remnant in gamma rays.

5.2 Modelling of MGRO J2019+37

The Cygnus region of the Galaxy hosts a number of extended, unidentified sources of TeV γ -ray emission, the most prominent of which is MGRO J2019+37 discovered by the Milagro experiment [8, 9]. Detailed analysis [10] of the observational data on this object collected during the period 2005–2008 gives a detection of this source with a statistical significance in excess of 12σ between 1 and 100 TeV. The measured flux [10] from this source is $7_{-2}^{+5} \times 10^{-10} \text{ s}^{-1} \text{ m}^{-2} \text{ TeV}^{-1}$ (with a $\sim 30\%$ systematic uncertainty) at 10 TeV with a spectrum that is best described by a power-law with a spectral index of $2.0_{-1.0}^{+0.5}$ (with a systematic uncertainty of ~ 0.1) and an exponential cutoff at an energy $E_c = 29_{-16}^{+50} \text{ TeV}$. It should be mentioned, however, that the ARGO-YBJ air-shower experiment in their observations [118] in the region of MGRO J2019+37 did not get a detectable signal from this object, instead placing an upper limit [118] on the flux at energies below 5 TeV at a level lower than that measured by the Milagro experiment. On the other hand, as mentioned in Ref. [118], the ARGO-YBJ exposure at energies above 5 TeV was not sufficient to draw a definite conclusion in this regard. However, very recently, the VERITAS telescope system has resolved the VHE emission from MGRO J2019+37 into two VERITAS sources: VER J2016+371 and VER J2019+368 [119]. VER J2019+368 is a bright extended source, and it coincides well with the centre region of MGRO J2019+37 and accounts for bulk of the emission from this source.

Although no confirmed counterparts of the TeV source MGRO J2019+37 at lower energies are known, several possible associations with other observed sources have been suggested. The emission from MGRO J2019+37 may be due to either a single extended source or several unresolved sources. The EGRET sources 3EG J2021+3716 and 3EG J2016+3657 are positionally close to MGRO J2019+37, and thus could be the GeV counterparts of MGRO J2019+37 if it is a multiple source. At the same time, the EGRET source 3EG J2021+3716 is suggested to be associated with the radio and GeV pulsar PSR J2021+3651 (and its associated pulsar wind nebula PWN G75.2+0.1

[13, 14]) observed at GeV energies by AGILE (AGL J2020.5+3653) [15] as well as FERMI (OFGL J2020.8+3649) [12]. A SWIFT/XRT observation [148] was also done within the positional uncertainty region of MGRO J2019+37 reported in [8, 9] and three X-ray sources were reported in the region with a total X-ray flux corresponding to $\nu F_\nu \sim 8.1 \times 10^{-14} \text{ TeV cm}^{-2} \text{ s}^{-1}$ in the 2–10 keV energy region, which can, therefore, be taken as an upper limit on the possible X-ray flux from any X-ray counterpart of MGRO J2019+37 in this energy region. In addition, a wide-field deep radio survey of the MGRO J2019+37 region at 610 MHz was made by the Giant Metrewave Radio Telescope (GMRT) [11], yielding no detectable radio source, thus giving a conservative upper limit of $\sim 1.0 \text{ mJy}$ on the radio flux from any point-like radio counterpart of MGRO J2019+37.

Here, we study the implications of a scenario in which the observed TeV γ -ray emission from MGRO J2019+37 arises from a Pulsar Wind Nebula (PWN) type source. Pulsar Wind Nebulae (PWNe) (see, e.g., Ref. [149] for a review), the most well-known example of which is the Crab Nebula (see Ref. [150] for a review), are known to be sources of very high energy gamma rays extending to TeV energies (see, e.g., Ref. [62, 151] for reviews). The very high energy (GeV – TeV) gamma rays are thought to be produced mainly through the so-called synchrotron self-compton mechanism, i.e., inverse Compton (IC) interaction of high energy electrons with low energy synchrotron photons emitted by the electrons themselves in the ambient magnetic field in the nebula. The photons constituting the cosmic microwave background (CMB) and infrared photons due to dust act as additional target photons for the IC scattering of the high energy electrons. The high energy electrons themselves are thought to be accelerated in the wind termination shock where the ultra-relativistic wind from the pulsar residing within the nebula is stopped by the nebular material. In principle, in addition to electrons high energy protons (and in general heavier nuclei) may be also accelerated [152, 153, 154, 155], which can produce high energy photons through decay of neutral pions produced in inelastic p - p collisions. In this thesis we shall restrict our attention to emission only due to electrons. We use multiwavelength data and flux upper limits from observations in the region around MGRO

J2019+37 including the radio upper limit given by GMRT [11], X-ray flux upper limit from SWIFT/XRT observations [148], GeV observations by FERMI [12], EGRET [42] and AGILE [15], and the TeV data from Milagro [8, 9, 10] and VERITAS [119], to set constraints on the parameters of the emission model.

We find that the PWN scenario of origin of the observed TeV flux of MGRO J2019+37 is severely constrained by the upper limit on the radio flux from the region around MGRO J2019+37 given by the GMRT as well as by the X-ray flux upper limit from SWIFT/XRT. Specifically, the GMRT and/or SWIFT/XRT flux upper limits impose upper limits of $O(10^{-3} \text{ pc})$ on the characteristic size of the emission region within the PWN for an assumed distance of $\sim \text{few kpc}$ to the source. This is about three orders of magnitude less than the characteristic size of the emission region typically invoked in explaining the TeV emission from a “standard” PWN such as the Crab Nebula.

The reason for the upper limit on the size of the emission region in the PWN scenario is not hard to understand: Heuristically, ignoring for the moment the details of the energy spectrum of the electrons, let n_e be the number density of the electrons and r_{em} the characteristic radius of the (assumed spherical) emission region in the source. Recall that the TeV photons are produced through IC interaction of the nebular high energy electrons with primarily the synchrotron photons produced by the electrons themselves in the magnetic field in the nebular region. Since the number density of the synchrotron photons scales as n_e , the number density of the TeV photons produced by all the electrons roughly scales as n_e^2 . Thus, for a given distance to the source, the emerging TeV flux from the source scales as $n_e^2 r_{\text{em}}^2$. The requirement of producing the observed TeV flux of MGRO J2019+37, therefore, fixes the product $n_e r_{\text{em}}$. On the other hand, the photon fluxes in the radio and X-ray regions scale with the product $n_e r_{\text{em}}^2$ since those photons arise directly from synchrotron radiation of the electrons. Therefore, with the product $n_e r_{\text{em}}$ fixed by the observed TeV flux of MGRO J2019+37, an upper limit on the radio flux given by GMRT or the X-ray flux given by SWIFT/XRT directly yields an upper limit on r_{em} .

These arguments are elaborated upon more quantitatively in the following sections.

5.2.1 Injection spectra of electrons

Following the example of the Crab nebula, we shall assume that the nebula harbors two distinct populations of high energy electrons [152, 55]: (a) the “relic” (or “radio”) electrons whose synchrotron emission is responsible for the radio and FIR emission from the nebula, and (b) the “wind” electrons that, through their synchrotron emission, give rise to higher energy radiation extending to X-ray and gamma rays up to several hundred MeV. The radio electrons comprise of the electrons that were injected during the very early phase of rapid spin-down of the pulsar and which have since cooled down and accumulated within the nebula [156]. The wind electrons, on the other hand, are the ones that are being freshly accelerated at the pulsar wind termination shock and are being currently injected into the system. The IC interaction of the high energy wind electrons with the soft photons produced by the radio electrons as well as with CMBR and IR photons can then give rise to the observed multi-TeV emission. For simplicity, we work within the framework of the so-called “constant B-field” scenario [157, 55] and assume the magnetic field to be constant within the nebular region.

We take the following forms [55] for the radio and wind electron spectra, $\frac{dn_e^r}{d\gamma}$ and $\frac{dn_e^w}{d\gamma}$, respectively:

$$\frac{dn_e^r}{d\gamma} = \begin{cases} A_e^r \gamma^{-\alpha_r} & \text{for } \gamma_{\min}^r \leq \gamma \leq \gamma_{\max}^r, \\ 0 & \text{otherwise,} \end{cases} \quad (5.4)$$

and

$$\frac{dn_e^w}{d\gamma} = A_e^w \exp\left(-\left[\frac{\gamma_{\min}^w}{\gamma}\right]^\beta\right) \times \begin{cases} \left(\frac{\gamma}{\gamma_b}\right)^{-\alpha_w}, & \text{for } \gamma < \gamma_b, \\ \left(\frac{\gamma}{\gamma_b}\right)^{-\alpha'_w}, & \text{for } \gamma_b \leq \gamma \leq \gamma_{\max}^w, \\ 0, & \text{for } \gamma > \gamma_{\max}^w. \end{cases} \quad (5.5)$$

The parameters A_e^r , α_r , γ_{\min}^r , γ_{\max}^r , A_e^w , β , α_w , α'_w , γ_{\min}^w , γ_{\max}^w , and γ_b , are to be determined by comparison of the resulting photon spectra with the observational data and multiwavelength constraints.

5.2.2 Multiwavelength photon spectra and constraints

It is clear that, unlike in the case of the Crab Nebula for which the existence of detailed multiwavelength data allows determination of the parameters of the model by performing detailed spectral fits to observational data [55], it is not practical or even meaningful to attempt to “determine” the parameters appearing in equations (5.4) and (5.5) for the PWN model of MGRO J2019+37 because of lack of such multiwavelength observational data. Instead, we shall focus on the plausible ranges of values of the most relevant parameters of the model by requiring that the resulting multiwavelength photon spectra be such as to be able to explain the observed TeV flux from MGRO J2019+37 without violating the upper limits on the X-ray and radio fluxes from the region around the object. In this exercise we have been primarily guided by simple arguments of energetics based on the example of the Crab Nebula as a sort of “standard” PWN.

Let n_e^r and n_e^w in equations (5.4) and (5.5) denote the number densities of radio and wind electrons, respectively, and let r_{em} be the radius of the assumed spherical region within which the electrons are assumed to be distributed uniformly. Following the example of the Crab Nebula, we shall assume that the total energies contained in the radio and wind electrons, $E_e^r = \frac{4}{3}\pi r_{\text{em}}^3 m_e c^2 \int \gamma \frac{dn_e^r}{d\gamma} d\gamma$ and $E_e^w = \frac{4}{3}\pi r_{\text{em}}^3 m_e c^2 \int \gamma \frac{dn_e^w}{d\gamma} d\gamma$, respectively, are com-

parable and roughly equal ($\sim \text{few} \times 10^{48}$ erg) [156, 55]. This allows us to relating the normalization constants A_e^r and A_e^w appearing in equations (5.4) and (5.5), respectively, to each other and to the total energy content of the electrons, $E_e = E_e^r + E_e^w$, which, for a given set of the electron parameters,

$$\{\mathcal{P}\} \equiv \{\alpha_r, \gamma_{\min}^r, \gamma_{\max}^r, \beta, \alpha_w, \alpha'_w, \gamma_{\min}^w, \gamma_{\max}^w, \gamma_b\}, \quad (5.6)$$

can, therefore, be expressed as

$$E_e = \frac{4}{3} \pi r_{\text{em}}^3 A_e^r m_e c^2 \mathcal{F}(\{\mathcal{P}\}), \quad (5.7)$$

where \mathcal{F} is a calculable function of the set of parameters $\{\mathcal{P}\}$, the exact form of which need not concern us for the purpose of the discussions that follow.

Now, the energy spectrum of synchrotron photons produced by an electron of energy $\gamma m_e c^2$ with a pitch angle θ in a magnetic field B can be written as [61]

$$\mathcal{L}_\nu^{\text{Sy}} \equiv \left(\frac{d\mathcal{E}}{d\nu dt} \right)_{\text{Sy}} = \frac{\sqrt{3} e^3 B \sin \theta}{m_e c^2} \frac{\nu}{\nu_c} \int_{\nu/\nu_c}^{\infty} K_{5/3}(x) dx, \quad (5.8)$$

where e is the electron charge,

$$\nu_c = \frac{3e\gamma^2}{4\pi m_e c} B \sin \theta, \quad (5.9)$$

is the characteristic frequency of the emitted synchrotron radiation, and $K_{5/3}(x)$ is the modified Bessel function of fractional order 5/3. In our calculations described below, we shall average over the electron pitch angle and adopt a value of $\sin \theta = \sqrt{2/3}$ [55].

The number density, n_ν^{sy} , of synchrotron photons produced per unit frequency at frequency ν by all the electrons in the (assumed constant) magnetic field B in the spherical volume

of radius r_{em} within the nebula can be expressed as

$$n_{\nu}^{\text{sy}} = \frac{1}{c h \nu} A_e^r g_{\text{sy}}(\nu, B, \{\mathcal{P}\}), \quad (5.10)$$

where $g_{\text{sy}}(\nu, B, \{\mathcal{P}\})$ is a calculable function obtained by folding the electron spectra given in equations (5.4) and (5.5) with the synchrotron photon spectrum given by equation (5.8).

Similarly, the energy spectrum of photons produced by an electron of energy $\gamma m_e c^2$ due to IC scattering off a background of soft photons is given by [61]

$$\mathcal{L}_{\nu}^{\text{IC}} \equiv \left(\frac{d\mathcal{E}}{d\nu dt} \right)_{\text{IC}} = \frac{3}{4} \frac{\sigma_T c}{\gamma^2} h^2 \nu \int_{h\nu/(4\gamma^2)}^{h\nu} d\epsilon \frac{n_b(\epsilon)}{\epsilon} f_{\text{IC}}(\epsilon, \nu, \gamma), \quad (5.11)$$

where σ_T is the Thomson cross section, $h\nu$ is the photon energy after scattering, $n_b(\epsilon) d\epsilon$ is the number density of the background soft photons between energy ϵ and $\epsilon + d\epsilon$, and

$$\begin{aligned} f_{\text{IC}}(\epsilon, \nu, \gamma) &= 2q \ln q + (1 + 2q)(1 - q) + \frac{1}{2} \\ &\times \frac{[4\epsilon\gamma q / (m_e c^2)]^2}{1 + 4\epsilon\gamma q / (m_e c^2)} (1 - q), \end{aligned}$$

with

$$q = \frac{h\nu}{4\epsilon\gamma^2 [1 - h\nu / (\gamma m_e c^2)]}.$$

Let n_{ν}^{IC} denote the number density of high energy photons produced through IC process per unit frequency at frequency ν by all the electrons in the spherical volume of radius r_{em} within the nebula. Within the context of the synchrotron self-compton scenario that we consider here, we can assume that the dominant target photons for the IC interaction of the high energy electrons that produce the TeV emission are the synchrotron photons produced by the electrons themselves, although the CMB and IR photons are additional

targets.¹ Thus, with n_b replaced by n_ν^{sy} in equation (5.11), and noting that $n_\nu^{\text{sy}} \propto A_e^r$, we see that $n_\nu^{\text{IC}} \propto (A_e^r)^2$, which gives the expression

$$n_\nu^{\text{IC}} = \frac{1}{c h \nu} (A_e^r)^2 g_{\text{IC}}(\nu, B, \{\mathcal{P}\}), \quad (5.12)$$

where $g_{\text{IC}}(\nu, B, \{\mathcal{P}\})$ is another calculable function obtained by folding the the electron spectra given in equations (5.4) and (5.5) with the IC photon spectrum given by equation (5.11).

Thus, for the source at a distance D , the synchrotron radiation flux (energy/area/time/frequency) at frequency ν at earth can be written as

$$F_\nu^{\text{sy}} = \frac{1}{4\pi D^2} 4\pi r_{\text{em}}^2 n_\nu^{\text{sy}} c h \nu = \left(\frac{r_{\text{em}}}{D}\right)^2 A_e^r g_{\text{sy}}(\nu, B, \{\mathcal{P}\}), \quad (5.13)$$

while the IC photon flux is

$$F_\nu^{\text{IC}} = \left(\frac{r_{\text{em}}}{D}\right)^2 (A_e^r)^2 g_{\text{IC}}(\nu, B, \{\mathcal{P}\}). \quad (5.14)$$

For a suitable choice of the magnetic field B and the parameter set $\{\mathcal{P}\}$, requiring that we be able to explain the observed TeV flux from MGRO J2019+37 at some energy, say, 10 TeV, by the IC flux (5.14), we get

$$A_e^r = \left(F_{10 \text{ TeV}}^{\text{MGRO}}\right)^{1/2} g_{\text{IC}}^{-1/2}(h\nu = 10 \text{ TeV}, B, \{\mathcal{P}\}) \frac{D}{r_{\text{em}}}, \quad (5.15)$$

where $F_{10 \text{ TeV}}^{\text{MGRO}}$ is the observed flux from MGRO J2019+37 at 10 TeV. But, at the same time, we must ensure that, for the same value of B and the parameter set $\{\mathcal{P}\}$, the synchrotron flux given by equation (5.13) at $\nu = 610 \text{ MHz}$ not exceed the radio flux upper limit given by GMRT [11], $F_{610 \text{ MHz}}^{\text{GMRT}}$, from the region around the observed position of

¹In our full numerical calculations and results we include the CMB and IR photons in addition to the synchrotron photons.

MGRO J2019+37. This gives the condition

$$\left(\frac{r_{\text{em}}}{D}\right)^2 \leq F_{610\text{ MHz}}^{\text{GMRT}} (A_e^r)^{-1} g_{\text{sy}}^{-1}(\nu = 610\text{ MHz}, B, \{\mathcal{P}\}),$$

which, upon substituting for A_e^r from equation (5.15) above, gives,

$$\begin{aligned} \left(\frac{r_{\text{em}}}{D}\right)_{\text{GMRT}} &\leq F_{610\text{ MHz}}^{\text{GMRT}} \left(F_{10\text{ TeV}}^{\text{MGRO}}\right)^{-1/2} g_{\text{sy}}^{-1}(\nu = 610\text{ MHz}, B, \{\mathcal{P}\}) \\ &\times g_{\text{IC}}^{1/2}(h\nu = 10\text{ TeV}, B, \{\mathcal{P}\}). \end{aligned} \quad (5.16)$$

In addition, we must ensure that for the same values of the parameter set $\{\mathcal{P}\}$ and magnetic field B that account for the observed TeV flux, the predicted synchrotron flux given by equation (5.13) in the X-ray region at energy $\sim 10\text{ keV}$ not exceed the X-ray flux from the region (within the positional uncertainty) of MGRO J2019+37 reported by SWIFT/XRT observation [148], $F_{10\text{ keV}}^{\text{SWIFT/XRT}}$. This gives

$$\begin{aligned} \left(\frac{r_{\text{em}}}{D}\right)_{\text{SWIFT/XRT}} &\leq F_{10\text{ keV}}^{\text{SWIFT/XRT}} \left(F_{10\text{ TeV}}^{\text{MGRO}}\right)^{-1/2} g_{\text{sy}}^{-1}(h\nu = 10\text{ keV}, B, \{\mathcal{P}\}) \\ &\times g_{\text{IC}}^{1/2}(h\nu = 10\text{ TeV}, B, \{\mathcal{P}\}). \end{aligned} \quad (5.17)$$

Thus, within the context of the PWN scenario of origin of the observed TeV emission from MGRO J2019+37, there is an upper limit to the size r_{em} of the emission region of the PWN for a given distance D to the source and a chosen set of the electron parameters $\{\mathcal{P}\}$ and magnetic field B that yield the observed TeV flux of MGRO J2019+37. This upper limit, $r_{\text{em,max}}$, is given by the lower of the right hand sides of equations (5.16) and (5.17).

The distance D to MGRO J2019+37 is not precisely known. The radio and GeV pulsar PSR J2021+3651, with its associated pulsar wind nebula PWN G75.2+0.1 [13, 14, 15, 12], that has been suggested to be associated with MGRO J2019+37, is inferred to be at a

distance of 3–4 kpc [158]. The constraint on $r_{\text{em,max}}$ depends on the chosen distance of the source. Below, in our estimates of $r_{\text{em,max}}$ we allow a source distance range of 3 to 10 kpc.

For a given source distance D , one can choose the values of the electron parameters $\{\mathcal{P}\}$ and magnetic field B such that the predicted fluxes in the radio and X-ray regions saturate the GMRT and SWIFT/XRT upper limits, respectively, while explaining the observed TeV flux. Examples of such multiwavelength photon spectra, which we obtain by performing a scan of the relevant parameters $\{\mathcal{P}\}$ for three chosen values of the magnetic field B , are shown in Figure 5.8 for a choice of the source distance $D = 3$ kpc. We have included the interstellar radiation field (ISRF) from Ref. [159] and the cosmic microwave background (CMB) in addition to the synchrotron photon field generated by the electrons themselves in obtaining the IC portion of the multiwavelength photon spectra (from X-ray to TeV energies) shown in Figure 5.8. The values of the electron parameters used in obtaining the curves in Figure 5.8 for the three chosen magnetic fields are listed in Table 5.4 where we also list the corresponding upper limits on the radius of the emission region, $r_{\text{em,max}}$, and the total energy contained in electrons, E_e , in units of $E_{e,\text{Crab}} = 5.3 \times 10^{48}$ erg [55]. As seen from Table 5.4 these upper limits on r_{em} are three or more orders of magnitude lower than the typical values of the characteristic size of the emission region (~ 1 pc) invoked in the PWN scenario of TeV emission of the Crab nebula, for example, Ref. [157, 55].

Table 5.4: Values of the electron parameters used in obtaining the curves shown in Figure 5.8 for the three chosen values of the magnetic field. The corresponding upper limits on the radius of the emission region, $r_{\text{em,max}}$, and the total energy contained in electrons, E_e , in units of $E_{e,\text{Crab}} = 5.3 \times 10^{48}$ erg, are also given. The source distance is taken as $D = 3$ kpc.

Magnetic field B (μG)	Electron parameters									$r_{\text{em,max}}$ (pc)	$E_e / E_{e,\text{Crab}}$
	α_r	γ'_{min}	γ'_{max}	β	α_w	α'_w	γ_{min}^w	γ_{max}^w	γ_b		
0.3	1.37	1	2.93×10^5	2.82	2.1	2.6	4×10^5	2×10^9	2×10^8	7.0×10^{-4}	1.8×10^{-2}
3.0	1.67	1	3×10^5	2.82	2.2	2.7	4×10^5	7×10^8	2×10^8	6.8×10^{-5}	4.6×10^{-4}
125	1.75	1	1.5×10^5	2.82	2.3	2.8	2×10^5	1.0×10^8	8×10^7	2.2×10^{-6}	1.5×10^{-6}

A heuristic estimate of the value of $r_{\text{em,max}}$ for MGRO J2019+37 can be obtained just

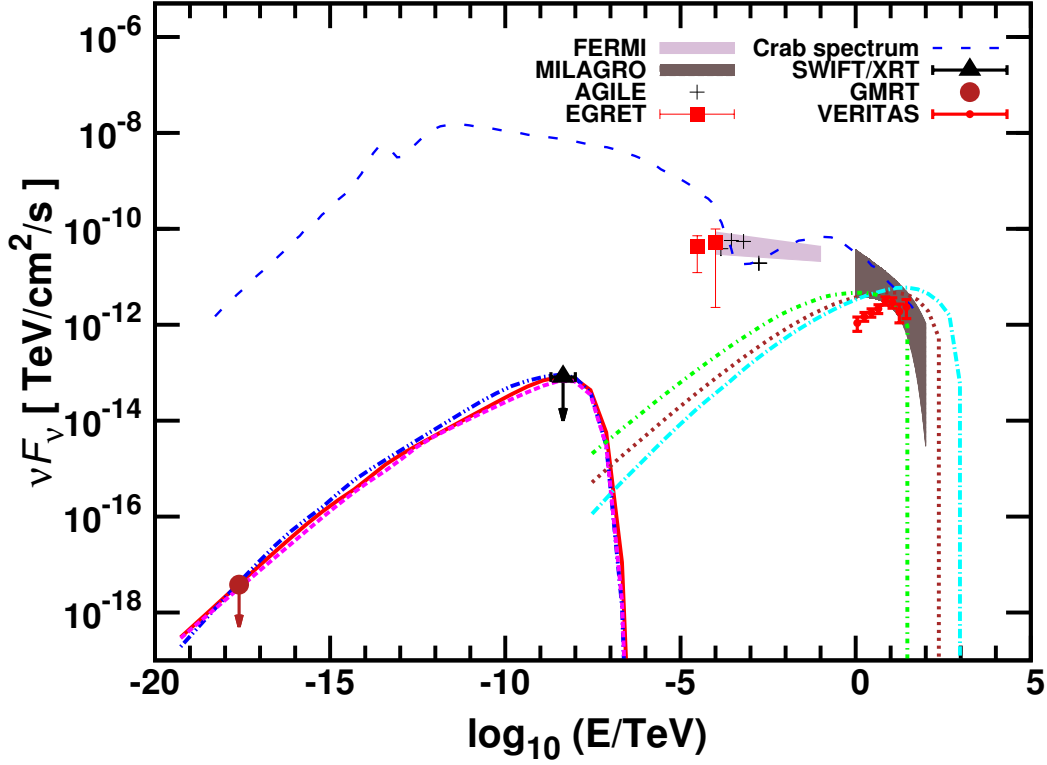


Figure 5.8: The constrained spectral energy distribution (SED) of MGRO J2019+37 from radio to TeV region in the PWN scenario. The solid, dash-double-dotted and dashed curves from radio to X-ray energies are the synchrotron spectra for magnetic fields of $B = 3$ and 0.3 and $125 \mu\text{G}$, respectively, and the dotted, long-dash-dotted and dot-dashed curves from the X-ray to TeV energies are the corresponding inverse Compton (IC) spectra for the three magnetic fields, respectively. The values of the various parameters of the electron spectra [see equations (5.4) and (5.5)] corresponding to the three magnetic fields are listed in Table 5.4. The distance to the source is taken to be $D = 3 \text{ kpc}$. Multiwavelength observational data and flux constraints from observations in the region around MGRO J2019+37 including the radio upper limit given by GMRT [11], X-ray flux upper limit from SWIFT/XRT observations [148], GeV observations by FERMI [12], EGRET [42] and AGILE [15] and TeV observations by Milagro [8, 9, 10] and VERITAS [119] are shown. In addition, the SED of the Crab nebula (at a distance of $\sim 2 \text{ kpc}$) from radio to TeV energies (taken from Ref. [55]) is also shown for comparison.

by comparing the constrained spectral energy distribution (SED) of MGRO J2019+37 shown in Figure 5.8 with the SED of the Crab nebula also shown in the same Figure. Note that Crab emits comparable amount of energy at TeV and radio wavelengths, with $\nu F_\nu^{\text{Crab}}(h\nu = 10 \text{ TeV}) \simeq 1.5 \times 10^{-11} \text{ erg cm}^{-2} \text{ s}^{-1}$ and $\nu F_\nu^{\text{Crab}}(\nu = 610 \text{ MHz}) \simeq 0.74 \times 10^{-11} \text{ erg cm}^{-2} \text{ s}^{-1}$ at 10 TeV and 610 MHz , respectively, for example. In con-

trast, for MGRO J2019+37, while the energy emitted at TeV energies is comparable with that for Crab, with $\nu F_{\nu}^{\text{MGRO}}(h\nu = 10 \text{ TeV}) \simeq 1.1 \times 10^{-11} \text{ erg cm}^{-2} \text{ s}^{-1}$, the GMRT upper limit restricts the possible flux of MGRO J2019+37 in the radio region to $\nu F_{\nu}^{\text{MGRO}}(\nu = 610 \text{ MHz}) \simeq 6.1 \times 10^{-18} \text{ erg cm}^{-2} \text{ s}^{-1}$, about 6 orders of magnitude less than the corresponding quantity for Crab at that frequency. Let us define the ratio

$$\xi \equiv \frac{\nu F_{\nu}^{\text{IC}}(h\nu = 10 \text{ TeV})}{\nu F_{\nu}^{\text{sy}}(\nu = 610 \text{ MHz})}, \quad (5.18)$$

where F_{ν}^{sy} and F_{ν}^{IC} are given by equations (5.13) and (5.14), respectively. Let us demand that the measured TeV flux of both Crab and MGRO J2019+37 be explained by the synchrotron self-compton (i.e., IC) process within the PWN scenario. Then, for a given set of the electrons' spectral parameters $\{\mathcal{P}\}$ and magnetic field B , assumed same for the moment for both Crab and MGRO J2019+37, it is easy to see, using equations (5.18), (5.13), (5.14) and (5.15), that

$$\left(\frac{r_{\text{em}}}{D}\right)_{\text{Crab}} \xi_{\text{Crab}} = \left(F_{10 \text{ TeV}}^{\text{Crab}}/F_{10 \text{ TeV}}^{\text{MGRO}}\right)^{1/2} \times \left(\frac{r_{\text{em}}}{D}\right)_{\text{MGRO}} \xi_{\text{MGRO}}, \quad (5.19)$$

where the sub(super)scripts Crab and MGRO refer to quantities relevant to Crab and MGRO J2019+37, respectively.

Now, from the above discussions of comparison of the measured SED of Crab and the constrained SED of MGRO (see Figure 5.8), we see that $\xi_{\text{Crab}} \simeq 2$ and $F_{10 \text{ TeV}}^{\text{Crab}}/F_{10 \text{ TeV}}^{\text{MGRO}} \simeq 1$, whereas $\xi_{\text{MGRO}} \geq 1.8 \times 10^6$. Using these estimates in equation (5.19) we immediately get the constraint

$$\left(\frac{r_{\text{em}}}{D}\right)_{\text{MGRO}} \leq 1.1 \times 10^{-6} \times \left(\frac{r_{\text{em}}}{D}\right)_{\text{Crab}}, \quad (5.20)$$

which, upon using typical numbers for the relevant quantities pertaining to Crab and

MGRO J2019+37, yields

$$(r_{\text{em}})_{\text{MGRO}} \leq 1.7 \times 10^{-6} \text{ pc} \left(\frac{D}{3 \text{ kpc}} \right)_{\text{MGRO}} \left(\frac{r_{\text{em}}}{1 \text{ pc}} \right)_{\text{Crab}} \left(\frac{2 \text{ kpc}}{D} \right)_{\text{Crab}}. \quad (5.21)$$

It is thus seen that if MGRO J2019+37 is like a “standard” PWN with the spectral parameters of its electron population and the magnetic field similar to those of Crab nebula, then within the context of the synchrotron self-compton scenario of production of TeV photons, the MGRO J2019+37 has to be a significantly more compact source than a standard PWN like the Crab. Of course, the electron parameters and the magnetic field inside MGRO J2019+37 have no reason to be exactly the same as those in Crab. However, this does not alter the above general inference, the main reason for which is the strong constraints on the radio and X-ray fluxes from MGRO J2019+37 imposed by the GMRT and the SWIFT/XRT observations discussed above in relation to those of Crab at these energies (see Figure 5.8).

Note that the constraint on r_{em} of MGRO J2019+37 given by equation (5.21), derived analytically under the assumption that the values of the electrons’ spectral parameters $\{\mathcal{P}\}$ and the magnetic field are same as those of Crab, is fairly close to the value $r_{\text{em,max}} \simeq 2.2 \times 10^{-6} \text{ pc}$ displayed in Table 5.4 for the case of magnetic field $B = 125 \mu\text{G}$ typically invoked for the Crab [55]. The difference may be attributed to the different values of the electrons’ spectral parameters adopted for MGRO J2019+37 in comparison with those for the Crab.

To see the dependence of $r_{\text{em,max}}$ on the electron parameters $\{\mathcal{P}\}$ and magnetic field B , we show in Figure 5.9 the variations of $r_{\text{em,max}}$ given by equations (5.16) and (5.17) with some of the relevant parameters of the electrons with respect to which the variations of $r_{\text{em,max}}$ are most sensitive. In Figure 5.9, for illustration, the electron parameters are individually varied about their respective values shown in Table 5.4 for the case of $B = 0.3 \mu\text{G}$ and source distance $D = 3 \text{ kpc}$. The crossing points of the two curves in each panel in Figure

5.9 correspond to the parameter values for which the GMRT and the SWIFT/XRT bounds are simultaneously fulfilled (see Figure 5.8). It is seen that the requirement of simultaneously respecting the two constraints given by equations (5.16) and (5.17) restricts $r_{\text{em,max}}$ to values less than a few $\times 10^{-4}$ pc for all reasonable values of the magnetic field within the nebula.

As seen from Figure 5.9, the most significant variation of $r_{\text{em,max}}$ occurs not with respect to the electron parameters, but rather with respect to the magnetic field B . In general, $r_{\text{em,max}}$ is larger for smaller magnetic fields. In Figure 5.10 we show the variations of the lower of the two $r_{\text{em,max}}$ values given by equations (5.16) and (5.17) and the corresponding variation of the total electron energy (E_e) with magnetic field B for various source distance D , with the values of the electron parameters kept fixed at those given in Table 5.4 for the case of $B = 0.3 \mu\text{G}$. As expected, and as seen from the right panel of Figure 5.10, the total energy in electrons required to produce the observed TeV flux is larger for smaller magnetic fields as well as for larger distance to the source. However, for too small values ($\sim 10^{-2} \mu\text{G}$) of magnetic field, the density of synchrotron photons of the requisite energy becomes so low that the synchrotron self-compton (IC) mechanism of explaining the TeV flux becomes inefficient unless the total energy content of electrons is made several orders of magnitude larger than that for the Crab.

To explain the observed data at TeV energies we have only considered IC emission process as shown in Figure 5.8. In principle, bremsstrahlung process can also contribute to gamma-rays at GeV and TeV energies. However, to explain the GeV–TeV data with bremsstrahlung process alone, it requires unreasonably high values ($> 10^3 \text{ cm}^{-3}$) of ambient matter density.

In the above discussions we have made the simplifying assumption of the electrons — and consequently the photons generated by them — being uniformly distributed within a spherical “emission region” of radius r_{em} within the nebula. More realistically, the radius

r_{em} may be considered as a kind of characteristic length scale of a possible non-uniform spatial distribution of the electrons and/or the photons generated by them [55, 157]. Also, the magnetic field inside the nebula is likely to be not spatially constant, but rather varying with a characteristic length scale similar to r_{em} . These details, however, are unlikely to change the general conclusion regarding the extreme compactness of the emission region of MGRO J2019+37 relative to a Crab nebula-like PWN within the general PWN scenario of origin of the observed TeV emission from the MGRO J2019+37.

5.2.3 Summary and conclusions

To summarize, here we have considered a PWN scenario of the origin of the observed TeV gamma ray emission from MGRO J2019+37. We find that, while no lower energy counterparts of this object have yet been identified, the upper limits on possible radio and X-ray emissions from sources suggested to be associated with MGRO J2019+37 already provide rather strong constraints on the size of the emission region of the nebula, with the characteristic radius of the emission region being restricted to $O(10^{-3})$ pc, about three orders of magnitude less than that of the Crab nebula. This conclusion is in fact fairly general and is reasonably independent of the details of the parameters describing the spectrum of the electrons responsible for the emission and the magnetic field within the nebula as long as the total energy content of the electrons is not too large ($\sim 10^{49}$ ergs) compared to that for the case of the Crab nebula. Thus, the TeV emission from the MGRO J2019+37 is difficult to explain within the context of the standard PWN scenario. The implied unusually compact size of the emission region of the source of MGRO J2019+37 in the PWN scenario also raises interesting issues concerning possible variability of the source on (sub)year time scales [118].

The parameters estimated for both Cas A and MGRO J2019+37 are optimized to fit the multi-wavelength observations. However, the physical plausibility of the values of these parameters can only be ascertained by detailed consideration of acceleration and loss

mechanisms which are subjects of future investigations.

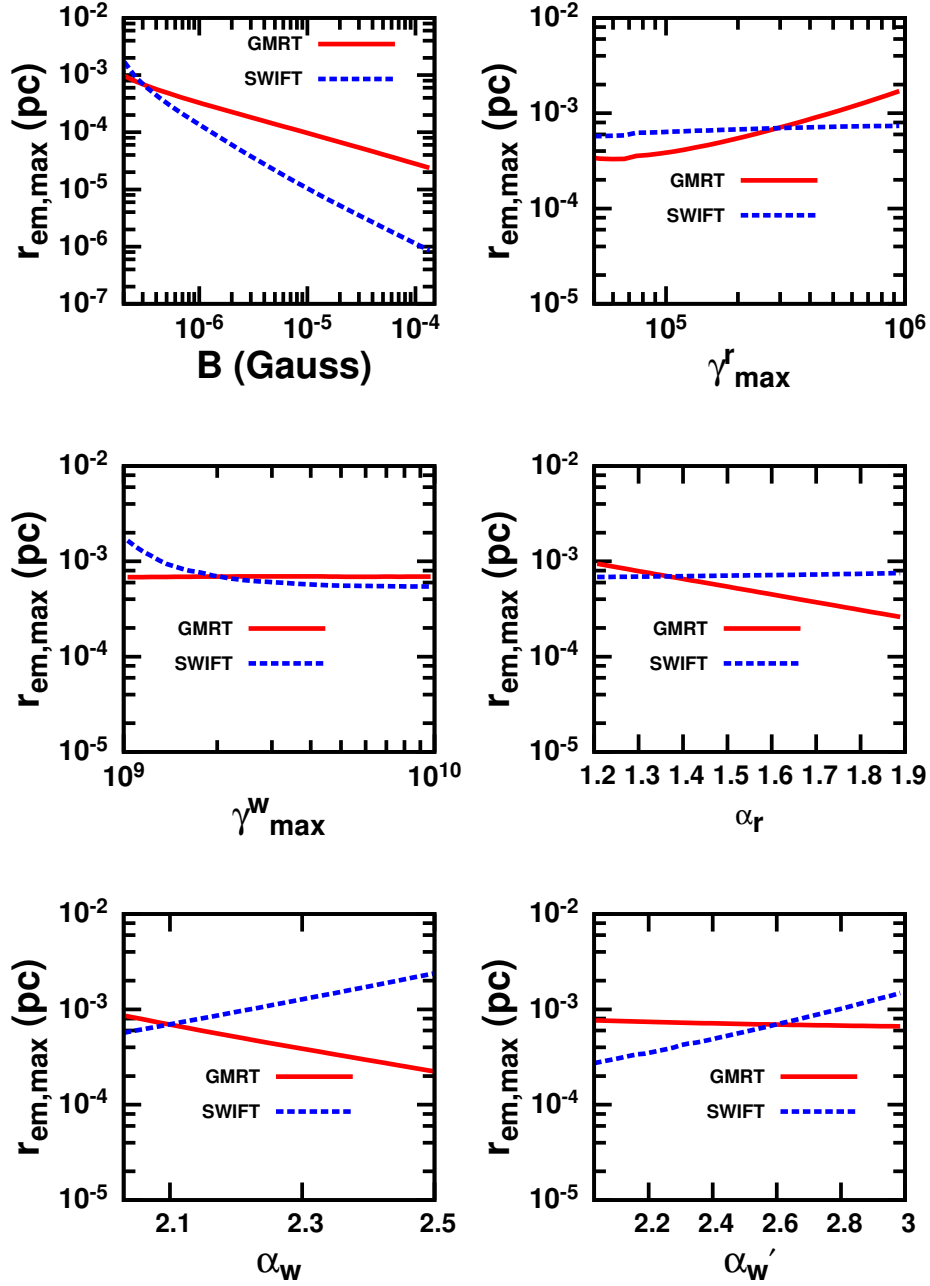


Figure 5.9: Variation of $r_{\text{em,max}}$ with magnetic field and various electron parameters about their respective values for the case $B = 0.3 \mu\text{G}$ shown in Table 5.4. The source distance is $D = 3 \text{ kpc}$. The crossing points of the two curves in each panel correspond to the parameter values for which the GMRT and the SWIFT/XRT bounds are simultaneously fulfilled (see Figure 5.8).

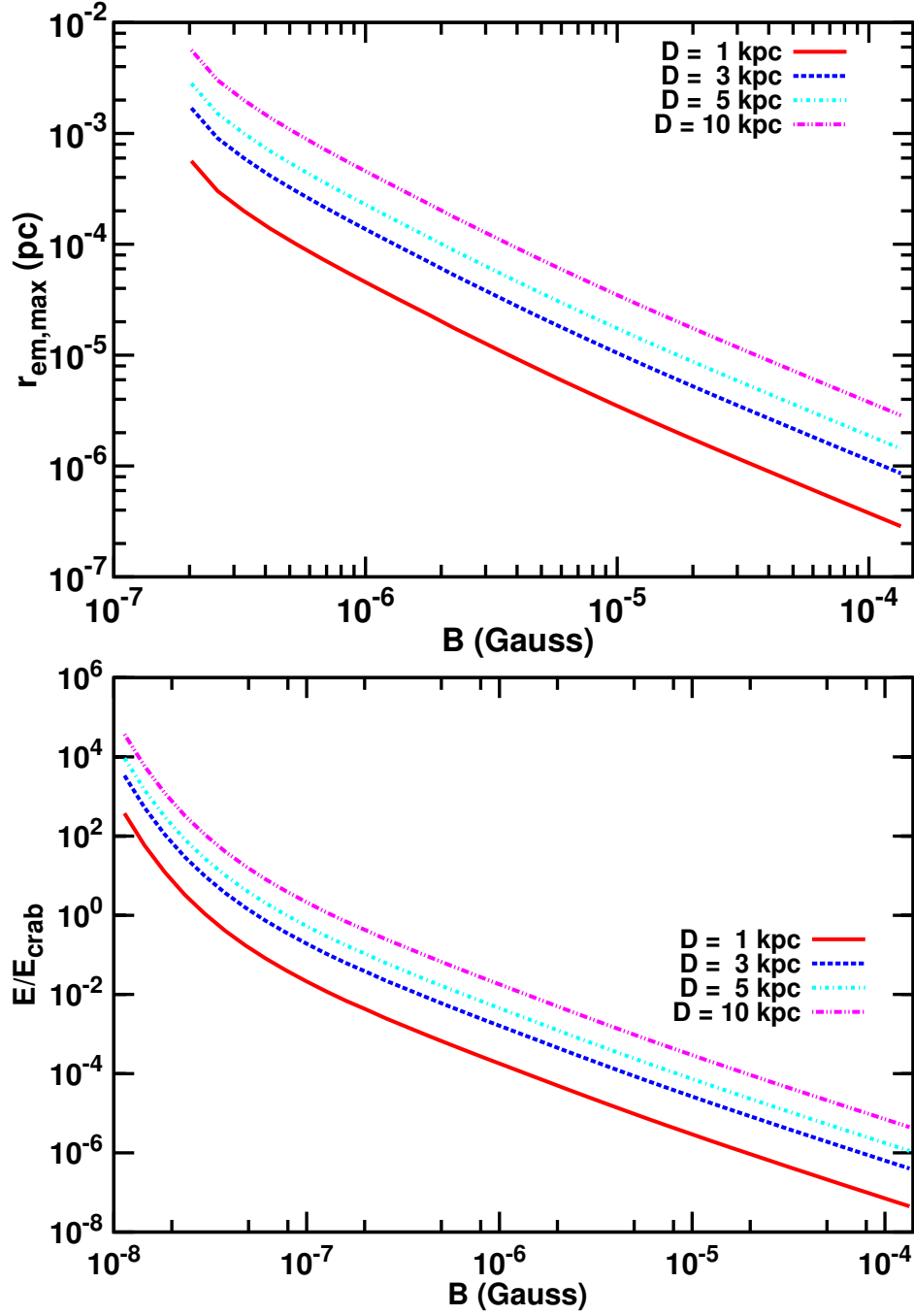


Figure 5.10: Variation of $r_{\text{em,max}}$ and the corresponding total energy in electrons (E_e , in units of $E_{e,\text{Crab}} = 5.3 \times 10^{48}$ erg) with magnetic field (B), for various source distance D . The values of the electron parameters are kept fixed at those given in Table 5.4 for the case of $B = 0.3 \mu\text{G}$.

Chapter 6

Summary and future prospects

6.1 Summary

This thesis is broadly divided into two parts. The first one is the Monte Carlo simulations, observations and analyses of data pertaining to High Altitude GAMMA Ray (HAGAR) telescope system, and the second one is the multi-wavelength modelling of two Galactic TeV gamma-ray sources.

Monte Carlo studies show that the energy threshold of HAGAR is about 210 GeV which is a factor of 4 lower than the similar type of setup at an altitude of 1075m amsl. Thus, by installing the HAGAR system at high altitude (4300 amsl) it was possible to bring down the energy threshold by a factor of 4 without significantly increasing the mirror area. We have also estimated that this telescope system is able to detect Crab like sources in 17 hours of observations with the significance of 5σ without further rejecting cosmic ray events. We have compared space angle distributions and variation of trigger rate with zenith angle obtained from simulations with the observed results and found that they are in good agreement indicating that the HAGAR telescope system is well understood and accurately modelled.

Among the several Galactic and extra-galactic gamma-ray sources observed so far with the HAGAR system, analyses and corresponding results of three Galactic sources are described in this thesis. Analysis of the Crab nebula data shows that the estimated Crab nebula fluxes for NTT greater than or equal to 5-fold and higher folds are consistent with the simulated results as well as with the results given by other experiments. In the case of the binary system LSI 61+303, we found that the source shows significant fluxes in the orbital phases of 0.0–0.1 and 0.7–0.8 during the period 2011–2012. The analysis results of the extended source MGRO J2019+37 showed that the estimated fluxes for different trigger conditions are higher than the flux estimated by VERITAS and Milagro indicating that the present HAGAR data analysis procedure is not sensitive to extended source observation.

In the case of multi-wavelength modelling of Galactic shell-type SNR Cassiopeia A, we found that the S-region of the shell is dominant among all other regions of the shell in producing gamma rays through IC process. The second best-fit IC prediction with the TeV data is from the SE and SW and then the NE region. The observed X-ray fluxes from different regions of the shell are attributed to different magnetic fields, which indicate amplification of magnetic fields at different regions of the shell. In addition, we found that the leptonic model alone is unable to explain the observed GeV–TeV fluxes simultaneously for any regions of the shell. However, the GeV and TeV gamma-ray data fit reasonably well to the hadronic model, which is independent of the selected regions on the shell. We also found that lepto-hadronic model provides a better fit to the GeV–TeV data.

The estimated total energy of high energy particles are about 2% of the total energy typically released during a supernova explosion. The low conversion efficiency of cosmic rays combined with amplification of magnetic fields suggests that the cosmic ray streaming energy may not be sufficient to be transferred to the magnetic fields that result from magnetic amplification. Hence, the magnetic field amplification in the down-stream regions

of shocks due to presence of turbulence could be a favourable scenario in this particular remnant.

For multi-wavelength modelling of the Galactic extended bright TeV gamma-ray source MGRO J2019+37, we have considered a PWN scenario to understand the origin of the observed TeV gamma ray emission from MGRO J2019+37. No confirmed counterparts of this source at lower energies are known. However, several possible associations with other observed sources have been suggested. We find that the upper limits on possible radio and X-ray emission from sources suggested to be associated with MGRO J2019+37 already provide rather strong constraints on the size of the emission region of the nebula, with the characteristic radius of the emission region being restricted to $O(10^{-3})$ pc. This is about four orders of magnitude less than that of the Crab nebula. We also find that this conclusion is in fact fairly general and is reasonably independent of the details of the parameters describing the spectrum of the electrons responsible for the emission and the magnetic field within the nebula as long as the total energy content of the electrons is not too large ($\sim 10^{49}$ ergs) compared to that for the case of the Crab nebula. Thus, the TeV emission from the MGRO J2019+37 is difficult to explain within the context of a standard PWN scenario.

Further improvements

The sensitivity of the HAGAR telescope system can be increased by improving the data analysis technique. HAGAR data analysis procedure needs to be improved to get better gamma-hadron separation. The pulse shape of each event recorded by the Flash-ADC can be used to discriminate between gamma-ray and cosmic ray showers, and this needs further detailed simulation study. Moreover, present HAGAR data analysis method is appropriate for point sources with gamma rays coming from source in specific direction and cosmic rays coming isotropically over larger angle range. To estimate the signal we compare space angle distribution of ON-OFF pairs. To normalize the backgrounds

of ON-source and OFF-source runs we consider tail regions of space angle distributions assuming that no gamma-ray events are present at the higher space angle. This is no longer true for analysis of extended sources. In that case, we cannot normalize the two backgrounds of an ON and an OFF source run considering the space angle distributions. The possible solution for this is to explore gamma-hadron separation parameters based on density fluctuations, pulse shape etc.

6.2 Future directions

Origin, presence of different spectral features and mass composition of cosmic rays are most important issues of cosmic rays physics, and it still lacks a coherent theory to understand all these issues of cosmic ray physics. However, they can be investigated through observations of Galactic sources of CRs. Supernova remnants (SNRs) are believed to be one of the main sources of galactic CRs. Pulsar wind nebulae (PWNe) are another class of objects which are considered to be sources which can accelerate CRs (particularly electrons) to very high energies. The recent discoveries of more than hundred such astrophysical sources in high energy gamma rays with both ground based and satellite based gamma-ray detectors enriched the field of high energy gamma-ray astronomy and provided some significant signatures of the origin of galactic CRs. The present generation of gamma-ray instruments cannot provide the exact location of gamma-ray emission region in a SNR or a PWN, more precisely, the morphology of the source is not known due to the limited instrumental sensitivity and angular resolution of the existing gamma-ray telescopes. Therefore, requirements for more sensitive instruments are highly desired. The next generation gamma-ray instrument, namely Cherenkov Telescope Array (CTA) (see Figure 6.1), is expected to be a much superior experiment to explore our non-thermal universe providing more detailed information of many astrophysical objects such as SNRs,

pulsars, PWNe, binary systems, active galactic nuclei, etc. With wider energy coverage ($\sim 30 \text{ GeV} - 300 \text{ TeV}$), better angular resolution ($\sim 2'$ at TeV energies), superior energy resolution ($\text{RMS} < 10\%$ at TeV energies), and a wider field of view ($\sim 6^\circ - 8^\circ$), CTA is expected to provide about 10 times better sensitivity than the present generation of imaging atmospheric Cherenkov telescopes (e.g. MAGIC, HESS, VERITAS).

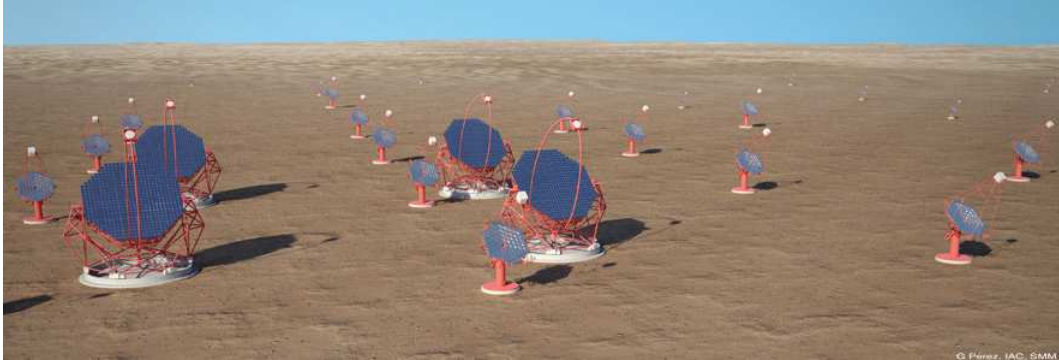


Figure 6.1: An artist's impression of CTA array. This figure is taken from Ref. [160]

The non-thermal emission from numerous SNRs and PWNe provide evidence for acceleration of cosmic particles to extremely high energies. Analysis of a large sample of SNRs and PWNe can be used to understand all these issues related to CR physics. CTA can potentially observe several hundreds of CR accelerators. Therefore, it is important to investigate the potential of CTA through Monte Carlo simulations to explore the morphology of the sources and the substructures in the sources with its improved sensitivity. In addition, multi-wavelength data can be used to study the SNRs and PWNe to get much deeper insight into the CR acceleration, morphology, sites of gamma-ray emission and emission mechanisms (leptonic and hadronic) in these sources as discussed in this thesis.

Bibliography

- [1] W. Galbraith and J. V. Jelley, *Nature* **171**, 349 (1953).
- [2] P. Majumdar *et al.*, *Astroparticle Physics* **18**, 333 (2003).
- [3] D. Bose *et al.*, *Astrophysics and Space Science* **309**, 111 (2007).
- [4] B. B. Singh *et al.*, *Astroparticle Physics* **32**, 120 (2009).
- [5] J. Knapp and D. Heck, *Extensive Air Shower Simulation with CORSIKA: A User's Guide*, Version 6.7 (2007).
- [6] D. Heck, J. Knapp, J. N. Capdevielle, G. Schatz, and T. Thouw, *Forschungszentrum Karlsruhe Report FZKA*, 6019 (1998).
- [7] L. Saha *et al.*, *Astroparticle Physics* **42**, 33 (2013).
- [8] A. A. Abdo *et al.*, *ApJL* **658**, L33 (2007).
- [9] A. A. Abdo *et al.*, *ApJL* **664**, L91 (2007).
- [10] A. A. Abdo *et al.*, *ApJ* **753**, 159 (2012).
- [11] J. M. Paredes *et al.*, *A&A* **507**, 241 (2009).
- [12] A. A. Abdo *et al.*, *ApJS* **183**, 46 (2009).
- [13] M. S. E. Roberts *et al.*, *ApJL* **577**, L19 (2002).
- [14] J. W. T. Hessels *et al.*, *ApJ* **612**, 389 (2004).

-
- [15] J. P. Halpern *et al.*, *ApJL* **688**, L33 (2008).
 - [16] J. Baars, R. Genzel, I. Pauliny-Toth, and A. Witzel, *A&A* **61**, 99 (1977).
 - [17] J. E. Reed, J. J. Hester, A. Fabian, and P. Winkler, *ApJ* **440**, 706 (1995).
 - [18] J. Smith *et al.*, *ApJ* **693**, 713 (2009).
 - [19] G. E. Allen *et al.*, *ApJL* **487**, L97 (1997).
 - [20] U. Hwang *et al.*, *ApJL* **615**, L117 (2004).
 - [21] J. Albert *et al.*, *A&A* **474**, 937 (2007).
 - [22] V. A. Acciari *et al.*, *ApJ* **714**, 163 (2010).
 - [23] A. A. Abdo *et al.*, *ApJ* **710**, L92 (2010).
 - [24] T. Ergin, L. Saha, P. Majumdar, M. Bozkurt, and E. Ercan, *ArXiv e-prints* (2013), 1308.0195.
 - [25] L. Saha, T. Ergin, P. Majumdar, M. Bozkurt, and E. Ercan, *A&A* **563**, A88 (2014).
 - [26] K. Koyama *et al.*, *Nature* **378**, 255 (1995).
 - [27] U. Hwang, A. Decourchelle, S. S. Holt, and R. Petre, *ApJ* **581**, 1101 (2002).
 - [28] M. Ackermann *et al.*, *Science* **339**, 807 (2013).
 - [29] D. Mazin *et al.*, *Astroparticle Physics* **43**, 241 (2013).
 - [30] F. Aharonian *et al.*, *Nature* **440**, 1018 (2006).
 - [31] D. Mazin and M. Raue, *A&A* **471**, 439 (2007).
 - [32] E. Waxman and J. N. Bahcall, *ApJ* **541**, 707 (2000).
 - [33] M. Lemoine and G. Pelletier, *MNRAS* **402**, 321 (2010).
 - [34] J. Ellis and N. E. Mavromatos, *Astroparticle Physics* **43**, 50 (2013).

-
- [35] R. Aloisio, P. Blasi, P. L. Ghia, and A. F. Grillo, *Phys.Rev.* **D62**, 053010 (2000).
- [36] P. Blackett, *Rep. Conf. Gassiot Comm. Phys. Soc.* **34** (1948).
- [37] P. Morrison, *Il Nuovo Cimento* **7**, 858 (1958).
- [38] G. Cocconi and P. Morrison, *Nature* **184**, 844 (1959).
- [39] A. Chudakov, V. Dadykin, V. Zatsepin, and N. Nesterova, A search for photons with energy 10^{13} ev from local sources of cosmic radiation, in *Proc. PN Lebedev Phys. Inst* Vol. 26, p. 118, 1964.
- [40] P. V. Ramana Murthy and A. W. Wolfendale, *Gamma-Ray Astronomy*, 2nd ed. (Cambridge University Press, Cambridge, 1993).
- [41] T. C. Weekes *et al.*, *ApJ* **342**, 379 (1989).
- [42] R. C. Hartman *et al.*, *ApJS* **123**, 79 (1999).
- [43] R. Mirzoyan, *Astroparticle Physics* **53**, 91 (2014).
- [44] B. Acharya, *Proceedings of 29th ICRC, Pune, India* **10**, 271 (2005).
- [45] R. Koul *et al.*, *Nucl.Instrum.Meth.* **A578**, 548 (2007).
- [46] D. Bose, PhD thesis, Tata Institute of Fundamental Research, Unpublished, 2007.
- [47] L. O. Drury, F. A. Aharonian, and H. J. Volk, *A&A* **287**, 959 (1994).
- [48] L. Drury, *Space Science Reviews* **36**, 57 (1983).
- [49] E. Fermi, *Phys. Rev.* **75**, 1169 (1949).
- [50] L. O. Drury, *Reports on Progress in Physics* **46**, 973 (1983).
- [51] R. Blandford and D. Eichler, *Phys.Rept.* **154**, 1 (1987).
- [52] M. S. Longair, *High Energy Astrophysics* (Cambridge: Cambridge University Press, 1981).

-
- [53] M. A. Malkov and L. O. Drury, Reports on Progress in Physics **64**, 429 (2001).
- [54] M. J. Rees and J. E. Gunn, MNRAS **167**, 1 (1974).
- [55] M. Meyer, D. Horns, and H.-S. Zechlin, A&A **523**, A2 (2010).
- [56] W. Bednarek and M. Bartosik, A&A **405**, 689 (2003).
- [57] A. M. Hillas *et al.*, ApJ **503**, 744 (1998).
- [58] S. Heinz and R. Sunyaev, A&A **390**, 751 (2002).
- [59] J. Albert *et al.*, Science **312**, 1771 (2006).
- [60] C. M. Urry and P. Padovani, Publ.Astron.Soc.Pac. **107**, 803 (1995).
- [61] G. R. Blumenthal and R. J. Gould, Reviews of Modern Physics **42**, 237 (1970).
- [62] F. Aharonian, *Very High Energy Cosmic Gamma Radiation: A crucial window on the extreme universe* (World Scientific, Singapore, 2004).
- [63] S. Kelner, F. A. Aharonian, and V. Bugayov, Phys.Rev. **D74**, 034018 (2006).
- [64] F. Aharonian, New Astronomy **5**, 377 (2000).
- [65] J. E. Baldwin, The Electromagnetic Spectrum of the Crab Nebula, in *The Crab Nebula*, edited by R. D. Davies and F. Graham-Smith, IAU Symposium Vol. 46, p. 22, 1971.
- [66] D. A. Green, R. J. Tuffs, and C. C. Popescu, MNRAS **355**, 1315 (2004).
- [67] T. Temim *et al.*, The Astronomical Journal **132**, 1610 (2006).
- [68] M. G. Kirsch *et al.*, Crab: the standard x-ray candle with all (modern) x-ray satellites, in *UV, X-Ray, and Gamma-Ray Space Instrumentation for Astronomy XIV*, edited by O. H. W. Siegmund, Society of Photo-Optical Instrumentation Engineers (SPIE) Conference Series Vol. 5898, pp. 22–33, 2005.

-
- [69] E. Jourdain and J. P. Roques, *ApJ* **704**, 17 (2009).
- [70] A. A. Abdo *et al.*, *ApJ* **708**, 1254 (2010).
- [71] J. Albert *et al.*, *ApJ* **674**, 1037 (2008).
- [72] F. Aharonian *et al.*, *A&A* **457**, 899 (2006).
- [73] P. A. Cherenkov, *Phys. Rev.* **52**, 378 (1937).
- [74] I. E. Tamm and I. M. Frank, *Dokl. Akad. Nauk SSSR* (1937).
- [75] J. V. Jelley, *CHERENKOV RADIATION and its applications* (PERGAMON PRESS, London, 1958).
- [76] M. V. Rao and S. Sinha, *Journal of Physics G* **14**, 811 (1988).
- [77] R. Ong, *Phys.Rept.* **305**, 93 (1998).
- [78] S. Oser, PhD thesis, University of Chicago, Unpublished, 2000.
- [79] M. Cawley and T. Weekes, *Experimental Astronomy* **6**, 7 (1995).
- [80] T. Weekes, *Phys.Rept.* **160**, 1 (1988).
- [81] F. I. Boley, *Reviews of Modern Physics* **36**, 792 (1964).
- [82] D. A. Hill, *Nature* **191**, 690 (1961).
- [83] A. M. Hillas, *Proceedings of 19th ICRC, La Jolla, USA* (1985).
- [84] A. M. Hillas, *Space Science Reviews* **75**, 17 (1996).
- [85] D. J. Fegan, *Journal of Physics G* **23**, 1013 (1997).
- [86] <http://www.mpi-hd.mpg.de/hfm/HESS/pages/about/telescopes/>
- [87] V. Chitnis *et al.*, *Proceedings of 31st ICRC, Łódź, Poland* (2009).
- [88] K. Gothe *et al.*, *Exper.Astron.* **35**, 489 (2013).

-
- [89] A. Shukla, PhD thesis, Pondicherry University, Unpublished, 2013.
- [90] K. Werner, Phys.Rept. **232**, 87 (1993).
- [91] H. Fesefeldt, Report Aachen PITHA **85** (1985).
- [92] W. R. Nelson and et al., SLAC-Report-265, Stanford Linear Accelerator Center (1985).
- [93] K. Bernlöhner, Astroparticle Physics **12**, 255 (2000).
- [94] J. R. Hörandel, Astroparticle Physics **19**, 193 (2003).
- [95] M. Ackermann *et al.*, Phys.Rev. **D82**, 092004 (2010).
- [96] F. Aharonian *et al.*, ApJ **539**, 317 (2000).
- [97] C. W. Allen, *Astrophysical Quantities*, 3rd ed. (Athlone Press, University of London, 1973).
- [98] S. Preuss, G. Hermann, W. Hofmann, and A. Kohnle, Nucl.Instrum.Meth. **A481**, 229 (2002).
- [99] http://www.astro.ucla.edu/veritas/Veritas-only/docs/sub_pro10/NSB.ps
- [100] B. Singh *et al.*, Astroparticle Physics **32**, 120 (2009).
- [101] R. J. Britto *et al.*, Status of the Himalayan Gamma-Ray Observatory (HIGRO) and observaton with HAGAR at very high energies, in *SF2A-2011: Proceedings of the Annual meeting of the French Society of Astronomy and Astrophysics*, edited by G. Alecian, K. Belkacem, R. Samadi, and D. Valls-Gabaud, pp. 539–543, 2011.
- [102] B. B. Singh *et al.*, Proceedings of 32nd ICRC, Beijing, China (2011).
- [103] V. Trimble, The Astronomical Journal **73**, 535 (1968).
- [104] C. F. Kennel and F. V. Coroniti, ApJ **283**, 694 (1984).

-
- [105] B. B. Bharat *et al.*, in preparation (private communication) (2014).
- [106] S. Oser *et al.*, *ApJ* **547**, 949 (2001).
- [107] A. Konopelko *et al.*, *Astroparticle Physics* **4**, 199 (1996).
- [108] C. Aragona *et al.*, *ApJ* **698**, 514 (2009).
- [109] V. A. Acciari *et al.*, *ApJ* **679**, 1427 (2008).
- [110] V. A. Acciari *et al.*, *ApJ* **738**, 3 (2011).
- [111] J. Aleksic *et al.*, *ApJ* **746**, 80 (2012).
- [112] E. Aliu *et al.*, *ApJ* **779**, 88 (2013).
- [113] G. E. Romero, D. F. Torres, M. K. Bernado, and I. Mirabel, *A&A* **410**, L1 (2003).
- [114] G. E. Romero, H. R. Christiansen, and M. Orellana, *ApJ*. **632**, 1093 (2005).
- [115] A. M. Atoyan and F. A. Aharonian, *MNRAS* **302**, 253 (1999).
- [116] V. Bosch-Ramon and J. M. Paredes, *A&A* **425**, 1069 (2004).
- [117] V. Bosch-Ramon, G. E. Romero, and J. M. Paredes, *A&A* **447**, 263 (2006).
- [118] B. Bartoli *et al.*, *ApJL* **745**, L22 (2012).
- [119] E. Aliu *et al.*, *ApJ* **788**, 78 (2014).
- [120] L. Saha and P. Bhattacharjee, *ArXiv e-prints* (2014), 1402.4309.
- [121] M. C. Anderson and L. Rudnick, *ApJ* **441**, 307 (1995).
- [122] E. Vinyaikin, *Astronomy Reports* **51**, 570 (2007).
- [123] J. F. Helmboldt and N. E. Kassim, *The Astronomical Journal* **138**, 838 (2009).
- [124] T. DeLaney *et al.*, *ApJ* **725**, 2038 (2010).

-
- [125] E. Helder and J. Vink, *ApJ* **686**, 1094 (2008).
- [126] Y. Maeda *et al.*, ArXiv e-prints (2009), 0912.5020.
- [127] F. Aharonian, *A&A* **370**, 112 (2001).
- [128] J. A. Esposito, S. D. Hunter, G. Kanbach, and P. Sreekumar, *ApJ* **461**, 820 (1996).
- [129] J. Vink and J. M. Laming, *ApJ* **584**, 758 (2003).
- [130] G. G. Pavlov, V. E. Zavlin, B. Aschenbach, J. Trümper, and D. Sanwal, *ApJL* **531**, L53 (2000).
- [131] G. G. Pavlov, D. Sanwal, and M. A. Teter, Central Compact Objects in Supernova Remnants, in *Young Neutron Stars and Their Environments*, edited by F. Camilo and B. M. Gaensler, IAU Symposium Vol. 218, p. 239, 2004.
- [132] A. Bamba, R. Yamazaki, T. Yoshida, T. Terasawa, and K. Koyama, *ApJ* **621**, 793 (2005).
- [133] D. J. Patnaude and R. A. Fesen, *ApJ* **697**, 535 (2009).
- [134] Y. Uchiyama and F. Aharonian, *ApJ* **677**, L105 (2008).
- [135] A. M. Atoyan, R. J. Tuffs, F. A. Aharonian, and H. J. Völk, *A&A* **354**, 915 (2000).
- [136] M. Araya, D. Lomiashvili, C. Chang, M. Lyutikov, and W. Cui, *ApJ* **714**, 396 (2010).
- [137] Y. Yuan *et al.*, *ApJ* **779**, 117 (2013).
- [138] J. Rho, T. Jarrett, W. Reach, H. Gomez, and M. Andersen, *ApJ* **693**, L39 (2009).
- [139] L. O. Drury, *MNRAS* **251**, 340 (1991).
- [140] G. M. Webb, L. O. Drury, and P. Biermann, *A&A* **137**, 185 (1984).
- [141] R. Cowsik and S. Sarkar, *MNRAS* **191**, 855 (1980).

-
- [142] J. M. Laming and U. Hwang, *ApJ* **597**, 347 (2003).
- [143] R. Willingale, J. Bleeker, K. van der Heyden, and J. Kaastra, *A&A* **398**, 1021 (2003).
- [144] E. Parizot, A. Marcowith, J. Ballet, and Y. A. Gallant, *A&A* **453**, 387 (2006).
- [145] A. R. Bell and S. G. Lucek, *MNRAS* **321**, 433 (2001).
- [146] A. R. Bell, *MNRAS* **353**, 550 (2004).
- [147] J. Giacalone and J. R. Jokipii, *ApJL* **663**, L41 (2007).
- [148] R. Landi *et al.*, *The Astronomer's Telegram* **1097**, 1 (2007).
- [149] B. M. Gaensler and P. O. Slane, *ARA&A* **44**, 17 (2006).
- [150] J. J. Hester, *ARA&A* **46**, 127 (2008).
- [151] O. Kargaltsev, G. G. Pavlov, and M. Durant, Pulsar Wind Nebulae from X-rays to VHE γ -rays, in *Electromagnetic Radiation from Pulsars and Magnetars*, edited by W. Lewandowski, O. Maron, and J. Kijak, ASP Conf. Ser. Vol. 466, p. 167, San Francisco, CA, 2012, ASP.
- [152] A. M. Atoyan and F. A. Aharonian, *MNRAS* **278**, 525 (1996).
- [153] W. Bednarek and R. J. Protheroe, *PRL* **79**, 2616 (1997).
- [154] E. Amato, D. Guetta, and P. Blasi, *A&A* **402**, 827 (2003).
- [155] W. Bednarek and M. Bartosik, *A&A* **405**, 689 (2003).
- [156] A. M. Atoyan, *A&A* **346**, L49 (1999).
- [157] A. M. Hillas *et al.*, *ApJ* **503**, 744 (1998).
- [158] A. Van Etten, R. W. Romani, and C.-Y. Ng, *ApJ* **680**, 1417 (2008).

[159] J. S. Mathis, P. G. Mezger, and N. Panagia, *A&A* **128**, 212 (1983).

[160] <http://www.cta-observatory.org>